Stochastic Modelling of Solar Cycle

BY

CELINE DIDIER DUPONT

STUDENT ID: S083514

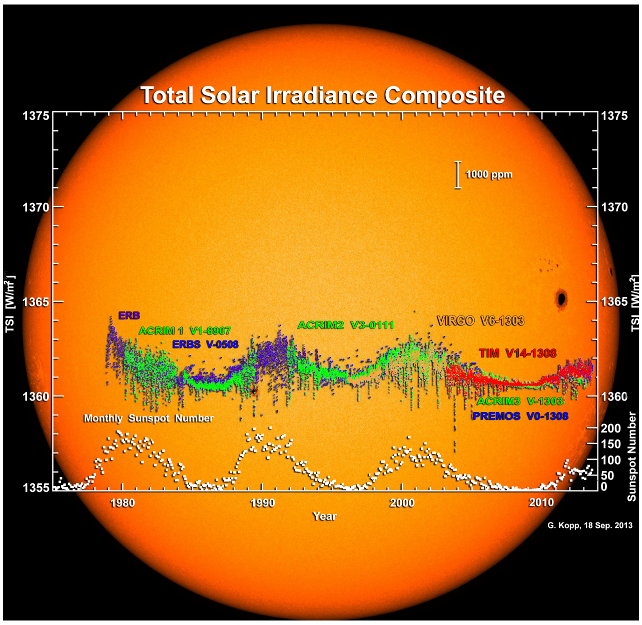

Source:NASA

Main supervisor

HENRIK MADSEN,

Co-supervisors

UFFE HØGSBRO THYGESEN

JAN KLOPPENBORG MØLLER

In cooperation with

ESO (Münich) - Gaitee Hussain

TECHNICAL UNIVERSITY OF DENMARK
SEPTEMBER 1, 2014

Abstract

The solar magnetic field has been analysed through many different aspects, for example by investigating the driving factors that generate the magnetic field, i.e the solar dynamo, or throughout observations of its evolution on the solar surface by analysing sunspots structures and physical features. In the present work, we focus on the large scale evolution of the magnetic field at the solar surface. Firstly, we investigate the flux transport process generated by the supergranular diffusion, the differential rotation and the meridional flow. Based on a recently reviewed flux transport numerical code, a new transport code is developed and implemented in the software R. This new numerical method is a combination of a finite volume and spectral method. The emergence of new magnetic fluxes, pairs of sunspots as Bipolar Magnetic Regions, will be simulated with help of statistical tools, as a Poisson point process in time, making it a stochastic process. On this basis, a full solar cycle is simulated which data are converted into a light curve. With help of real high precision data from the ESA/NASA SOHO spacecraft, VIRGO (Variability of solar IRradiance and Gravity Oscillations), we compare the main features of the spectrum of the simulated light curve to the ones of the empirical data on a short term timescale, i.e six months, and investigate the influence of some of the parameters on a lightcurve. The light curve resulting from the simulation model of the emergence and evolution of the BMR reproduces the main features of the real data. It is even possible by adjusting some of the parameters to reproduce unusual periods in the simulated light curve, corresponding to periods found in the VIRGO data.

Acknowledgements

I wish to express my deep gratitude to Prof. Henrik Madsen who encouraged me to write a project within the field of astrostatistics. Prof. Henrik Madsen helped me, to come in contact with Dr. Gaitee Hussain at ESO and made it possible to meet her in person, at several occasions. Prof. Henrik Madsen's enthusiasm about the project and his expertise, have helped me believe in this project, even at the most critical times.

I would like to acknowledge the help provided by Senior scientist Uffe Høgsbro Thygesen. His incredible ability to make complicated stuff to seem simple, his large amount of patience, availability and last but not least, his experience in working with interdisciplinary subjects and his vast knowledge, have been essential for the realisation of this master thesis.

I am particularly grateful for the assistance given by Dr. Gaitee Hussain, who provided crucial informations about the astrophysics part and supported my work during the whole process. I adress her my deep gratitude for having arranged a five weeks long visit at the ESO research center in Münich.

I wish to thank various researcher, from the dynamical system department at DTU, from the ESO research center in Münich and from the Max Planck institute for Solar System research, for their interest in this project.

Finally, I would like to adress a special thank to Senior scientist Bo Friis Nielsen, who many years ago, convinced med to work with stochastic processes.

My partner Casper, my children, my family and my friends, deserve a special thank for all the help and support they have shown me during this long writing period, full of unforesen circumstances, that just confirms the stochastic aspect of life.

Contents

Introduction

The Sun and solar activity

Solar activity is a global term that covers many different processes on the Sun. Among these processes, and common to them, is that they all reflect changes in the Sun's magnetic field (Hudson, 2008).

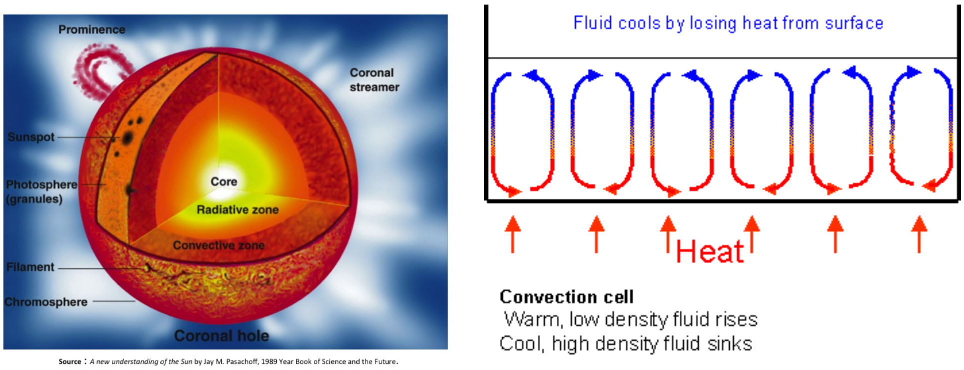

Source : *A new understanding of the Sun* by Jay M. Pasachoff, 1989 Year Book of Science and the Future.

(a) The interior of the Sun

(b) Convection

Figure 1: Structure and transport processes at the interior of the Sun
Figure from: http://starchild.gsfc.nasa.gov

Perturbations in the solar magnetic field are caused by the convection zone in the Sun. This zone is just below the surface, the photosphere (see figure 1(a)). Convection is the process by which heated fluid rises to the surface due to the low density. With ascension, the gas expands in order to conserve mass, before cooling down and sink because of a density that has now become higher than the surrounding material. When the process is repeated, the fluid becomes a part of a convection cell (figure 1(b)).

A convection cell can take any sizes. When the cell is very large, the order of 1000km, it is called granulae or super granulae when the size reaches 30 000km (Jones, 1993). The granulation pattern can be seen on the whole surface of the Sun, except at the sunspots areas (see figure 2). The magnetic field is around one Gauss on average, at the surface of the Sun, at the upper part of the photosphere. In some areas, the magnetic field becomes very strong, up to 3700 Gauss (Solanki, 2003), leading to the inhibition of the convection of heat from the interior of the Sun. A consequence of these depressions is a quite important loss of temperature at these regions, where it falls to approximatively 4300 K; that is 20% cooler than the surrounding temperature of 5500 K. That is the reason why these cooler regions seem darker, which explains why they are called "dark spots" or "sunspots" (Jones, 1993).

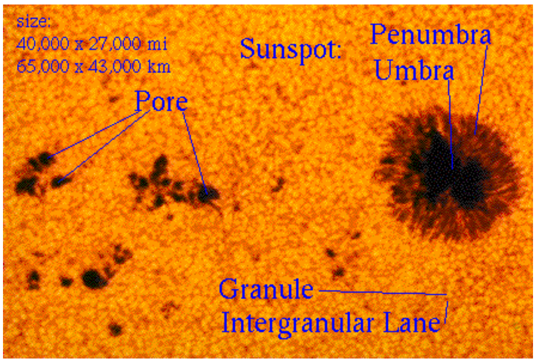

Figure 2: Structure of the photosphere - Figure from: http://starchild.gsfc.nasa.gov

Surface transport processes

The main surface transport processes at solar surface are the supergranular diffusion, the differential rotation and the meridional flow.

The supergranular diffusion

The supergranular diffusion is an effect of the small-scale convective motions of supergranules on the large scale magnetic field of the Sun (Mackay and Yeates, 2012). It makes the magnetic field to dissipate and contributes to the poleward motion of the magnetic field. The diffusion acts on a long time scale in the order of 30 - 50 years.

The differential rotation

The differential rotation of the Sun is a characteristic for non solid rotating bodies(See figure 3). It acts in a East - West direction and makes the equator rotate faster than at the poles (Mackay and Yeates, 2012). It takes 25 days to perform one rotation at the equator while it can take up to 36 days at the poles. Another effect of the differential rotation, is after some time, i.e in the order of one year, the separation of the magnetic field into bands of opposite polarity as the field moves polewards (Mackay and Yeates, 2012).

The meridional flow

It is a weak flow that transports material from the equator towards the poles at the solar surface and back again from the poles to the equator at the interior of the Sun (Schmieder and Pariat, 2007) (see figure 3). It appears that it takes the meridional flow 11 years to transport material at the solar interior, from mid latitude towards the equator; a transport time that corresponds to a sunspot cycle and a feature that explains the pattern seen on the butterfly diagram (figure 4).

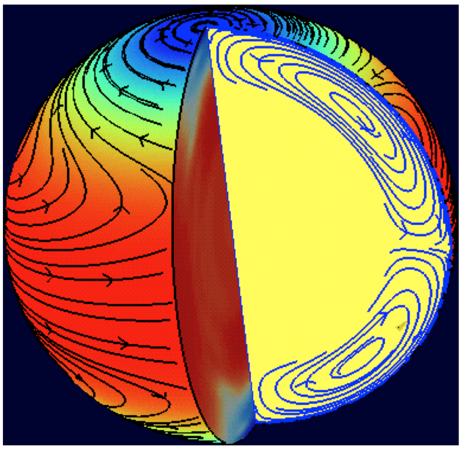

Figure 3: Meridional flow and differential rotation - Figure from (Hathaway, 2012)

Sunspots and faculae

A group of sunspots forms in particularly magnetic active areas, called active regions. Faculae, or bright spots, are associated to sunspots. They cover the whole surface of the Sun, however, they are only visible near the spots. Sunspot sizes varie from 300km to 100 000km and the lifetime of one spot spans from hours to months. Observations show that, they come as a pair of opposite polarity, one positive, one negative. The number of these magnetic bipoles follows a cycle, called the solar or sunspot cycle. One cycle is usually defined as the time it takes to go from one solar minimum where there are very few sunspots to another solar miminum. In the middle of a cycle, called the solar maximum, it can be counted up to two hundred of sunspots when the maximum is very high. Each cycle spans between 8 years and 14 years, giving an average of 11 years. The solar magnetic field reverses at each sunspot cycle, meaning that the solar magnetic cycle is of 22 years (Hale et al., 1919). The butterfly diagram (see figure 4) shows that the emergence of the spots is at highest latitude, around 40 degrees, at the beginning of a cycle, and ends very near the equator, around 5 degrees, at the end of the cycle. The latitude of sunspot emergence during a sunspot cycle is decreasing from high latitudes to equatorial-close latitudes. This figure shows as well, that the spots form as pairs symmetrically around the equator, creating patterns that looks like butterflies. Many informations about the behaviour of the solar dynamo can be established by observing the sunspots and their cycles.

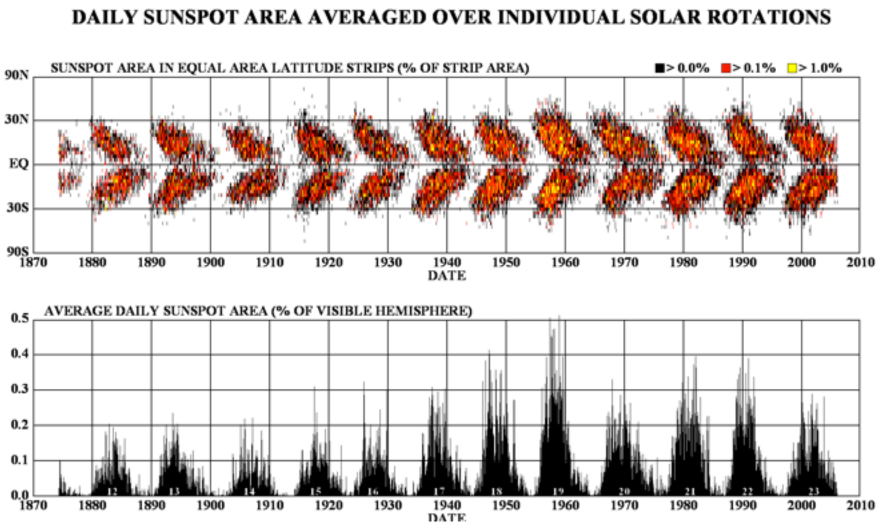

Figure 4: Butterfly diagram Figure from: http://nasa.gov

Lightcurves

The light emitted from the Sun, changes during a solar cycle. The solar luminosity, which is the total energy radiated each second in all directions at the surface of the Sun, is higher at sunspots maxima, despite of the darker effect of the spots (Jones, 1993). Some other phenomena at the solar surface, such as sun flares, which are sudden and intense eruptions of magnetic energy, or the faculae, follow the sunspot cycle, and the change in luminosity permits to retrace the solar cycle. Registration of lightcurves from the Sun or other stars is therefore a way to gather information about the behaviour of the magnetic field on these stellar targets.

Motivation

Astrostatistics is a field under development alongside new intrumentation and techniques have allowed to gather much larger and precise set of data than before. In particular, Space missions like the NASA Kepler mission have succeeded in gathering high precision lightcurves of tens of thousands of spotted magnetically active stars. There is clearly an opportunity for applying newer statistical tools for analysing light curves and the underlying processes that governs the evolution of the magnetic field on the Sun and other solar-type stars. A model for understanding the magnetic flux transport on the surface of the Sun has been developed by van Ballegooijen et al. (1998) and has since been optimized by Mackay et al. (2004), Baumann (2005) and lately by Cameron et al. (2010). This is a numerical simulation that gives informations about how the magnetic field expands at solar surfaces. This model is of special interest for a deeper knowledge of the emergence of magnetic flux and its evolution under differential rotation, supergranular diffusion and meridional flow. A better understanding of these phenomena on the Sun would be a basis for carrying out analysis of the magnetic field on other stars, as dark spots and similar magnetic processes to the Sun have been observed on other stellar objects. It would be of greatest interest to investigate statistically the behaviour of stellar magnetic flux transport as stars of the same spectral type are subject to the same flux transport processes. Differences in their ages, temperatures, i.e convection zone sizes, are believed to drive differences in the timescales of these processes. By studying the Sun as a star in the way that we do in the present work, we can learn how sensitively flux transport processes can be measured from high precision lightcurves.

Goal

The overriding purpose of this project is to investigate the effect of different solar parameters on the spectra of light curves. To this end, we need to model the new emergence of magnetic flux, here as a stochastic process, before making it undergo the effect of the different flow processes, and afterwards convert the magnetic flux into a light curve. Thenafter it is possible to perform a parameter study of the processes that influence the evolution of the magnetic flow at the solar surface both from a simulated light curve and from a light curve from real data. For the parameter estimations, a dynamical system model would possibly provide informations about the underlying processes that makes the magnetic field to evolve.

Project outline

The project is divided into three different parts.

Part 1

The first part deals with the numerical approximation to the solution of a homogeneous flux transport PDE. We will start by presenting the flux transport model represented by a partial differential equation on the sphere. In the next chapters we will briefly outline the most common way to solve a Partial Differential Equation numerically, i.e. the finite methods and the spectral method. In chapter four, we will focus on a decomposition of the field into real spherical harmonics and try to implement the solution of the PDE with this method, which has been the most common way to handle this specific equation. A new numerical approach combining the conservative properties of a finite volume and the accuracy of a spectral method, will be proposed. In the last chapter of this first part, the model will be tested through some initial conditions specifically chosen in order to test each process that constitutes the magnetic flux transport code at the solar surface.

Part 2

In the second part, we will start by investigating how to simulate the emergence of new magnetic sources, sunspots in form of Bipolar Magnetic Regions (BMR), as a stochastic process. The properties of the BMR are introduced and a detailed explanation for how to simulate pairs of sunspots as a BMR is presented. Thenafter, the emergence of these BMR as a Poisson point process is outlined. Once the process has been defined, it can be added to the homogeneous flux transport PDE from Part I. The process is verified through a simulation of two solar cycles, where the simulation runs for 12 years with a half year of overlap in both ends of the cycle, resulting in a cycle of 11 years. As it will be seen in part III, in real life, each solar cycle has different durations with different rates of BMR emergences. We will not take these variations into account in this work.

In the following chapter, we will convert the simulated evolution of the magnetic field into a light curve. To this end, it is necessary to take accounts for measurement corrections for the light emitted from the sunspots and the faculae. Once these corrections have been calculated, a light curve can be produced by taking a weighted sum of the integration of the intensity of the spots and the faculae, over the sphere.

Part 3

In a third part, an investigation of the spectrum of real data from VIRGO will be carried out and compared to the one from the simulated light curve. The work will be done on a six months time scale. Two methods will be tested. It is most common to consider the dynamical system that represents a light curve, as a linear system and perform simple statistical analysis e.g linear regression and discrete time ARMA models but recent research has shown that there is a need to consider non linear modelling instead. The latter will not be tested in the present project.

First, we will consider the VIRGO light curve as a linear continuous time stochastic ARMA process, estimate its parameters from which the spectrum can be found with help of the system's transfer function. We will see that the linear modelling shows some limitations and will work with a Lomb Scargle periodogram, a widely used method when dealing with unevenly spaced time series such as astrophysical data. The last analysis will be about the parameters that govern the flux transport code. We will try to change different parameter values, e.g increase the rate of emergence of the BMR or tune the velocity of the advection and the diffusion time scale in order to change the spectrum of the simulated light curve and find periods corresponding to the periods from the spectrum of the real data.

Notes

- Throughout this project, unless something else is stated, the figures that represent the Sun will be shown as a rectangular projection of the solar surface on a ϕ, θ grid, where ϕ is the longitude that runs from 0 to 2π, on the x-axis and θ the colatitude, that runs from 0 to π, 0 at north, on the y-axis. It will happen for symmetry reasons, that the y-axis will not represent the colatitude, but the latitude $\frac{\pi}{2} - \theta$.

- Unless something else is stated, the color scale on the figures is not the same for all figures, but belongs to the shown figure only.

- The magnetic field on the figures is measured in Gauss.

- The time unit for velocities will be in $\frac{km}{s}$

- One day is 24 hours, one month is 30 days, one year is 365 days.

Part I

Numerical methods

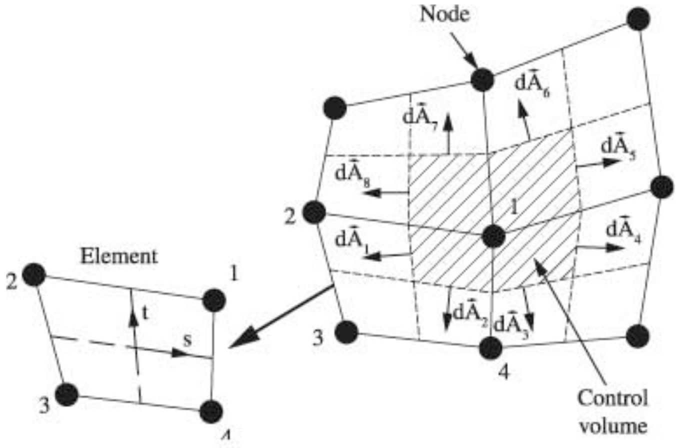

Source:http://dx.doi.org/10.1590/S1516-14392011005000049

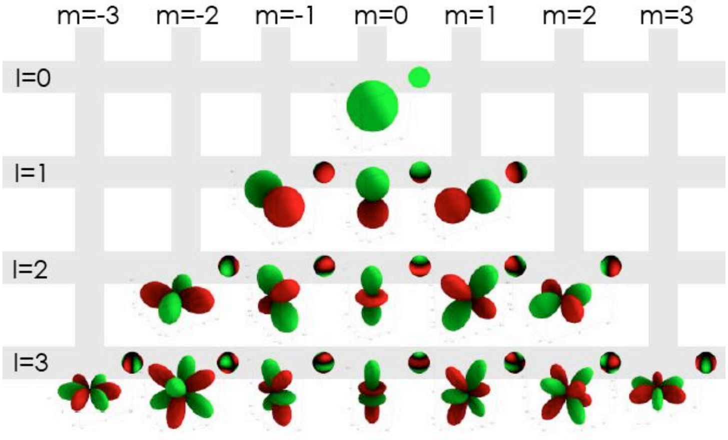

Source: http://nccasymposium.bmth.ac.uk/2007/joao_montenegro/theory.html

Table of Contents

Chapter 1

Introduction

The magnetic field on the solar surface is subjected to a magnetic transport flux. The present work focuses on the transport of the large - scale magnetic field originating from new magnetic sources. In this part, we will develop a numerical code that can reproduce the main features of the dispersal of the flux under the effect of the meridional flow, that pushes the flux polewards, the differential rotation, that makes the flow travel fastest at the equator and the supergranular diffusion, that dissipates the magnetic field.

1.1 The model equation

Mackay et al. (2004), Baumann (2005) , (Cameron et al., 2010), among other, have worked on the flux transport model that was first described by van Ballegooijen et al. (1998). The evolution of the magnetic flux B_r is a Partial Differential Equation, PDE, and can be written as defined by Mackay and Yeates (2012):

$$\begin{aligned}\frac{\partial B_r}{\partial t} &= -\omega(\theta)\frac{\partial B_r}{\partial \phi} - \frac{1}{\sin(\theta)}\frac{\partial}{\partial \theta}\left[v(\theta)B_r\sin(\theta)\right] \\ &+ D[\frac{1}{\sin(\theta)}\frac{\partial}{\partial \theta}(\sin(\theta)\frac{\partial B_r}{\partial \theta}) \\ &+ \frac{1}{\sin^2(\theta)}\frac{\partial^2 B_r}{\partial \phi^2}] \\ &+ S(\theta, \phi, t) \qquad (1.1)\end{aligned}$$

This equation represents the evolution of the magnetic field at the surface of a stellar object, considered as a sphere. The magnetic flux $B_r(\theta, \phi, t)$ is

a function of the colatitude θ, that goes from 0, at the North pole, to π in the South pole, of ϕ, the longitude that goes from 0 to 2π in the East - West direction and of the time t. D is the supergranular diffusion that dissipates the flux on the sphere (Mackay and Yeates, 2012), $\omega(\theta)$ is the differential rotation that operates in East - West and $v(\theta)$ is the meridional flow that acts in the North - South direction, and $S(\theta, \phi, t)$ is a source term of new emerging flux (Baumann, 2005).
We will start by looking at equation 1.1 without any source term , $S(\theta, \phi, t) = 0$.

On a general level, there are mainly two different ways of solving numerically a PDE, the spectral method and the finite methods. The finite methods comprise the Finite Element Method (FEM), the Finite Difference Method (FDM) and the Finite Volume Method (FVM). We will start by briefly outline the spectral method and investigate an approximation to the solution of the PDE presented in equation 1.1 with spherical harmonics. In the following chapter, the finite methods will be introduced and we will look at the solution found with a combined finite volume and spectral method.

Chapter 2

The Spectral Method

The spectral method approximates the solution of the PDE by some linear combination of orthogonale basis functions.

In 1D, if we want to approximate a periodic function f with period 2π, the orthogonal basis can be composed of Fourier basis functions, that forms a basis of cosine and sine functions $\{(\cos(lx), \sin(lx)) : l \in R\}$, in the complex form :

$$f(x) = \sum_{l=-\infty}^{\infty} c_l \exp(ilx) \tag{2.1}$$

where c_l are the coefficients of the function f with respect to the basis $\exp(ilx)$. They can be found by multiplying each side by the complex conjugate of the basis functions and taking the integral over the period interval:

$$c_l = \frac{1}{2\pi} \int_{-\pi}^{\pi} f(x) e^{-ilx} dx \tag{2.2}$$

The complex exponential are the orthogonale expansion basis functions. Their inner product is defined by :

$$\begin{aligned} < \exp(ilx), \exp(ikx) > &= \frac{1}{2\pi} \int_{-\pi}^{\pi} \exp(ilx) \exp(ikx) \quad dx \\ &= \delta_{lk} \end{aligned} \tag{2.3}$$

where δ is the Kronecker delta,

$$\delta_{lk} = \begin{cases} 1 & \text{if } l = k \\ 0 & \text{if } l \neq k \end{cases} \tag{2.4}$$

2.1 Spherical harmonics

The analog of the Fourier in 1D on a sphere are the spherical harmonics. The spherical coordinates becomes $\{(r, \theta, \phi) : r \in R_+, \theta \in [0, \pi], \phi \in [0, 2\pi]\}$ where r is the radius, that we will considere as being equal to one in this work, θ the colongitude, and ϕ the latitude.
Spherical harmonics are harmonic functions that are solution to the Laplace equation, when restricted to the sphere. They form a basis for the L^2 functions on a sphere. The Laplace operator $\triangle$, for the unit sphere, is given by the angular Laplacian:

$$\triangle = \frac{1}{\sin\theta}\frac{\partial}{\partial\theta}(\sin\theta\frac{\partial}{\partial\theta}) + \frac{1}{\sin^2\theta}\frac{\partial^2}{\partial\phi^2} \tag{2.5}$$

The solution of the Laplace equation for a field B on a unit sphere becomes:

$$\triangle B = \frac{1}{\sin\theta}\frac{\partial}{\partial\theta}(\sin\theta\frac{\partial B}{\partial\theta}) + \frac{1}{\sin^2\theta}\frac{\partial^2 B}{\partial\phi^2} = 0 \tag{2.6}$$

It can be shown that the general complex solutions of the part in θ is given by the associated Legendre polynomials :

$$P_l^m(x) = (-1)^m(1-x^2)^{\frac{m}{2}}\frac{d^m}{dx^m}(P_l(x)) \tag{2.7}$$

where l is the degree and m is the order, $P_l(x)$ is the Legendre polynomials:

$$P_l(x) = \frac{1}{2^n n!}\frac{d^n}{dx^n}(x^2-1)^n \tag{2.8}$$

and the solution of the part in ϕ is of the form $Ce^{im\phi}$.

The normalised complex spherical harmonics are defined as:

$$Y_l^m(\theta, \phi) = N_l^m P_l^m(\cos(\theta))e^{im\phi} \tag{2.9}$$

where N_l^m are the normalisation constants.

Thus, the spherical harmonics $Y_l^m(\theta, \phi)$ are solution to the differential equation:

$$\triangle Y_l^m(\theta,\phi) = -l(l+1)Y_l^m(\theta,\phi) \tag{2.10}$$

One of their characteristics is that they are eigenfunctions to the spherical Laplacian operator with corresponding eigenvalues $l(l+1)$. They are basis functions and the spherical harmonics are orthonormal to each other.

$$\int_S Y_l^m(\theta,\phi)\tilde{Y}_k^n(\theta,\phi)dS = \delta_{lk}\delta mn \tag{2.11}$$

where $\int_S$ is the integral over the sphere,$\int_S = \int_\phi \int_\theta$ with the surface element $dS = \sin(\theta)d\theta d\phi$ and $\tilde{Y}_l^n(\theta,\phi)$ the complex conjugate.

We can now write equation 2.6 as an expansion of functions of ϕ and of θ:

$$B(\theta,\phi,t) = \sum_{l=0}^{\infty}\sum_{m=-l}^{m=l} c_l^m(t)Y_l^m(\theta,\phi) \tag{2.12}$$

where the $c_l^m(t)$ are complex coefficients at time t, of the form $a_l^m + ib_l^m$. They can be found as in equation 2.2 :

$$c_l^m(t) \;\; = \;\; \int_S B(\theta,\phi,t)\tilde{Y}_l^m(\theta,\phi)dS \tag{2.13}$$

2.2 Real spherical harmonics

It is also possible to work with real spherical harmonics.

$$Y_l^m(\theta,\phi) = \begin{cases} Y_l^{m^+}(\theta,\phi) &= \sqrt{2}Re(Y_l^m(\theta,\phi)) = \sqrt{2}N_l^m\cos(m\phi)P_l^m(\cos\theta), m>0 \\ Y_l^0(\theta,\phi)) &= N_l^0P_l^0(\cos\theta), m=0 \\ Y_l^{m^-}(\theta,\phi) &= \sqrt{2}Im(Y_l^m(\theta,\phi)) = \sqrt{2}N_l^{|m|}\sin(|m|\phi)P_l^{|m|}(\cos\theta), m<0 \end{cases} \tag{2.14}$$

The real spherical harmonics are orthonormal as well, for each case of m value and the relation from 2.11 holds:

$$\begin{aligned}
\int_S Y_l^{m^+}(\theta,\phi)\tilde{Y}_k^{n^+}(\theta,\phi)dS &= \delta_{lk}\delta mn \\
\int_S Y_l^{m^-}(\theta,\phi)\tilde{Y}_k^{n^-}(\theta,\phi)dS &= \delta_{lk}\delta mn \\
\int_S Y_l^{0}(\theta,\phi)\tilde{Y}_k^{0}(\theta,\phi)dS &= \delta_{lk} \qquad (2.15)
\end{aligned}$$

The following plots show the real spherical harmonics of order 10 and degree 21, Y_{10}^{21}:

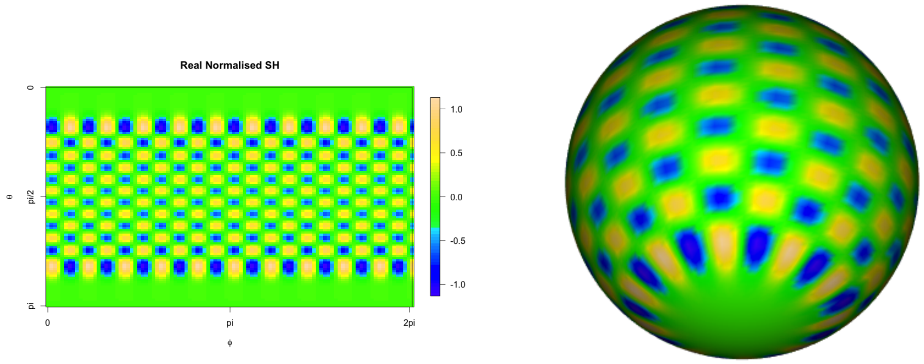

(a) 2D plot of Y_{10}^{21} (b) 3D plot of Y_{10}^{21}

Figure 2.1: Real normalised spherical harmonics

[

Chapter 3

Decomposition of the magnetic field into spherical harmonics

We now want to solve equation 1.1 with help of spherical harmonics. All this chapter is based on the method used by Baumann (2005). However, in the present work, we have performed all the implementations R, and have encountered limitations when working with complex spherical harmonics. We will therefore solve the PDE with real spherical harmonics, despite of the supplementary numbers of calculations, although Baumann (2005) used the complex form.

We write equation 1.1 in a diffusion - advection form:

$$\begin{aligned} \frac{\partial B_r}{\partial t} &= \underbrace{D\left(\frac{1}{\sin(\theta)}\frac{\partial}{\partial\theta}(\sin(\theta)\frac{\partial B_r}{\partial\theta}) + \frac{1}{\sin^2(\theta)}\frac{\partial^2 B_r}{\partial\phi^2}\right)}_{\text{diffusion}} \\ &- \underbrace{\left[\frac{1}{\sin(\theta)}\frac{\partial}{\partial\theta}(\sin\theta v(\theta)B_r) + \omega(\theta)\frac{\partial B_r}{\partial\phi}\right]}_{\text{advection}} \end{aligned} \quad (3.1)$$

We recognize the diffusion part as the Laplace equation on a sphere with a unit radius, as described in equation 2.5.

3.1 Solving the expansion coefficients ODE

We follow the procedure described in section 2.1 more specifically, the magnetic field at the surface $B_r(\theta, \phi, t)$ can be decomposed into real spherical harmonics.

$$\begin{aligned}
B_r(\theta,\phi,t) &= \sum_{l=0}^{\infty}\sum_{m=-l}^{m=l} c_l^m(t)Y_l^m(\theta,\phi) \\
&= \sum_{l=0}^{\infty}\sum_{m=-l}^{m=l} [(a_l^m(t)+ib_l^m(t))(N_l^mP_l^m(\cos(\theta))(\cos(m\phi)+i\sin(m\phi)))] \\
&= \sum_{l=0}^{\infty}\sum_{m=-l}^{m=l} [(a_l^m(t)\cos(m\phi)-b_l^m(t)\sin(m\phi)) \\
&+ i(a_l^m(t)\sin(m\phi)+b_l^m(t)\cos(m\phi))](N_l^mP_l^m(\cos(\theta))] \qquad (3.2)
\end{aligned}$$

It is clear that if $a_l^m(t) = a_l^{-m}(t)$ and $b_l^{-m}(t) = -b_l^m(t)$ the imaginary part cancels out term by term. Setting $b_l^0(t) = 0$, and using relation 2.14, we can see that equation 3.2 reduces to:

$$\begin{aligned}
B_r(\theta,\phi,t) &= \sum_{l=0}^{\infty} a_l^0(t)Y_l^0 \\
&+ \sum_{l=1}^{\infty}\sum_{m=1}^{m=l} a_l^m(t)Y_l^{m^+} \\
&+ \sum_{l=1}^{\infty}\sum_{m=1}^{m=l} b_l^m(t)Y_l^{m^-} \qquad (3.3)
\end{aligned}$$

We start by inserting equation 3.2 in equation 3.1, first for the diffusion part and afterwards for the advection:

$$\begin{aligned}
&D\left[\frac{1}{\sin(\theta)}\frac{\partial}{\partial\theta}(\sin(\theta)\frac{\partial B_r}{\partial\theta}) + \frac{1}{\sin^2(\theta)}\frac{\partial^2 B_r}{\partial\phi^2}\right] \\
&= \sum_{l=0}^{\infty}\frac{D}{\sin(\theta)}\frac{\partial}{\partial\theta}\left(\sin(\theta)\frac{\partial}{\partial\theta}(a_l^0(t)Y_l^0(\theta,\phi))\right) + \frac{D}{\sin^2(\theta)}\frac{\partial^2}{\partial\phi^2}(a_l^0(t)Y_l^0(\theta,\phi)) \\
&+ \sum_{l=1}^{\infty}\sum_{m=1}^{m=l}\frac{D}{\sin(\theta)}\frac{\partial}{\partial\theta}\left(\sin(\theta)\frac{\partial}{\partial\theta}(a_l^m(t)Y_l^m(\theta,\phi)+b_l^m(t)Y_l^m(\theta,\phi)\right) \\
&+ \frac{D}{\sin^2(\theta)}\frac{\partial^2}{\partial\phi^2}(a_l^m(t)Y_l^m(\theta,\phi)+b_l^m(t)Y_l^m(\theta,\phi)) \\
&= \underbrace{-Dl(l+1)a_l^0(t)Y_l^0(\theta,\phi)}_{\text{diffusion m = 0}} \\
&+ \underbrace{-Dl(l+1)a_l^m(t)Y_l^{m^+}(\theta,\phi)}_{\text{diffusion m positive}} \\
&+ \underbrace{-Dl(l+1)b_l^m(t)Y_l^{m^-}(\theta,\phi)}_{\text{diffusion m negative}} \qquad (3.4)
\end{aligned}$$

Now we look at the advection part , that we can split up into two processes, first the meridional (*NOTE that the Legendre polynomials are functions of* $\cos(\theta)$ *but will here be written as* P_l^m *for shorter notation*).

$$
\begin{aligned}
&-\frac{1}{\sin\theta}\frac{\partial}{\partial\theta}(\sin(\theta)v(\theta)B_r) \qquad\qquad (3.5)\\
&= \sum_{l=0}^{\infty}-\frac{1}{\sin(\theta)}\frac{\partial}{\partial(\theta)}\Big(\sin(\theta)v(\theta)a_l^0(t)Y_l^0(\theta,\phi)\Big)\\
&+ \sum_{l=1}^{\infty}\sum_{m=1}^{m=l}-\frac{1}{\sin(\theta)}\frac{\partial}{\partial(\theta)}\Big(\sin(\theta)v(\theta)(a_l^m(t)Y_l^{m^+}(\theta,\phi)+b_l^m(t)Y_l^{m^-}(\theta,\phi))\Big)\\
&= \sum_{l=0}^{\infty}\underbrace{-\frac{1}{\sin(\theta)}\left(\cos(\theta)v(\theta)P_l^0+\sin(\theta)\frac{dv(\theta)}{d\theta}P_l^0+\sin(\theta)v(\theta)P_l^1)a_l^0N_l^0\right)}_{\text{meridional advection m = 0}}\\
&- \sum_{l=1}^{\infty}\sum_{m=1}^{m=l}\underbrace{\frac{1}{\sin(\theta)}\left((l+1)\cos(\theta)v(\theta)P_l^m+\sin(\theta)\frac{dv(\theta)}{d\theta}P_l^m-(l+m)\sin(\theta)v(\theta)P_{l-1}^m)a_l^mN_l^m\right)}_{\text{meridional advection m positive}}\\
&- \underbrace{\frac{1}{\sin(\theta)}\left((l+1)\cos(\theta)v(\theta)P_l^m+\sin(\theta)\frac{dv(\theta)}{d\theta}P_l^m-(l+m)\sin(\theta)v(\theta)P_{l-1}^m a_l^mN_l^m\right)}_{\text{meridional advection m negative}}
\end{aligned}
$$

then the zonal flow:

$$
\begin{aligned}
&-\omega(\theta)\frac{\partial B_r}{\partial\phi}\\
&= \sum_{l=0}^{\infty}-\omega(\theta)\frac{\partial}{\partial\phi}\Big(a_l^0(t)Y_l^0(\theta,\phi)\Big)+\sum_{l=1}^{\infty}\sum_{m=1}^{m=l}\omega(\theta)\frac{\partial}{\partial\phi}\left(a_l^m(t)Y_l^m(\theta,\phi)+b_l^m(t)Y_l^m(\theta,\phi)\right)\\
&= \sum_{l=1}^{\infty}\sum_{m=1}^{m=l}\underbrace{m\omega(\theta)a_l^m(t)N_l^mP_l^m\sin(m\phi)}_{\text{differential rotation m positive}}-\underbrace{m\omega(\theta)b_l^m(t)N_l^mP_l^m\cos(m\phi)}_{\text{differential rotation m negative}} \qquad (3.6)
\end{aligned}
$$

The coefficients can be found using the orthonormality of the spherical harmonics, i.e. relation 2.11 :

Coefficients when m = 0

$$
\begin{aligned}
\dot{a}_l(t) &= -Dl(l+1)a_l(t)-2\pi\sum_{k=0}^{\infty}N_kN_l\int_0^{\pi}a_k(t)P_l\Big[\frac{\partial v(\theta)}{\partial\theta}\sin(\theta)P_k\\
&+ v(\theta)\cos(\theta)P_k+\sin(\theta)v(\theta)P_k^1\Big]d\theta \qquad (3.7)
\end{aligned}
$$

Coefficients when m < 0

$$\begin{aligned}
\dot{b}_l^m(t) &= -Dl(l+1)b_l^m(t) - 2\pi \sum_{k=1}^{\infty} N_k^m N_l^m \int_0^{\pi} P_l^m \Big[a_k^m(t) m\omega(\theta) P_k^m \qquad (3.8)\\
&+ b_k^m(t) \left(\frac{\partial v(\theta)}{\partial \theta} \sin(\theta) P_k^m + (k+1) v(\theta)\cos(\theta) P_k^m - (k+m)\sin(\theta) v(\theta) P_{k-1}^m \right) \Big] d\theta
\end{aligned}$$

Coefficients when m > 0

$$\begin{aligned}
\dot{a}_l^m(t) &= -Dl(l+1)a_l^m(t) - 2\pi \sum_{k=1}^{\infty} N_k^m N_l^m \int_0^{\pi} P_l^m \Big[-b_k^m(t) m\omega(\theta) P_k^m \\
&+ a_k^m(t) \Big(\frac{\partial v(\theta)}{\partial \theta} \sin(\theta) P_k^m + (k+1) v(\theta)\cos(\theta) P_k^m \\
&- (k+m)\sin(\theta) v(\theta) P_{k-1}^m \Big) \Big] d\theta \qquad (3.9)
\end{aligned}$$

It is of course not possible to take the summation until ∞ and the solution has to be truncated at a suitable wavenumber $lmax = N$.

3.2 System of differential equations for the coefficients

The differential equations of the coefficients is now reduced to a differential equation in time, of the form $\dot{a}(t) = Aa(t)$, where A is a system matrix composed of the elements described above, the meridional flow, the differential rotation and the diffusion. The system matrix A only needs to be calculated once. The system of differential equations is such that :

$$\begin{pmatrix} \dot{a}_l^m(t) \\ \dot{a}_{l+1}^m(t) \\ \vdots \\ \dot{a}_{lmax}^m(t) \\ \dot{b}_l^m(t) \\ \dot{b}_{l+1}^m(t) \\ \vdots \\ \dot{b}_{lmax}^m(t) \end{pmatrix} = \begin{pmatrix} A_{l,k}^m & \cdots & A_{l,kmax}^m \\ A_{(l+1),k}^m & \cdots & A_{(l+1),(kmax)}^m \\ \vdots & \ddots & \vdots \\ A_{lmax,k}^m & \cdots & A_{lmax,kmax}^m \\ A_{l,k}^m & \cdots & A_{l,kmax}^m \\ A_{(l+1),k}^m & \cdots & A_{(l+1),(kmax)}^m \\ \vdots & \ddots & \vdots \\ A_{lmax,k}^m & \cdots & A_{lmax,kmax}^m \end{pmatrix} \begin{pmatrix} a_k^m(t) \\ a_{k+1}^m(t) \\ \vdots \\ a_{kmax}^m(t) \\ b_k^m(t) \\ b_{k+1}^m(t) \\ \vdots \\ b_{kmax}^m(t) \end{pmatrix} \qquad (3.10)$$

The "a" coefficients are for $m \geq 0$ and the "b" are for $m < 0$. We can see in

equations 3.9 and equation 3.9 that some of the coefficients for m negative are a part of the differential equation for the coefficients for m positive and vice versa. This is due to the differentiation in ϕ for the differential rotation .
The differential rotation has an effect on the East - West direction and has therefore no effect when m = 0. If the indexes of the coefficients l and k are such that k + l are odd, the elements become 0 and we end with a system of differential equations that look the following way , for lmax = 3:

Case 1 : $m = 0$

In the diagonal, the A matrix is composed of the meridional flow and the diffusion, otherwise, only of the meridional flow.

$$\begin{pmatrix} \dot{a}_0^0(t) \\ \dot{a}_1^0(t) \\ \dot{a}_2^0(t) \\ \dot{a}_3^0(t) \end{pmatrix} = \begin{pmatrix} -A_{00}^0 & 0 & -A_{02}^0 & 0 \\ 0 & -A_{11}^0 & 0 & -A_{13}^0 \\ -A_{20}^0 & 0 & -A_{22}^0 & 0 \\ 0 & -A_{31}^0 & 0 & -A_{33}^0 \end{pmatrix} \begin{pmatrix} a_0^0(t) \\ a_1^0(t) \\ a_2^0(t) \\ a_3^0(t) \end{pmatrix} \tag{3.11}$$

Case 2:m $\neq$ 0

The main diagonal in the whole matrix is still the diffusion and the meridional flow, while the upper right and lower left submatrices are purely composed of the differential rotation, and the two other submatrices, that contains the main diagonal, are composed of the meridional flow.

$$\begin{pmatrix} \dot{a}_1^1(t) \\ \dot{a}_2^1(t) \\ \dot{a}_3^1(t) \\ . \\ \dot{b}_1^1(t) \\ \dot{b}_2^1(t) \\ \dot{b}_3^1(t) \end{pmatrix} = \left(\begin{array}{ccccccc} -A_{11}^1 & 0 & -A_{13}^1 & \vdots & A_{11}^1 & 0 & A_{13}^1 \\ 0 & -A_{22}^1 & 0 & \vdots & 0 & A_{22}^1 & 0 \\ -A_{31}^1 & 0 & -A_{33}^1 & \vdots & A_{13}^1 & 0 & A_{33}^1 \\ \cdots & \cdots & \cdots & \cdots & \cdots & \cdots & \cdots \\ -A_{11}^1 & 0 & -A_{13}^1 & \vdots & -A_{11}^1 & 0 & -A_{13}^1 \\ 0 & -A_{22}^1 & 0 & \vdots & 0 & -A_{22}^1 & 0 \\ -A_{31}^1 & 0 & -A_{33}^1 & \vdots & -A_{31}^1 & 0 & -A_{33}^1 \end{array}\right) \begin{pmatrix} a_1^1(t) \\ a_2^1(t) \\ a_3^1(t) \\ . \\ b_1^1(t) \\ b_2^1(t) \\ b_3^1(t) \end{pmatrix}$$

$$\begin{pmatrix} \dot{a}_2^2(t) \\ \dot{a}_3^2(t) \\ . \\ \dot{b}_2^2(t) \\ \dot{b}_3^2(t) \end{pmatrix} = \begin{pmatrix} -A_{22}^2 & 0 & \vdots & A_{22}^2 & 0 \\ 0 & -A_{33}^2 & \vdots & 0 & A_{33}^2 \\ \cdots & \cdots & \cdots & \cdots & \cdots \\ -A_{22}^2 & 0 & \vdots & -A_{22}^2 & 0 \\ 0 & -A_{33}^2 & \vdots & 0 & -A_{33}^2 \end{pmatrix} \begin{pmatrix} a_2^2(t) \\ a_3^2(t) \\ . \\ b_2^2(t) \\ b_3^2(t) \end{pmatrix}$$

$$\begin{pmatrix} \dot{a}_3^3(t) \\ . \\ \dot{b}_3^3(t) \end{pmatrix} = \begin{pmatrix} -A_{33}^3 & \vdots & A_{33}^3 \\ \cdots & \cdots & \cdots \\ -A_{33}^3 & \vdots & -A_{33}^3 \end{pmatrix} \begin{pmatrix} a_3^3(t) \\ . \\ b_3^3(t) \end{pmatrix} \tag{3.12}$$

Each matrix for a specific m value is a square matrix. Thus, the solution of this system of differential equations is of the form:

$$a_l^m(t) = \exp(At) a_l^m(t = 0) \tag{3.13}$$

where the $a_l^m(t = 0)$ are defined as in equation 2.13 i.e. for real coefficients:

$$\begin{aligned} a_l^0(t = 0) &= \int_S B_r(\theta, \phi, t = 0) Y_l^0(\theta, \phi) dS \\ a_l^{m^+}(t = 0) &= \int_S B_r(\theta, \phi, t = 0) Y_l^{m^+}(\theta, \phi) dS \\ a_l^{m^-}(t = 0) &= \int_S B_r(\theta, \phi, t = 0) Y_l^{m^-}(\theta, \phi) dS \end{aligned} \tag{3.14}$$

We end with a system of $(\mathrm{lmax} + 1)^2$ differential equations to solve. The number of equations to solve can be reduced by using the complex form, and becomes then $\frac{(\mathrm{lmax}+1)(\mathrm{lmax}+2)}{2}$ for each t (Baumann, 2005). All these integral approximations can make the code running slower when using the real form.

The spherical harmonics approach for the approximation to the solution of the flux transport PDE will be tested in chapter 6.

Chapter 4

The Finite methods

We will now briefly stress the finite methods, i.e the Finite Difference Method, FDM, the Finite Element Method, FEM and the Finite Volume Method, FVM. For the FEM and the FVM, the technique reminds of the spectral approach but differs in the expansion basis functions. One of the advantage of the finite methods, is that the grid does not need to have a regular shape, and the elements do not need to be equidistants, however, we will not make use of that in this work. The finite methods solve the PDE locally while the spectral method is global i.e the function value at a point x_i depends on the interval of the subdomains, while in a global method, the function value is dependant of the entire domain (Costa, 2004).

4.1 The Finite Difference Method

It consists in the approximation of the derivatives of a differential or partial differential equation by finite differences. Let $f'(x)$ be the derivative of the function f, that we want to approximate at the point x. Then :

$$\begin{aligned} f'(x) &= \lim_{\Delta x->0} \frac{f(x+\Delta x)-f(x)}{\Delta x} \\ &= \lim_{\Delta x->0} \frac{f(x)-f(x-\Delta x)}{\Delta x} \\ &= \lim_{\Delta x->0} \frac{f(x+\frac{1}{2}\Delta x)-f(x-\frac{1}{2}\Delta x)}{2\Delta x} \qquad (4.1) \end{aligned}$$

where all the expression are equivalent to the expression of the derivative of f at the point x, when $\Delta x- > 0$ (Peiro and Sherwin, 2005).

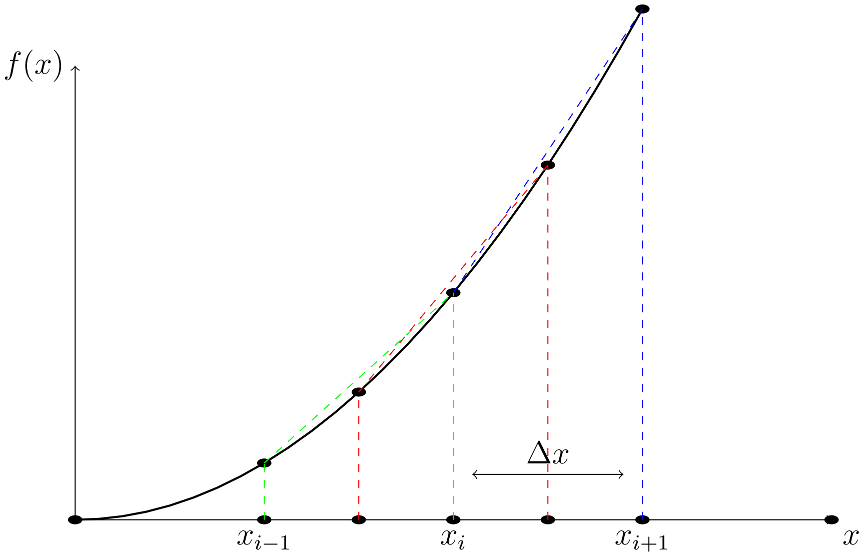

Figure 4.1: FDM

When the system has to be solved numerically, the derivative can no longer be found as in the continuous case seen above, and the domain of definition of f needs to be discretised . Let $f_i = f(x_i)$ be the value of the function at the i_{th} point of the grid. The distance between the points of the grid is given by $\Delta x_i = x_{i+1} - x_i$, or Δx when the points on the grid are equally distant. The approximation becomes:

$$\begin{aligned} f'(x) &\approx \frac{f(x_i+\Delta x)-f(x_i)}{\Delta x} = \frac{f_{i+1}-f_i}{\Delta x} \quad (forward) & (4.2)\\ &\approx \frac{f(x_i)-f(x_i-\Delta x)}{\Delta x} = \frac{f_i-f_{i-1}}{\Delta x} \quad (backward) & (4.3)\\ &\approx \frac{f(x_i+\Delta x)+f(x_i-\Delta x)}{2\Delta x} = \frac{f_{i+1}+f_{i-1}}{2\Delta x} \quad (centered) & (4.4) \end{aligned}$$

To illustrate the method, we can look at the Dirichlet problem in 1D. Let v be a function defined on an interval Ω between a and b, and v'' its second derivative, we then have:

$$\begin{aligned} v''(x) = f(x), x \in]0,1[\\ v(0) = v(1) = 0 \end{aligned} \tag{4.5}$$

We want to approximate $v''(x)$, and start by looking at a taylor expansion around x_i:

$$\begin{aligned} v(x_{i+1}) &= v(x_i) + \Delta x v'(x_i) + \frac{\Delta x^2}{2} v''(x_i) + \frac{\Delta x^3}{6} v'''(x_i) + ... \\ v(x_{i-1}) &= v(x_i) - \Delta x v'(x_i) + \frac{\Delta x^2}{2} v''(x_i) - \frac{\Delta x^3}{6} v'''(x_i) + ... \end{aligned} \tag{4.6}$$

We can then approximate $f(x_i)$ with :

$$f(x_i) = v''(x_i) \approx \frac{v(x_{i+1}) + v(x_{i-1}) - 2v(x_i)}{\Delta x^2} \tag{4.7}$$

While the FDM is expressed in a differential formulation, the FEM and FVM are in the integral form.

4.2 The Finite Element Method

First is the domain Ω discretised into $N-1$ subdomains $\Omega_i = \{x : x_{i-1} < x < x_i\}$, called elements (Peiro and Sherwin, 2005). The idea is to approximate a function ϕ in terms of some basic functions ϕ:

$$\phi(x) = \sum_{i=1}^{N} c_i \phi_i(x) \tag{4.8}$$

where c_i are coefficients. It is common to choose the basis functions ϕ so that the value of the coefficients c_i are the same as the function value at the i_{th} point of the grid, which corresponds to an expansion basis as:

$$\phi_i(x_j) = \delta_{ij} = \begin{cases} 1 & \text{if } i = j \\ 0 & \text{if } i \neq j \end{cases} \tag{4.9}$$

from which:

$$\phi_i = \begin{cases} \frac{x - x_{i-1}}{x_i - x_{i-1}} = \frac{x - x_{i-1}}{\Omega_{i-1}} & \text{for } x_{i-1} < x < x_i \\ \frac{x_{i+1} - x}{x_{i+1} - x_i} = \frac{x_{i+1} - x}{\Omega_i} & \text{for } x_i < x < x_{i+1} \\ 0 & \text{elsewhere} \end{cases} \tag{4.10}$$

and

$$\phi_i' = \begin{cases} \frac{1}{x_i - x_{i-1}} = \frac{1}{\Omega_{i-1}} & \text{for } x_{i-1} < x < x_i \\ \frac{-1}{x_{i+1} - x_i} = \frac{-1}{\Omega_i} & \text{for } x_i < x < x_{i+1} \\ 0 & \text{elsewhere} \end{cases} \tag{4.11}$$

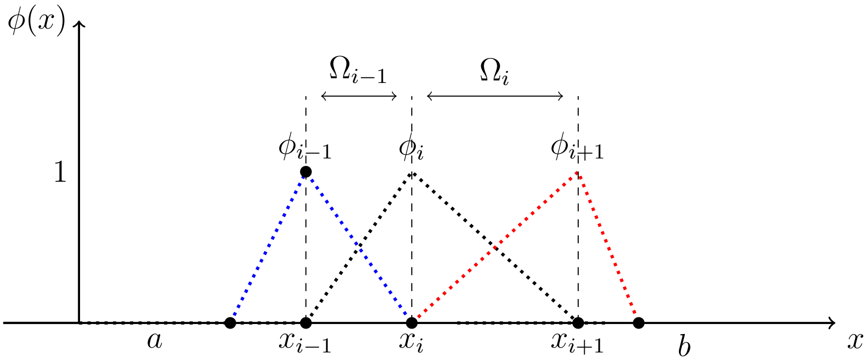

Figure 4.2: Basis functions of FEM on a non equidistant grid.

We look at problem 4.5. We need to find a function v that solves:

$$\int_a^b \omega(x) v''(x) dx = \int_a^b \omega(x) f(x) dx \tag{4.12}$$

the left hand side can be integrated by parts :

$$-\int_a^b v'(x)\omega'(x) dx = \int_a^b \omega(x) f(x) dx \tag{4.13}$$

Using relation 4.8 and equations 4.10 and 4.11 , and letting $v(x) = \sum_{j=1}^{N} v_j \phi_j$ and $\omega(x) = \phi_i(x)$ for $i = 2, ..., N$, we find:

$$-\int_a^b \phi_i'(x) \sum_{j=1}^{N} c_j \phi_j'(x) dx = \int_a^b \phi_i(x) f(x) dx \tag{4.14}$$

which yields to :

$$\begin{aligned} -\int_{x_{i-1}}^{x_i} \phi_i'(x)(c_{i-1}\phi_{i-1}'(x) + c_i\phi_i'(x))dx - \int_{x_i}^{x_{i+1}} \phi_i'(x)(c_i\phi_i'(x) + c_{i+1}\phi_{i+1}'(x))dx \\ = \int_{x_{i-1}}^{x_i} \phi_i(x) f(x) dx + \int_{x_i}^{x_{i+1}} \phi_i(x) f(x) dx \end{aligned} \tag{4.15}$$

Using 4.10 and 4.11, it can be shown that the approximation to the problem is the same as the one found with help of the FDM if the elements are equidistants (Peiro and Sherwin, 2005).

4.3 The Finite Volume Method

Here is the space also discretised, it is divided into a mesh, that can either be vertex centered or cell centered (see Figure 4.3). The elements of the mesh are called control volumes Ω_i , the blue regions in figures 4.3(a) and 4.3(b). These control volumes are each associated to a point x_i, that in a cell centered scheme is such that $x_i = \frac{x_{i+\frac{1}{2}}+x_{i-\frac{1}{2}}}{2}$ where i is the index of the interface. In a finite volume scheme, the flux is locally conservative, i.e. the flux on the boundary of a cell has to be the same on both sides of the interface.

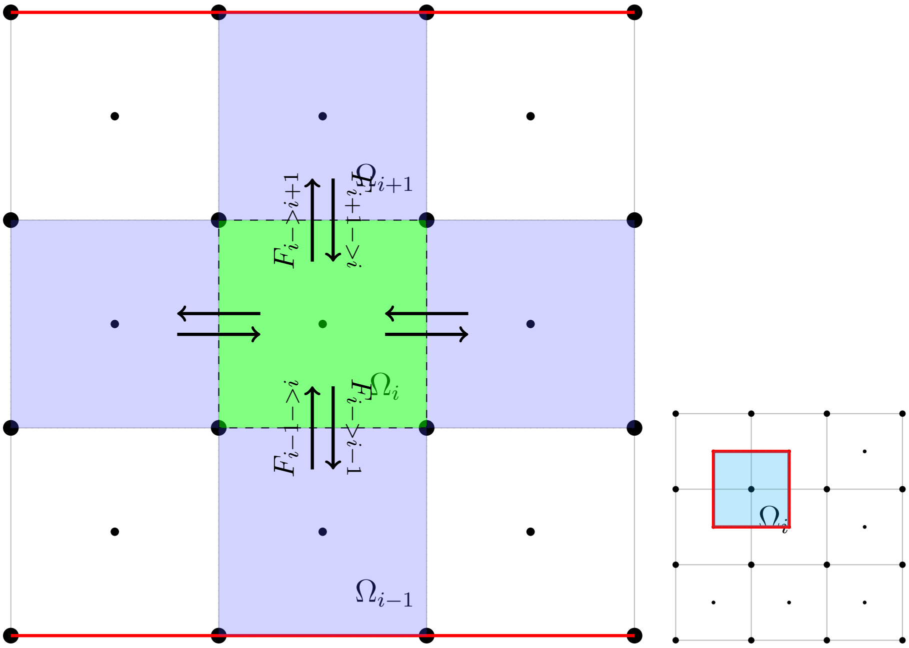

(a) Cell centered (b) Vertex centered

Figure 4.3: Flux exchange at the interfaces

We look at the same example as previously 4.5. The control volumes Ω_i are defined for an x such that $\{x_{i-\frac{1}{2}} \leq x \leq x_{i+\frac{1}{2}}\}$. We have:

$$\int_{x_{1-\frac{1}{2}}}^{x_{1+\frac{1}{2}}} v''(x)dx = \int_{x_{1-\frac{1}{2}}}^{x_{1+\frac{1}{2}}} f(x)dx \tag{4.16}$$

The right hand side can be found with help of the approximation by the middle value of the function f at the cell surface of the control volume Ω_i :

$$f(x_i) = \frac{1}{d_i} \int_{x_{1-\frac{1}{2}}}^{x_{1+\frac{1}{2}}} f(x)dx \tag{4.17}$$

where $\Delta_{i+\frac{1}{2}} = x_{i+\frac{1}{2}} - x_{i-\frac{1}{2}}$ and $\Delta_{i+\frac{1}{2}} f(x_i) = \int_{x_{1-\frac{1}{2}}}^{x_{1+\frac{1}{2}}} f(x)dx$. Equation 4.16 becomes:

$$v'(x_{1-\frac{1}{2}}) - v'(x_{1+\frac{1}{2}}) = \Delta x_{i+\frac{1}{2}} f(x_i) \tag{4.18}$$

the left hand side can be approximated with help of the FDM and we end with:

$$\frac{v_{i+1} - v(x_i)}{\Delta x_i} - \frac{v(x_i) - v(x_{i-1})}{\Delta x_{i-1}} = \Delta x_{i+\frac{1}{2}} f(x_i) \tag{4.19}$$

If the grid is equidistant, we find again the same as with the FEM and FDM.

$$f(x_i) = \frac{v(x_{i+1}) + v(x_{i-1}) - 2v(x_i)}{\Delta x^2} \tag{4.20}$$

Chapter 5

Combined finite volume and spectral method

We return to the model equation 1.1 without the source term and investigate a method that combines two of the presented numerical methods in the previous chapters. Because we are working with transport of flux on a sphere, that involves many complicated processes, we want to use a conservative scheme such as a finite volume method. We are interesting in a method that can perform faster than with the spherical harmonics alone, but we still want to make use of the rotation symmetry of the sphere by including the eigenfunctions of a differential operator on a unit sphere. On this basis, a combined finite volume and spectral method seems to fulfill our wish. Furthermore, this might minise eventual approximations errors due to the calculations of the many integrals we have seen in chapter 3. The differential rotation, that does not require many integrals approximations, and have constant coefficients, could be approximated by a spectral decomposition. We will therefore use a combined method, where the finite volume approach is used along the colatitude, and the spectral method along the longitude as illustrated in Figure 5.1.

The flux transport equation can be written as a sum of the evolution in the θ direction and in the ϕ direction:

$$\frac{\partial B_r}{\partial t} = \underbrace{[\underbrace{\frac{D}{\sin\theta}\frac{\partial}{\partial\theta}(\sin\theta\frac{\partial B_r}{\partial\theta})}_{\text{diffusion}} - \underbrace{\frac{1}{\sin\theta}\frac{\partial}{\partial\theta}(\sin\theta v(\theta)B_r)]}_{\text{meridional flow}}}_{\text{North - South}} + \underbrace{[\underbrace{\frac{D}{\sin^2\theta}\frac{\partial^2 B_r}{\partial\phi^2})}_{\text{diffusion}} - \underbrace{\omega(\theta)\frac{\partial B_r}{\partial\phi}}_{\text{differential rotation}}}_{\text{East - West}} \tag{5.1}$$

We can see that the magnetic field in the North - South direction, along θ, is governed by the meridional flow and the diffusion, while the differential rotation and the zonal diffusion make the magnetic field to move in an East - West direction, along ϕ.

We are still seeking a solution to equation 5.1 of the form:

$$B(\theta,\phi,t) = \sum_{l}^{lmax} B_l(\theta,t)e^{il\phi} \tag{5.2}$$

where $B_l(\theta,t)$ is a complex function. Here will B_l be approximated with a finite volume and is therefore a function of θ and the time t, while in the spherical harmonics approach, the coefficients $a_l^m(t)$ are expanded in Legendre polynomials and are function of the time.

Inserting 5.2 into equation 5.1 we can see that the PDE becomes :

$$\frac{dB_l}{dt} = \underbrace{\frac{D}{\sin\theta}\frac{\partial}{\partial\theta}(\sin\theta\frac{\partial B_l}{\partial\theta}) - \frac{1}{\sin\theta}\frac{\partial}{\partial\theta}(\sin\theta v(\theta)B_l)}_{\text{North - South}} - \underbrace{(il\omega(\theta) + \frac{D}{\sin^2\theta}l^2)B_l}_{\text{East - West}} \tag{5.3}$$

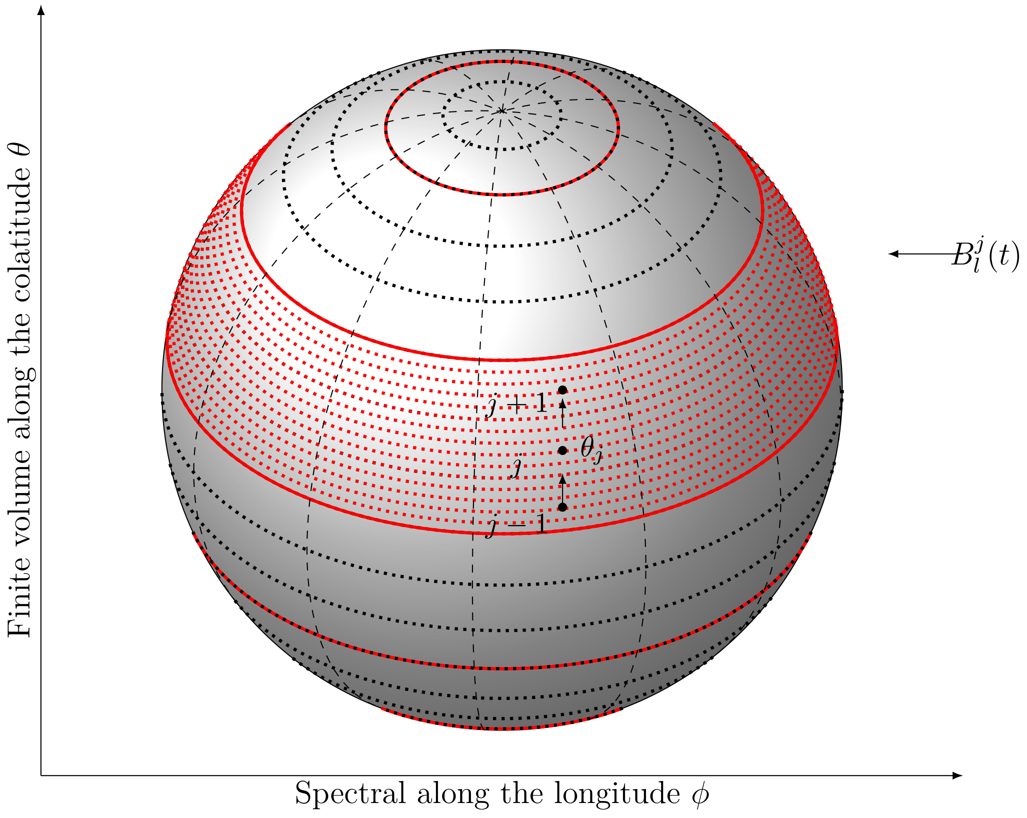

Figure 5.1: Discretisation

The flux transported from one cell to another is calculated with help of a

centered finite difference approximation (see section 4.1). First is the colatitude divided into N cells, j, which interfaces $\theta_{j+\frac{1}{2}}$, are such that $\theta_{\frac{1}{2}=0}$ and $\theta_{N+\frac{1}{2}} = \pi$. The flux taken in consideration is the amount of flux across the interfaces, called θ_j, and defined as $\theta_j = \frac{1}{2}(\theta_{j-\frac{1}{2}} + \theta_{j+\frac{1}{2}})$. The distance, d, between each cell j, is given by $d^{j,j+1} = R(\theta_{j+1} - \theta j)$ and the area of each cell is equal to $A^j = \pi R^2(\cos\theta_{j+\frac{1}{2}} - \cos\theta_{j-\frac{1}{2}})$ (see figure 5.2).
We also need to know the average value in each cell, that we define as :

$$\bar{B}_l^j(t) = \frac{B_l^j(t)}{A^j} \tag{5.4}$$

Now, $B_l^j(t)$ corresponds to the portion of magnetic field , along ϕ between the interfaces $\theta_{j-\frac{1}{2}}$ and $\theta_{j+\frac{1}{2}}$ of cell j (see figure 5.1 and figure 5.2) for the wavenumber l, and can be found with help of the desired solution given in equation 5.2 that we integrate with respect to the surface of the sphere .

$$\begin{aligned} B_l^j(t) &= \int_S B_l(\theta,t)e^{il\theta}dS \\ &= 2\pi R^2 \int_{\theta_{j-\frac{1}{2}}}^{\theta_{j+\frac{1}{2}}} B_l(\theta,t)\sin(\theta)d\theta \end{aligned} \tag{5.5}$$

For each wavenumber l, and cell j, equation 5.3 can then be written as:

$$\dot{B}_l^j = \underbrace{J_l^{j-\frac{1}{2}} - J_l^{j+\frac{1}{2}}}_{\text{North - South}} \underbrace{- (il\omega(\theta_j) - \frac{D}{R^2\sin^2\theta_j}l^2)B_l^j}_{\text{East - West}} \tag{5.6}$$

where $J_l^{j-\frac{1}{2}}$ is the flux that is transported from cell $j-1$ to cell j through the interface $\theta_{j-\frac{1}{2}}$ and $J_l^{j+\frac{1}{2}}$ is the flux from cell j to cell $j+1$ (See figure 5.2). As seen in equation 5.1, the flux that goes in the North - South direction is convective and contains a diffusion part and an advective part in the form of the meridional flow.

North - South

The flux approximation of the diffusive part that enters cell $j+1$ through the interface $\theta_{j+\frac{1}{2}}$ becomes :

$$J_l^{Dif,j+\frac{1}{2}} = D\frac{\bar{B}_l^j - \bar{B}_l^{j+1}}{d^{j,j+1}} 2\pi R\sin\theta_j \tag{5.7}$$

For the approximation of the advective flux that is transported between cell j and $j+1$, the centered scheme is replaced by the upwind scheme. When the velocity of the meridional flow $v(\theta)$ is positive, the flux goes from cell j to $j+1$, when negative, it goes from cell $j+1$ to cell j.

$$\begin{aligned} J_l^{Ad_{j,j+1}} &= v(\theta_{j+\frac{1}{2}})\bar{B}_l^j 2\pi R sin(\theta_{j+\frac{1}{2}}) \\ J_l^{Ad_{j+1,j}} &= v(\theta_{j+\frac{1}{2}})\bar{B}_l^{j+1} 2\pi R sin(\theta_{j+\frac{1}{2}}) \end{aligned} \tag{5.8}$$

The total flux that goes from cell j to $j+1$ is then:

$$J_l^{j+\frac{1}{2}} = J_l^{Ad^+_{j,j+1}} + J_l^{Ad^-_{j+1,j}} + J_l^{Dif,j+\frac{1}{2}} \tag{5.9}$$

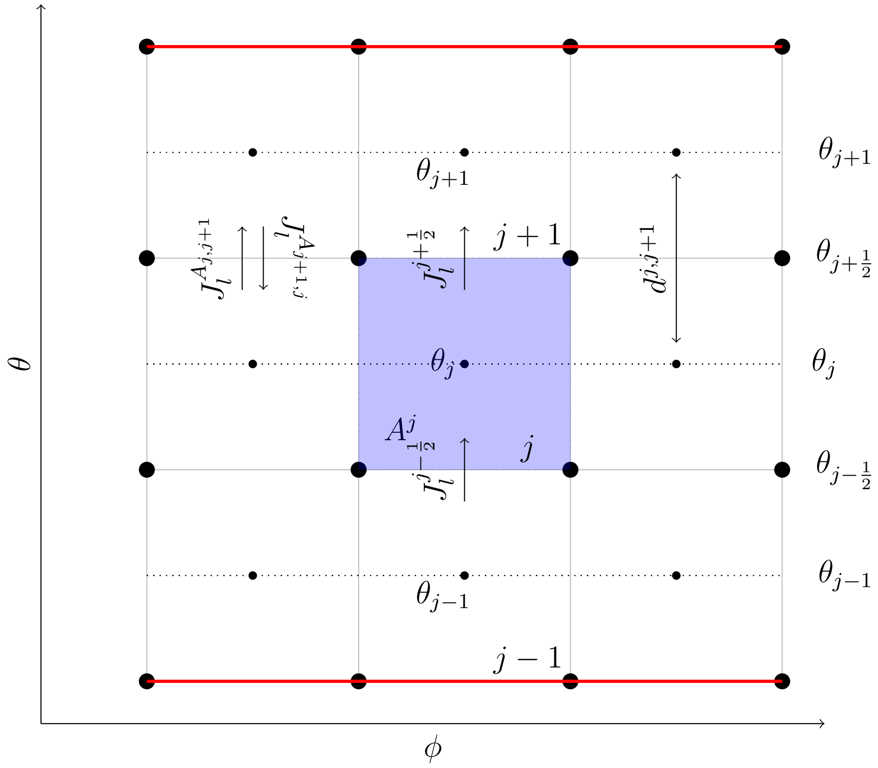

Figure 5.2: Cell geometry and flux exchange

East - West

In the East - West direction, we have for each m, the effect of the differential rotation and the diffusion along the latitude. It is equal for each cell all along a same wavenumber m and is therefore represented by a diagonal matrix, that we call Z :

$$Z_l^{j,j} = -il\omega(\theta_j) - \frac{D}{R^2 \sin(\theta_j)^2} l^2 \tag{5.10}$$

We can now contrusct the system matrice A, $A = J + Z$.
We obtain a system of differential equations for the coefficients:

$$\dot{B}_l(t) = AB_l(t) \tag{5.11}$$

For each t, we need to calculate :

$$\dot{B}_l(t) = \sum_{l=0}^{l=lmax} \exp(At) B_l(t) \tag{5.12}$$

We therefore end by solving a system of l = (lmax + 1) equations, while with the spherical harmonics method, the coefficients $a_l^m(t)$ need to be defined for each m and l, resulting in a system of $(\text{lmax} + 1)^2$ equations to solve when working with real spherical harmonics, and $\frac{(\text{lmax}+1)(\text{lmax}+2)}{2}$ when the coefficients are in their complex form (Baumann, 2005).

We have here developed an unusual scheme for solving a PDE on a sphere. It is clear that the use of a finite volume method reduces considerably the number of numerical integral approximations, and might perform faster especially when using a high value of wavenumbers.
We are not aware of previous work that has combined a finite volume and spectral method in that way, neither in the present context of magnetic flux transport on the solar surface, nor in other context. It is therefore highly interesting to see if we can validate the model through some tests that we will run in the next chapter.

Chapter 6

Validation of the model

In this chapter, we will perform some tests that can verify specifically the different processes. We will evaluate the model, with parameter values based on the simulations made by van Ballegooijen et al. (1998) and Mackay et al. (2004). The wavenumber used for both methods is lmax = 63, which should be sufficient for representing the structure of the solar supergranular cells (Mackay et al., 2004).

The tests of the two different methods will be compared by using the same initial fields and the same number of grids cells. We will use a grid with 64 cells for the colatitude and 128 cells for the longitude. The time unit will be 1 rotation, 27 days, corresponding to an average of the different values at the different latitudes. The tests for the spectral method on the left, that we call SH method, and those for the finite volume combined with spectral, called FVS, on the right. Note that the color scale is not fixed for a given value, which permits one to see the whole evolution during 36 rotations. Furthermore, the colors can slightly diverge between the two figures for each time t, because the field is not propagated at the exactly same speed despite of similar timescales and parameters. This reflects the differences betwen the two methods. We have decided to prioritise the visibility of the repartition of the magnetic field as a function of the time above the opportunity of comparing directly the strength of the field in the plots that illustrates the two methods. The simulations are performed in the units km per seconds and radians per seconds, unless something else is specified.

6.1 Simulation of the flux transport model

We will start by testing the differential rotation, then the meridional flow, and at least, a bipole. We have chosen some artificial initial fluxes with the only purpose to see the field evolve according to the respective processes.

6.2 Diffusion

The diffusion coefficient D is set to be 500 km$^2 s^{-1}$, which corresponds to a timescale in the order of $\frac{R^2}{D} \approx 30$ years. The diffusion dissipates the magnetic field with time. We will not perform any test with the only purpose to control the effect of the diffusion, but it will be involved in all the tests.

6.3 Zonal flow : differential rotation

The differential rotation operates in an East - West direction and makes the field evolve faster around the equator than at the poles (See figure 3 and figure 6.1). The period of rotation for the Sun is about 25 days at the equator and 35 days at the poles Jones (1993). Its timescale is of the order of $\frac{2\pi}{\omega(0)-\omega(\frac{\pi}{2})} \approx 100$ days, i.e. it is the lowest common multiple for the rotation time at the equator and near the poles, as seen on figure 6.1.

The profile of the differential rotation that is used, its the one defined by Snodgrass (1983) :

$$\omega(\theta) = (13.38 - 2.30\cos^2\theta - 1.62\cos^4\theta)\frac{\pi}{180}\frac{1}{86400} \quad \text{rads}^{-1} \tag{6.1}$$

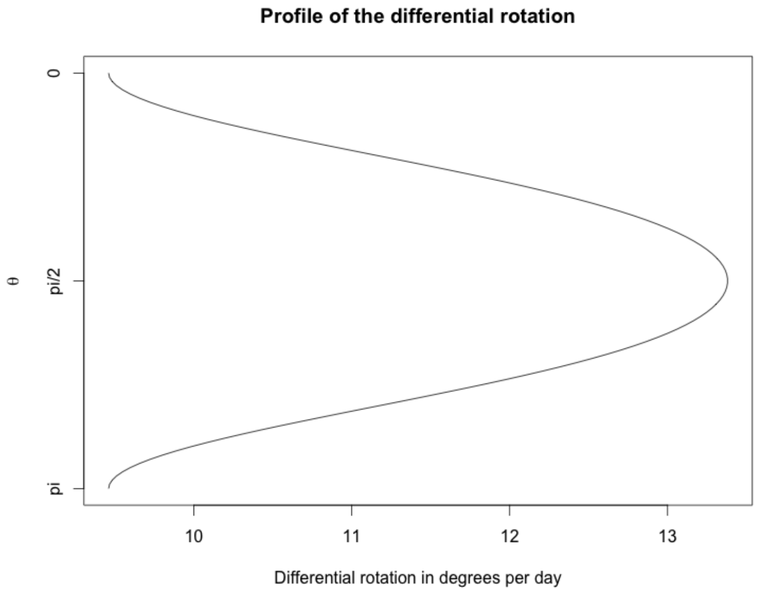

Figure 6.1: Differential rotation profile

Figure 6.1 illustrates that the rotation at the equator, at $\theta = \frac{\pi}{2}$ on the figure, is faster than at the poles.

In this test, we use as initial value a magnetic field of 500 Gauss that is concentrated in the first meridian. We make the field evolve afterwards until the effect of the differential rotation has stopped. We can see on figure 6.3, that the FVS method reproduces best the intial field. However, the field evolves at similar speed and we recognize on figures 6.4 to figures 6.7, the profile of the differential rotation (figure 6.1). Another recognisable feature is that for each rotation, the field at the equator is at the same position, while the field at the poles is moving slower, until a period of 4 rotations, around 100 days, where the flux at the poles and the flux at the equator are both at their initial position, as it should be according to the timescale of the profile. After 6 rotations the field begins to separate into bands and migrate towards the poles, as it should do under the effect of the differential rotation according to Mackay and Yeates (2012). It is clear that after 12 rotations, the flux is moving slower with the SH method (see figure 6.9). At this time, the flux is already concentrated at the pole with the FVS method, while it is still moving around the sphere with the SH method. However after 24 - 36 rotations, the field is at the poles only, with both approaches (figures 6.10, 6.11).

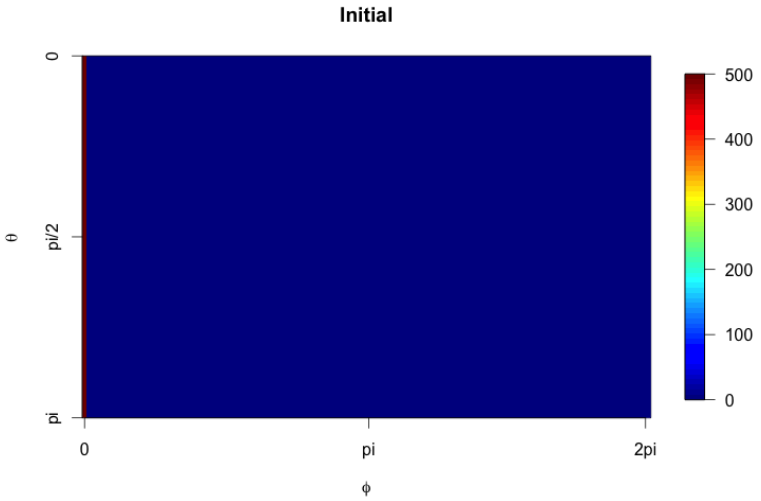

Figure 6.2: Initial field for the zonal test - all the field is concentrated in the first meridian.

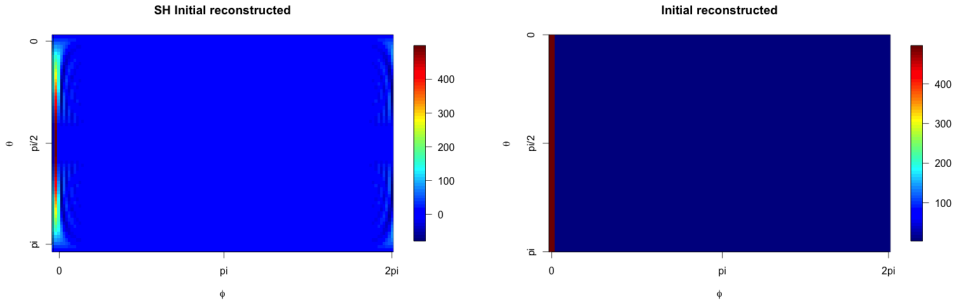

(a) Spherical Harmonics

(b) Finite Volume - Spectral

Figure 6.3: Reconstruction

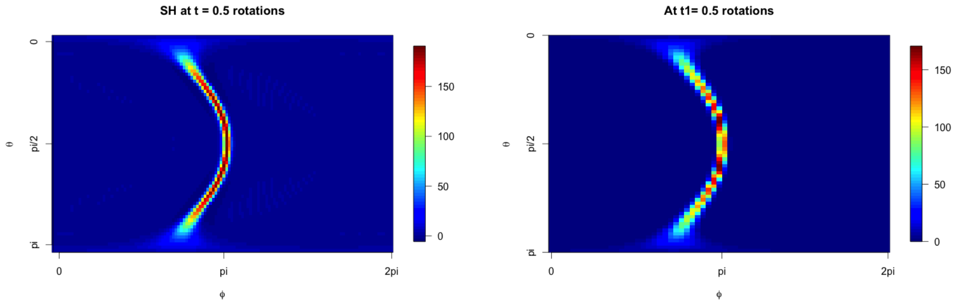

(a) Spherical Harmonics (b) Finite Volume - Spectral

Figure 6.4: 0.5 Rotation
Note: The color scale can differ on the pictures

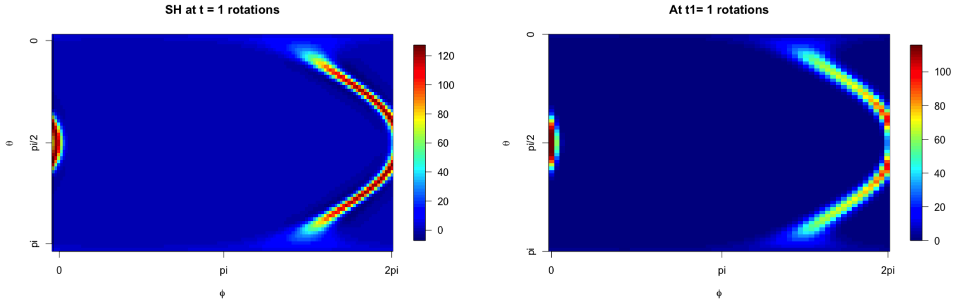

(a) Spherical Harmonics (b) Finite Volume - Spectral

Figure 6.5: 1 Rotation
Note: The color scale can differ on the pictures

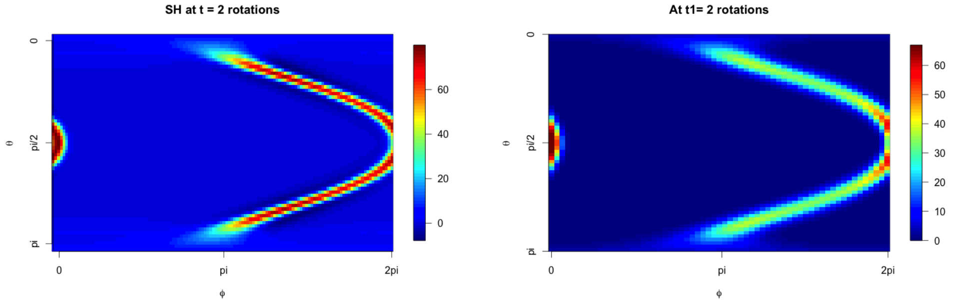

(a) Spherical Harmonics (b) Finite Volume - Spectral

Figure 6.6: 2 Rotations
Note: The color scale can differ on the pictures

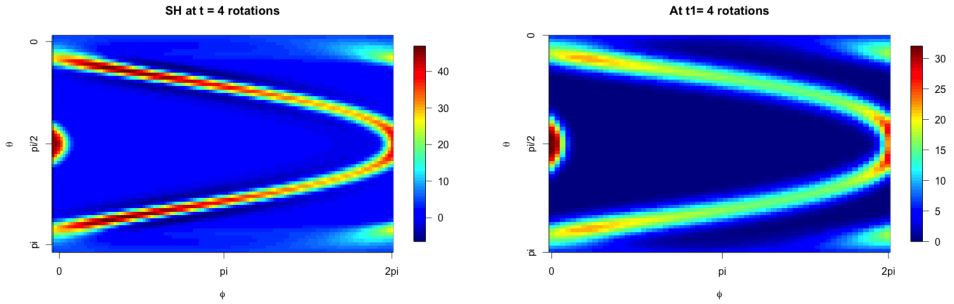

(a) Spherical Harmonics (b) Finite Volume - Spectral

Figure 6.7: 4 Rotations
Note: The color scale can differ on the pictures

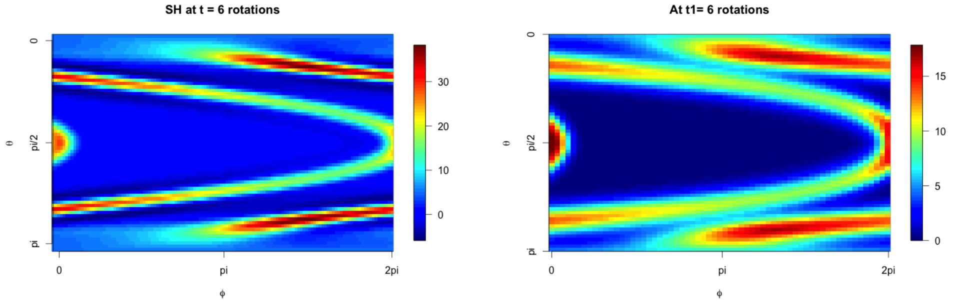

(a) Spherical Harmonics (b) Finite Volume - Spectral

Figure 6.8: 6 Rotations
Note: The color scale can differ on the pictures

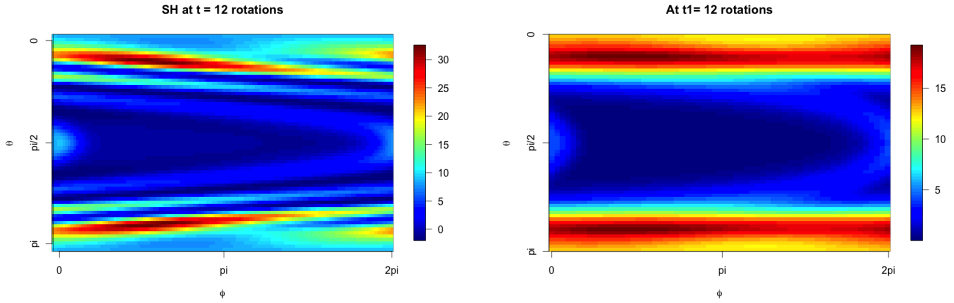

(a) Spherical Harmonics (b) Finite Volume - Spectral

Figure 6.9: 12 Rotations
Note: The color scale can differ on the pictures

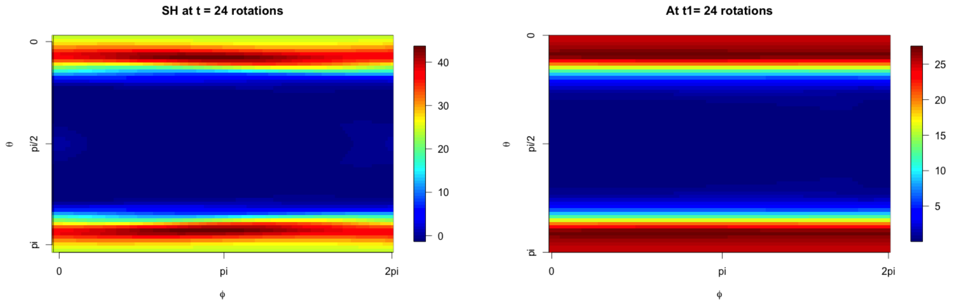

(a) Spherical Harmonics (b) Finite Volume - Spectral

Figure 6.10: 24 Rotations
Note: The color scale can differ on the pictures

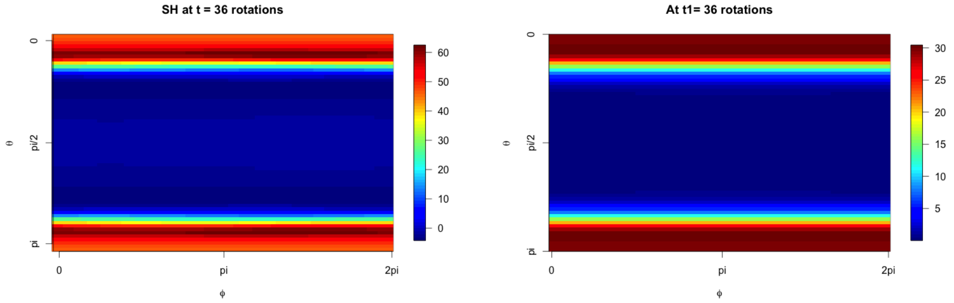

(a) Spherical Harmonics (b) Finite Volume - Spectral

Figure 6.11: 36 Rotations
Note: The color scale can differ on the pictures

6.4 Meridional flow

The meridional flow is acting in the North - South direction. This is a quite weak flow that pushes the flux polewards from the equator on the solar surface (see figure 3 and figure 6.12) and towards the equator at the interior of the Sun. In this model, we will only look at its motion on the surface. This flow is a function of the latitude , $\frac{\pi}{2} - \theta$, called λ in the litterature (van Ballegooijen et al., 1998) and a θ limit, θ_0; it only acts within a certain range of latitude for $|\theta| \leq \theta_0$. We choose to set the threshold at $\theta_0 = 75$ degrees (van Ballegooijen et al., 1998). Flux should accumulate at the pole under the effect of a combination of the supergranular diffusion and the meridional flow. The most common values are an initial advection velocity $v_0(\theta) = 0.011$ km/s. Its timescale is in the order of $\frac{R}{v_0} \approx 2$ years, meaning that it takes 2 years to transport the flux polewards. The profile of the meridional flow used for this simulation is the one described by Snodgrass and Dailey (1996) and Hathaway (1996):

$$v(\theta) = \begin{cases} -v_0 \sin(\pi \frac{(\frac{\pi}{2}-\theta)}{\theta_0}) & \text{if} \quad \theta < |\frac{\pi}{2} - \theta_0| \\ 0 & \text{otherwise} \end{cases} \tag{6.2}$$

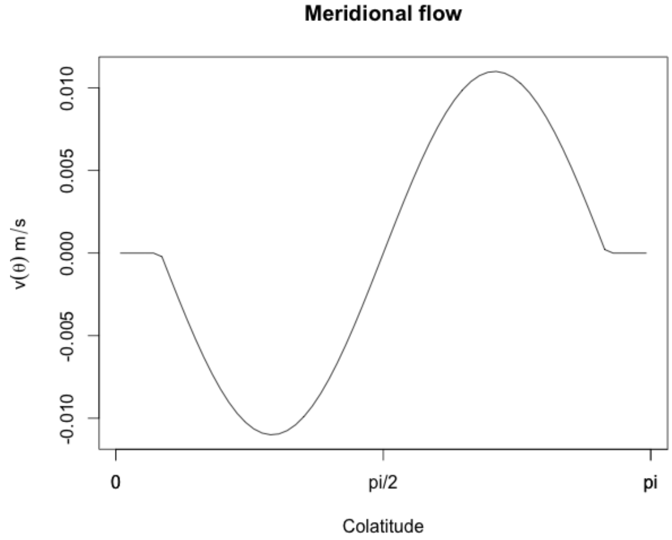

Figure 6.12: Meridional flow profile

The meridional flow is tested by placing a field of 500G in the Northern hemisphere, at a latitude of 18 degrees (see figure 6.13). Here again, both methods recontruct the field very well (see figure 6.14). After one rotation, the strength of the field is fallen quite a lot, from 500G to respectively 120G with the SH (figure 6.15(a)) and 100G with the FVS (figure 6.15(b)). The flux moves towards the pole at the same speed until 5 rotations. From 12 rotations, the SH method begins to encounter stability issues; the flux strength is growing, and moves slower than with the FVS method in addition to formation of positive flux at the pole of the opposite hemisphere (see figure 6.18(a)). The dispersal of the flux with the FVS method is in concordance with the meridional flow function (equation 6.2, and figure 6.12), flux at both side of the equator moves polewards, while it cancels out when reaching the equator. The flux migrates fastest at mid latitudes, corresponding to its position after 5 rotations as we can see on figure 6.17(b), for reaching the pole after 18 rotations. At 24 rotations has settled down and reaches a steady state between 24 and 36 rotations, corresponding to the analytical timescale of the meridional flow.

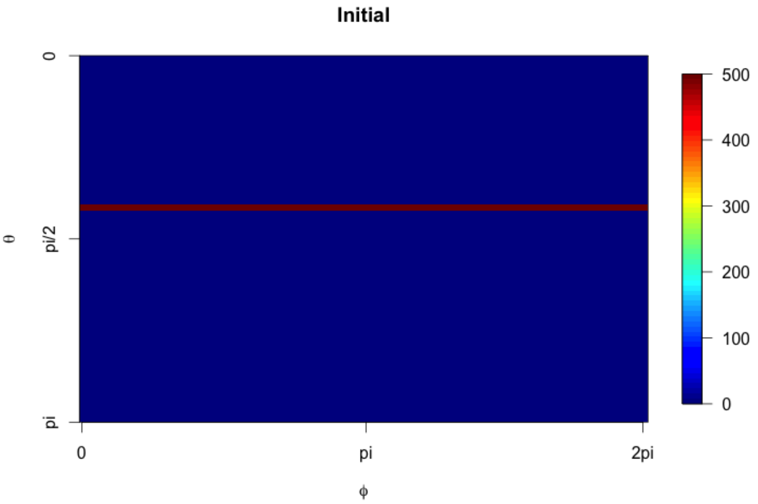

Figure 6.13: Initial Meridional flow - all the field is placed in the same parallel.

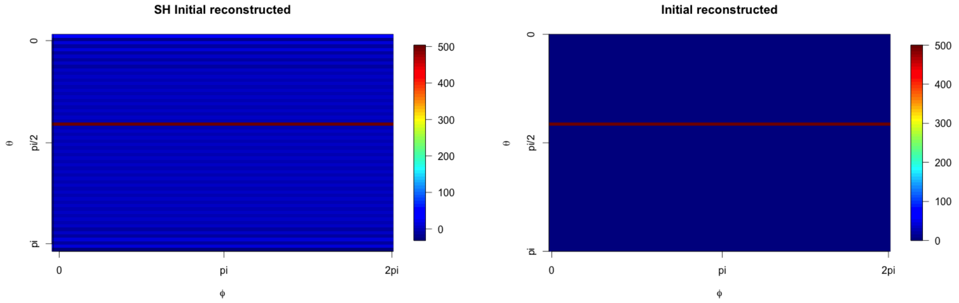

(a) Spherical Harmonics

(b) Finite Volume - Spectral

Figure 6.14: Reconstruction

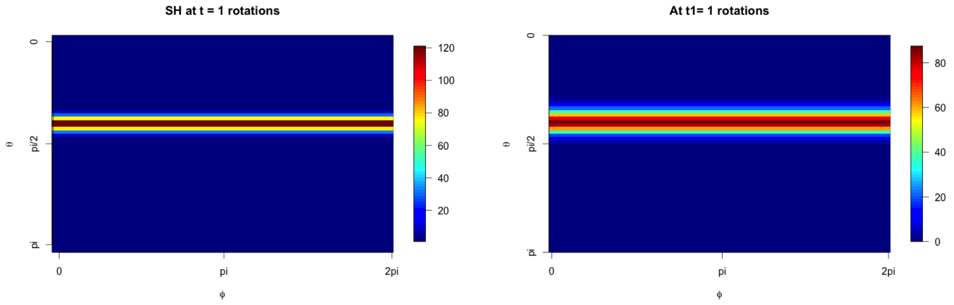

(a) Spherical Harmonics (b) Finite Volume - Spectral

Figure 6.15: 1 Rotation The color scale can differ on the pictures

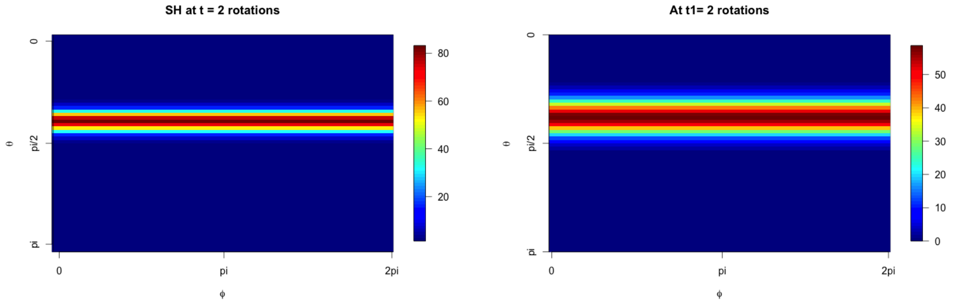

(a) Spherical Harmonics (b) Finite Volume - Spectral

Figure 6.16: 2 Rotations
Note: The color scale can differ on the pictures

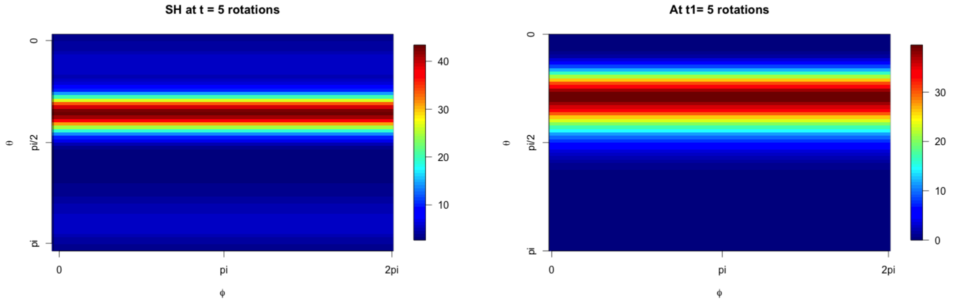

(a) Spherical Harmonics (b) Finite Volume - Spectral

Figure 6.17: 5 Rotations
Note: The color scale can differ on the pictures

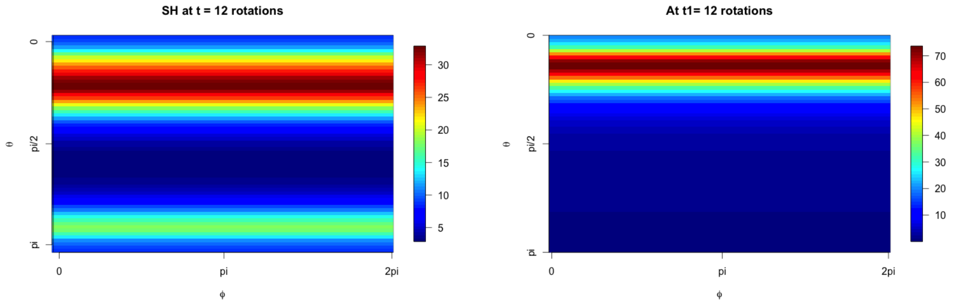

(a) Spherical Harmonics (b) Finite Volume - Spectral

Figure 6.18: 12 Rotations
Note: The color scale can differ on the pictures

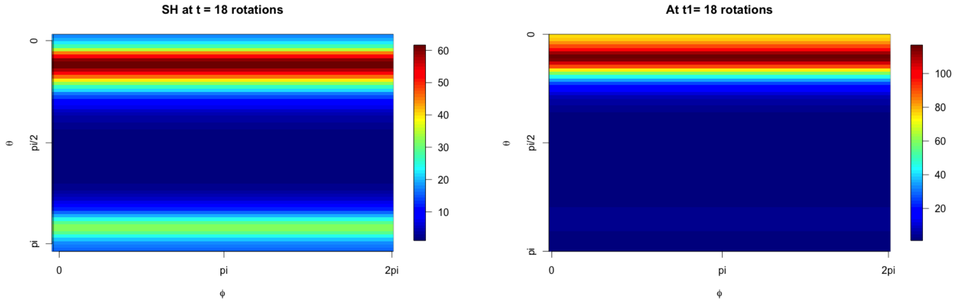

(a) Spherical Harmonics (b) Finite Volume - Spectral

Figure 6.19: 18 Rotations
Note: The color scale can differ on the pictures

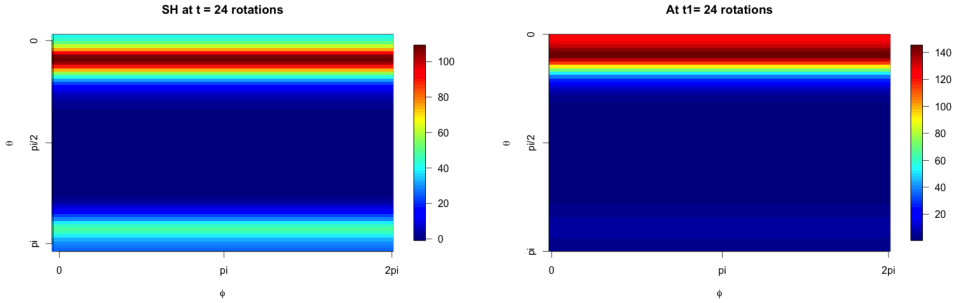

(a) Spherical Harmonics (b) Finite Volume - Spectral

Figure 6.20: 24 Rotations
Note: The color scale can differ on the pictures

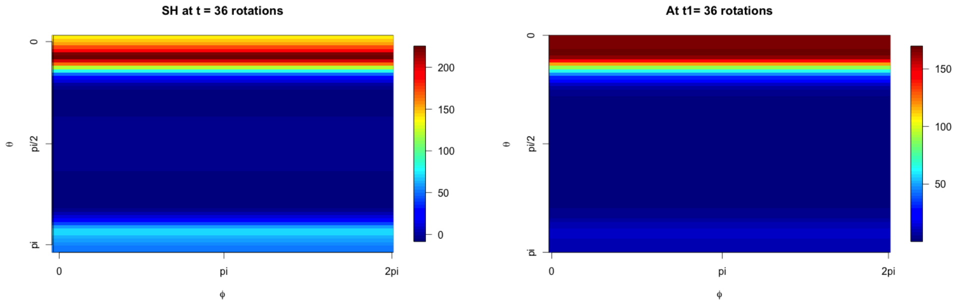

(a) Spherical Harmonics (b) Finite Volume - Spectral

Figure 6.21: 36 Rotations
Note: The color scale can differ on the pictures

6.5 Bipole

We now test all the 3 transport processes together. A bipole with an initial strength of 450G is placed in the northern hemisphere. We expect the northern spot to move towards the equator and the spot closest to the equator towards the North pole, as described by van Ballegooijen et al. (1998). The reconstruction looks alike with both methods, see figures 6.23(b). The bipole moves with the same rate using the one or the other method, until 5 rotations. From that time, we notice large differences between the methods. With the FVS, the field of the northern spot begins to accumulate at the pole, when the flux of the other spot moves towards the equator and begins to cancel out, while the separation has not occured yet with the SH as shown on figures 6.28. After 12 rotations, the diffusion should be the dominant process and makes the remaing field to acrreate at the pole while dissipating what is left. This process is well operated with the FVS method, while both spots want to accreate at the pole with the SH method (figure 6.29(a)). Figures 6.30 and 6.31 confirm this difference.

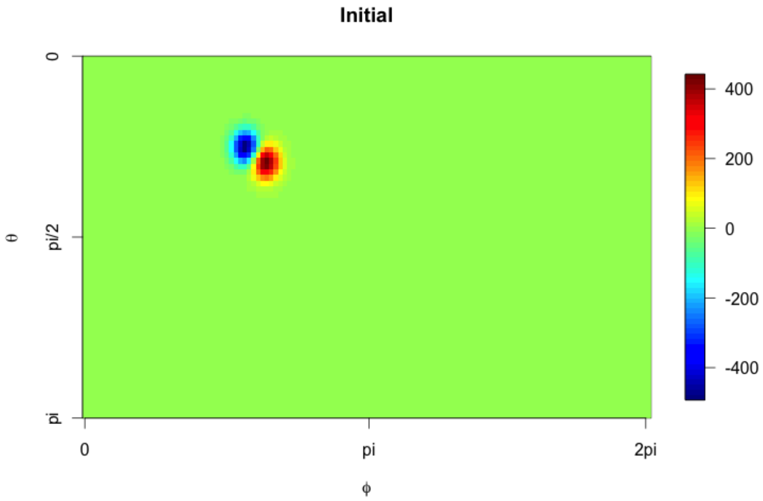

Figure 6.22: Initial bipole

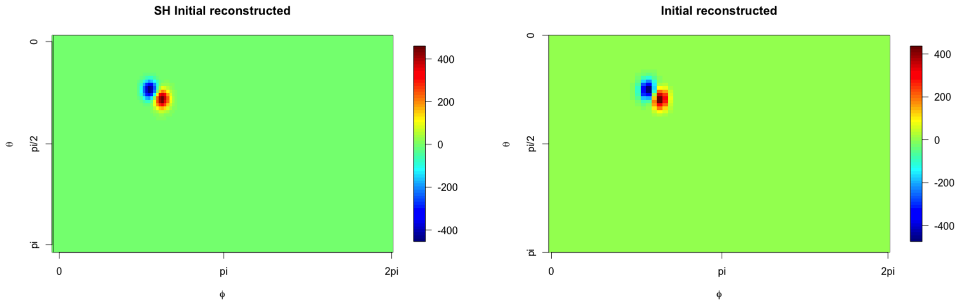

(a) Spherical Harmonics (b) Finite Volume - Spectral

Figure 6.23: Reconstruction

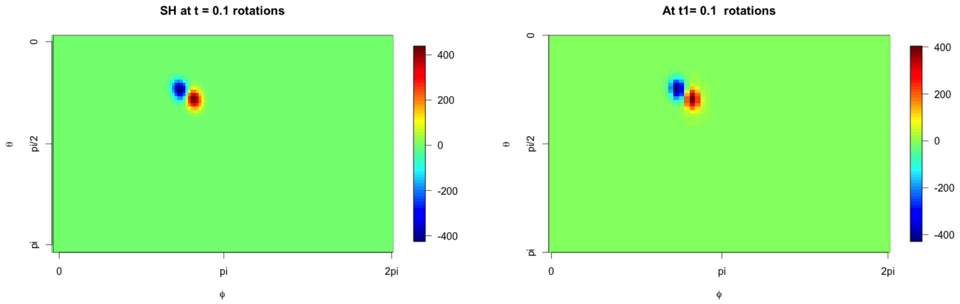

(a) Spherical Harmonics (b) Finite Volume - Spectral

Figure 6.24: 0.1 Rotation

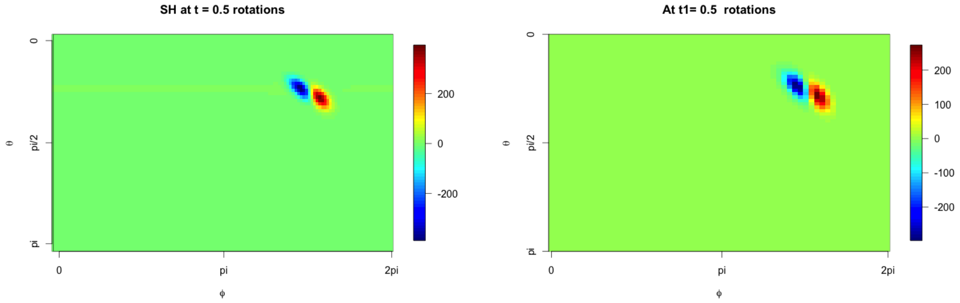

(a) Spherical Harmonics (b) Finite Volume - Spectral

Figure 6.25: 0.5 Rotation
Note: The color scale can differ on the pictures

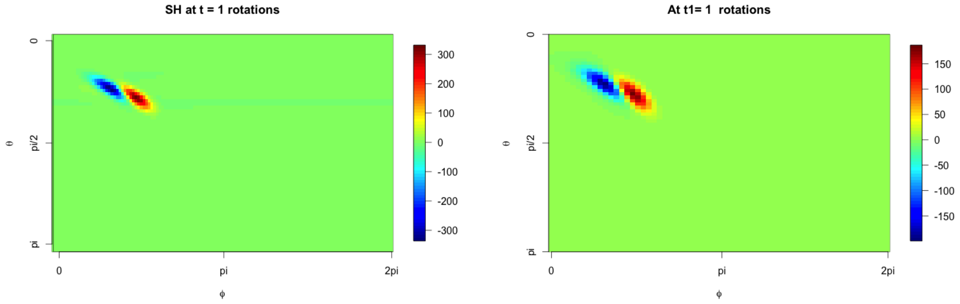

(a) Spherical Harmonics (b) Finite Volume - Spectral

Figure 6.26: 1 Rotation
Note: The color scale can differ on the pictures

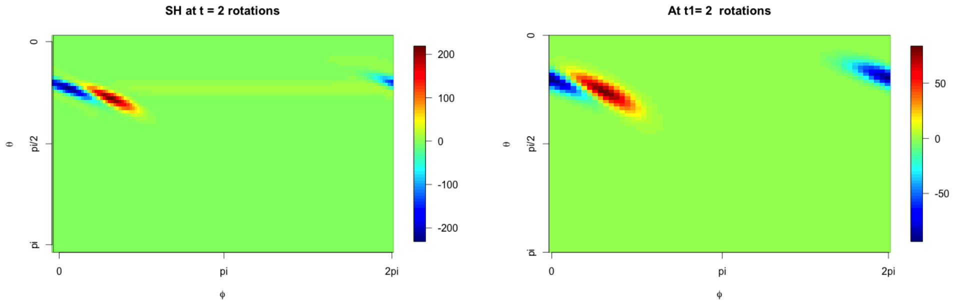

(a) Spherical Harmonics (b) Finite Volume - Spectral

Figure 6.27: 2 Rotations
Note: The color scale can differ on the pictures

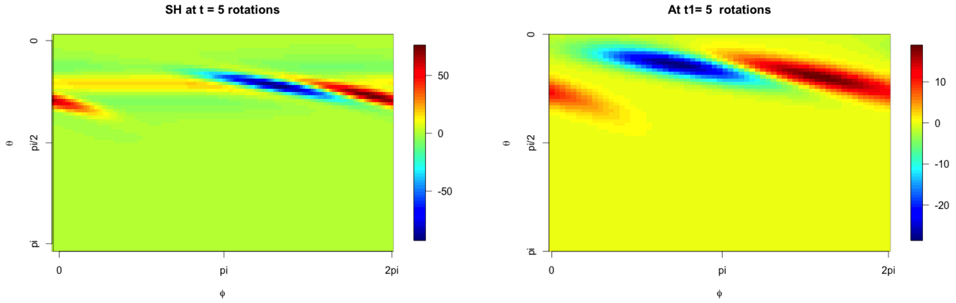

(a) Spherical Harmonics (b) Finite Volume - Spectral

Figure 6.28: 5 Rotations
Note: The color scale can differ on the pictures

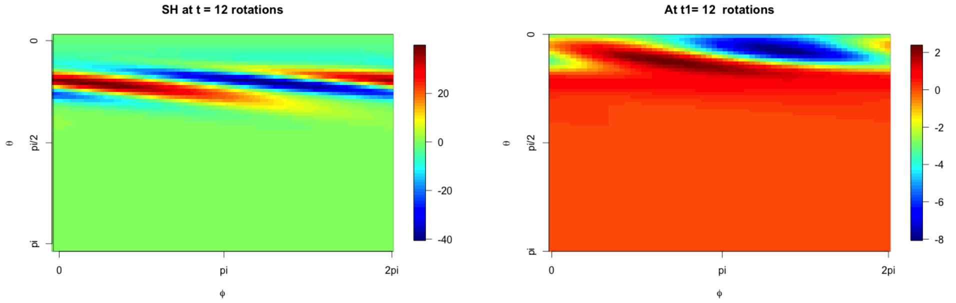

(a) Spherical Harmonics (b) Finite Volume - Spectral

Figure 6.29: 12 Rotations
Note: The color scale can differ on the pictures

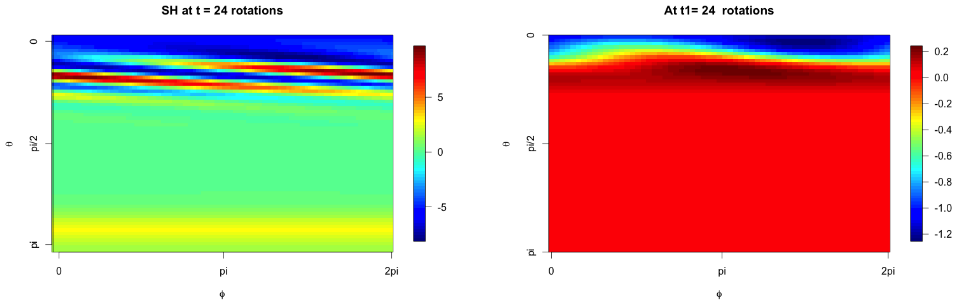

(a) Spherical Harmonics (b) Finite Volume - Spectral

Figure 6.30: 24 Rotations
Note: The color scale can differ on the pictures

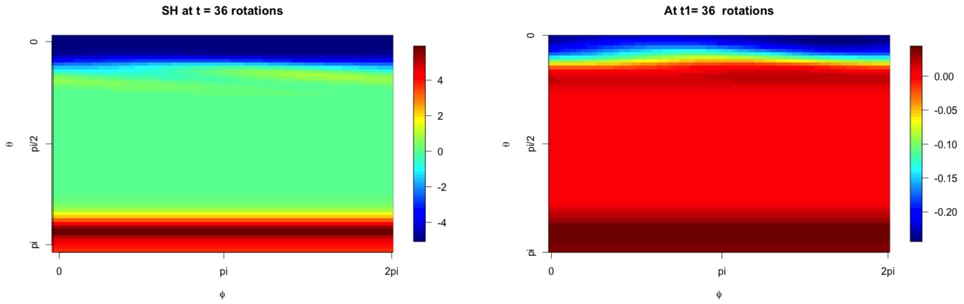

(a) Spherical Harmonics (b) Finite Volume - Spectral

Figure 6.31: 36 Rotations
Note: The color scale can differ on the pictures

Chapter 7

Summary and conclusion

Magnetic fluxes at the solar surface are mainly submitted to three different transport processes, the meridional flow that operates in the North - South direction, the differential rotation that works on the West - East direction and the supergranular diffusion, that dissipates and makes the flux, on a long timescale, to migrate polewards. A flux transport equation is used for reproducing the evolution of the magnetic flux on the Sun. Two different numerical methods for approximating the solution of a PDE have been presented. The spectral method approximates the solution with a linear combination of orthogonale basis functions. The spherical harmonics can either be complex or real. In this work, we have chosen to decompose the field into real spherical harmonics. The spherical harmonics approach is the most common method used, when dealing with transport on a sphere, because they are eigenfunctions for the spherical Laplacian operator in L^2, which is a rotationally invariant operator. In fact, the spherical harmonics scheme we have worked on, is based on the work done by (Baumann, 2005) that we have implemented in R, while other studies have used Fortran or other softwares. However, the flux transport PDE we are considering, contains a complicated advection term, involving a large number of integrations that each of them is solved by an approximation. In the model validation chapter, we have encountered stability problems with the SH method, that other work did not seem to have experienced.

The finite methods have been outlined, the finite element, the finite difference and the finite volume. We have focused on the finite volume scheme, that we have combined with a spectral method. Finite volume method, does not only ensure conservative properties, but also stability. Moreover, it permits to reduce considerably the number of integral approximations, which could be the source of the problems we experienced with the spherical harmonics method alone. One of the advantage to combine a finite volume with a spectral scheme on one direction, is a reduction of the number of control volumes, making the code more efficient than with a finit volume alone.

Furthermore, we have seen that an approximation with real SH requires to solve a system of $(\mathrm{lmax}+1)^2$ equations, $\frac{(\mathrm{lmax}+1)(\mathrm{lmax}+2)}{2}$ equations when working with complex SH, while the use of a combined finite volume - spectral method reduces the system to (lmax+1) differential equations, where lmax is the maximum number of wavenumbers. This makes the code more efficient and noticeably shorter to implement.

This uncommon scheme gave the expected results under the different tests we performed. On this basis, we decide to work with the finite volume - spectral method in the following parts of the project.

Part II

BMR emergence, a stochastic process

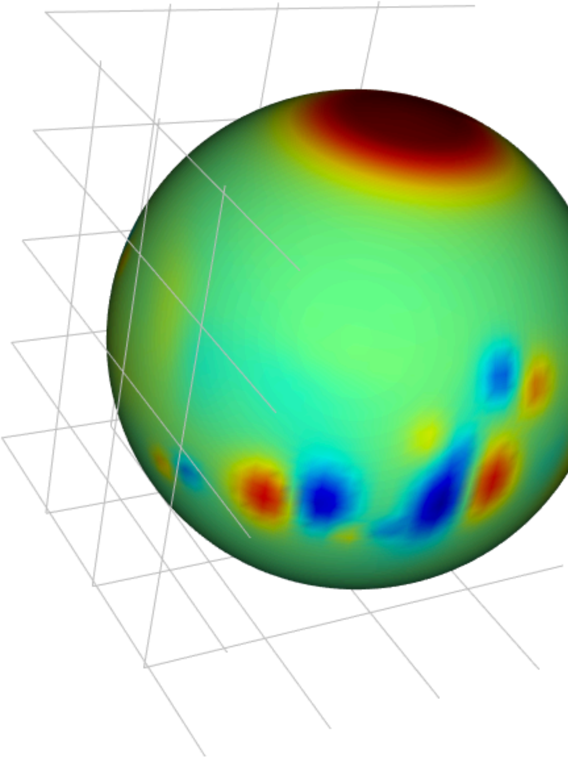

Table of Contents

Chapter 1

Introduction

In the previous chapter, we solved the transport flux equation, numerically without the source term, using a combination of a finite volume method and spectral decomposition. We now need to determine a process that can add new magnetic fluxes to the solar surface. Once we have defined this process, we will simulate the emergence and the evolution of these sources, sunspots, that appear as Bipolar Magnetic Regions, BMR. The objective is to map the evolution of the magnetic field into a light curve. The main features of the input data follow the rules and laws that have been observed (Solanki, 2003), while the parameter values will be based on observations and the real data we are going to analyse in the next part (see section 3.1 in the next chapter and part III for more details). This simulation will only consider the evolution of the spots after the time of emergence, i.e the evolution under the influence of the meridional and the zonal flow and the diffusion. In this part, the goal of the simulation is to produce a light curve which properties can be compared to a light curve from real data. The input model will therefore be both based on observations and study of the general properties for the emergence of the BMR, and properties found in the real data set, e.g we will use a 12 years cycle with 0.5 year of overlap at both ends of the cycle, where spots can emerge both at high and low latitudes, until a new cycle begins (Hathaway, 2010). One important characteristic of the sunspot cycle, is that is takes shorter time to reach a maximum than decreasing down to a minimum. We have defined the solar maximum at five years after the begining of a new cycle and a decay time from a maximum to the end of a cycle, to six years. 1 year is defined as 365 days, where 1 day is 24 hours.

1.1 New magnetic sources

New flux sources,$S(\theta, \phi, t)$ are added to the homogeneous transport flux equation 5.1 (page 34):

$$\begin{aligned}
\frac{\partial B_r}{\partial t} &= \underbrace{[\underbrace{\frac{D}{\sin\theta}\frac{\partial}{\partial\theta}(\sin\theta\frac{\partial B_r}{\partial\theta})}_{\text{diffusion}} - \underbrace{\frac{1}{\sin\theta}\frac{\partial}{\partial\theta}(\sin\theta v(\theta)B_r)]}_{\text{meridional flow}}}_{\text{North - South}} \\
&+ \underbrace{[\underbrace{\frac{D}{\sin^2\theta}\frac{\partial^2 B_r}{\partial\phi^2}}_{\text{diffusion}} - \underbrace{\omega(\theta)\frac{\partial B_r}{\partial\phi}}_{\text{differential rotation}})]}_{\text{East - West}} + \underbrace{S(\theta,\phi,t)}_{\text{Source term}}
\end{aligned} \tag{1.1}$$

These magnetic fluxes are a function of the colatitude θ, the longitude ϕ and time. Their spatial repartition depends on what stage at the solar cycle they arise. They are incorporated to the model at the time of emergence and begin to decay as they are submitted to the diffusion and advection processes at the solar surface.

1.2 Spatial properties of the BMR

Magnetic fluxes always emerge as magnetic bipole regions at the surface of the Sun within a certain range of latitude that is defined by the activity cycle stage. These pairs of spots always have opposite polarity and their strengths balance each other.

At the beginning of a cycle, the spots emerge at higher latitudes, around 40 degrees, and subsequently appearing closer and closer to the equator. This feature is commomly represented by the butterfly diagram (see figure 1.2). For each cycle, the bipoles are formed by a leading and a following spot, each of them keeping the same polarity during the whole cycle, according to Hale's law (Hale et al., 1919). The leader is always closest to the equator (Joy's law , see figure 1.1) of the same polarity for the entire cycle (Hale's law):

> *. . . the preceding and following spots of binary groups, with few exceptions, are of opposite polarity, and that the corresponding spots of such groups in the Northern and Southern hemispheres are also of opposite sign. Furthermore, the spots of the present cycle are opposite in polarity to those of the last cycle...*(Hale et al., 1919)

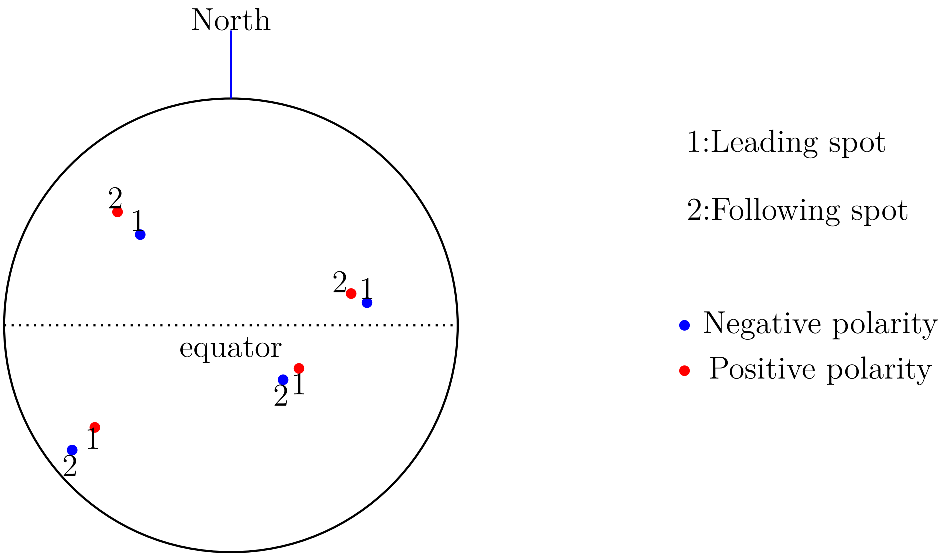

Figure 1.1: Hale's law

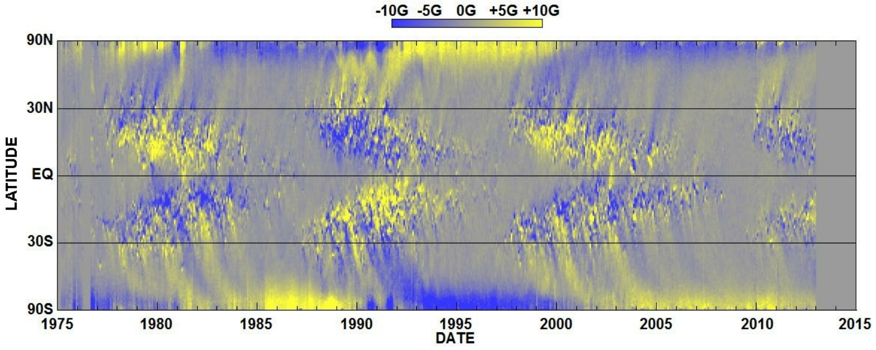

Hathaway/NASA/MSFC 2013/01

Figure 1.2: Illustration of Hale's and Joy's polarity law

The tilt angle between the two spots, is essential for the poleward transport of the flux. This is the following spot, i.e. the closest to the pole, that is transported polewards under the effet of the meridional flow while the magnetic flux of the leader is more inclined to cancel across the equator (Mackay and Yeates, 2012). It is clear from figure 1.2 that the polarity at the poles is determined by the following spot and is therefore of opposite sign at opposite poles. The polarity alternates during every solar cycle a couple of years after each solar maximum, when there is enough flux to cancel out the existing, and it takes a full magnetic cycle, 22 years before the polarity at the poles is of equal polarity (Solanki, 2003).

Chapter 2

Computational methods

A detailed description for simulating the emergence and the physical properties of the sunspots is presented in this chapter. There are many properties to take into account when studying the new sources of flux. The simulation is based on the procedure described by Mackay et al. (2004).

2.1 How to simulate the emergence of new sources (BMR)

a Find the coordinates of the leading spot.

b Find the coordinates of the following spot, i.e calculate the tilt angle (the distance separation between the center of the leading and the following spots).

c Determine the hemisphere of emergence.

d Find the width of the spots, both spots will have the same width.

e Calculate the magnetic strength of the spots, both spots will have the same strength.

g Find the rate of emergence, i.e the number of events per time unit.

a. Find the coordinates of the leading spot.

The first latitude to be found in this simulation, is the one of the leading spot. The mean latitude of emergence, λ is decreasing linearly from 30-35 degrees, at the beginning of a cycle, to 5 degrees at the end of the cycle (Hathaway, 2010). We start by defining a latitude between 5 and 25 degrees, depending on the stage in the solar cycle, that can be later on, be either situated in the northern or in the southern hemisphere. At this stage, we only work on one hemisphere and are consequently only interested in a positive value. We consider a normal distribution with a time dependent mean and standard deviation:

$$\mu(t) = \lambda_{max} - (\lambda_{max} - \lambda_{min})\frac{\mathrm{t}}{\mathrm{T}} \tag{2.1}$$

$$\sigma_E(t) = \sigma_{Emax} - (\sigma_{Emax} - \sigma_{Emin})\frac{\mathrm{t}}{\mathrm{T}} \tag{2.2}$$

where T is the time length of a cycle and t is the time of emergence. Because this distribution determinates the mean latitude of the spot closest to the equator, λ_{max} is sat to be 25 degrees with a standard deviation of 7 degrees and λ_{min} to 5 degrees with a standard deviation of 2 degrees, see figure2.1. This allows the following spot to emerge at higher latitude within values in concordance with the observations. A threshold is set such that no leading spot can appear above $\lambda = 62.5$ degrees, furthermore, for numerical reasons, we decide to define a narrow region around the equator, where BMR can not emerge. This zone is between -0.57 and 0.57 degrees ($\pm 0.01 rad$) of latitude. Purposely, according to the calculations shown in the next step, the latitude limits of emergence for the following spot are between 3.6 and 75 degrees.

We wish to weight the low latitudes of emergence greater than the high latitudes as observations have shown that most of the sunspots emerge at low to middle latitudes. One way is to sample from the absolute value of the defined normal distribution, in order to map the eventual negative values, that mostly would appear when the mean is close to zero at solar minimum, into very small positive values, resulting in a increased probability of sampling low latitudes values at solar minimum. The mean latitude of the leading spot is sampled from the absolute value of the defined normal distribution that follows the properties of the butterfly diagram (See figure 4).

$$\lambda(\theta, t) \sim |\mathcal{N}(\mu(t), \sigma(t)^2)|$$

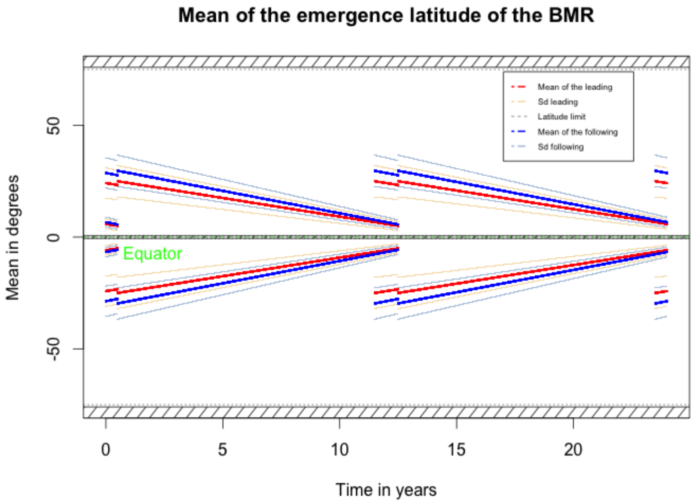

Figure 2.1: Mean latitude function in degrees

At the time of overlap, BMR can emerge at both high and low latitudes. Nevertheless, we have slightly lowered the mean of emergence at high latitudes during this period of overlap, for two reasons. The first is the wish to preserve the wanted mean values during the sunspot cycle period. The other is for not producing mean latitudes that would be higher than at the beginning of a cycle. The sunspot maximum is reached five years after the beginning of a new cycle. On figure 2.1 it corresponds to 5.5 years, and 18 years. The first cycle runs from 0.5 years to 11.5 years, while the second cycle runs from 12.5 years to 21.5 years. The times of overlap are between 0 and 0.5 years, 11.5 and 12.5 years, and the last one in this simulation starts at 21.5 years.

The longitude of the leading spot has to be found. We work with the assumption that the probability of emergence is equal all along the longitude of the Sun. It is therefore sampled from a uniform distribution between 1 and 360 degrees.

Figure 2.1 shows the mean latitude of emergence, and the corresponding standard deviation functions of the two spots forming a BMR. The dashed regions are free from spot emergence. The mean latitudes are corresponding to those of a 12 years cycle with a half year of overlap at the beginning and at the end of a cycle.

b. Find the coordinates of the following spot, i.e calculate the tilt angle (the distance separation between the center of the leading and the following spots)

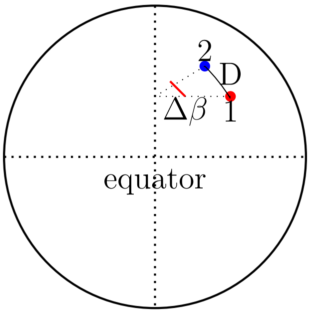

Figure 2.2: Angular separation

In step one, we have determinated the coordinates of the leading spot, and from relation 2.3, we can now calculate the coordinates of the following spot. According to previous work (Mackay et al., 2004), (Baumann, 2005), the tilt angle is a function of the coordinates of the spots, especially of the latitudes 2.3. In this work, the calculations are based on the angle of separation, β between the two centers of the spots, which is found (see figure 2.2) through the relation:

$$\beta = \cos^{-1}(\sin(\lambda_1)\sin(\lambda_2) + \cos(\lambda_1)\cos(\lambda_2)\cos(\phi_1 - \phi_2)) \tag{2.3}$$

The coordinates of the leading spot are sampled from a truncated normal distribution and from a uniform distribution, from which the coordinates of the follower are found with help of the separation angle in equation 2.3.

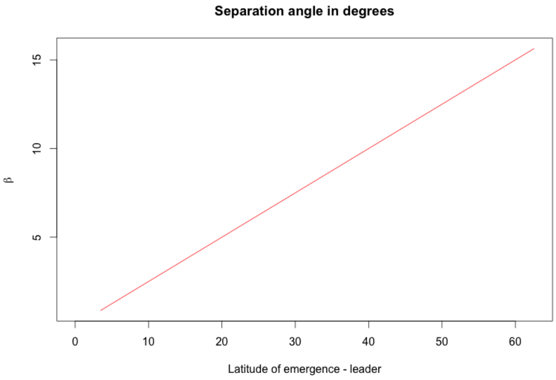

Figure 2.3: Separation angle - function of latitude λ_1

c. Hemisphere of emergence.

Once the coordinates of the BMR are found, we need to determine the hemisphere of emergence. The probability of emergence in one or the other hemisphere is equal:

$$\mathbb{P}(\lambda_{Em}i \in \text{Southern hemis.}) = \mathbb{P}(\lambda_{Em}i \in \text{Northern hemis.}) = 0.5$$

.

d. Width of the spots.

Observations show that the area of the BMR is proportional to the latitude of emergence and to the stage of the solar cycle (Hathaway, 2010). This can also be seen on figure 4 in the introduction page 5. The spots are very small at the beginning of a cycle and subsequently growing to large sizes at solar maximum and decreasing until solar minimum. The size of the spots are approximated by a truncated normal distribution with time dependent mean, with a standard deviation equal to the half of the mean width function. At solar minimum, the mean width is set to 1.15 degrees with a standard deviation of 0.575 degrees, while at solar maximum, the mean width becomes 4.3 degrees with a standard deviation of 2.15 degrees. The sampling from a normal distribution allows occasionally small and large spots to emerge at any time and any latitude, similarly to reality. However, while it is very rare that large spots emerge at solar minimum, the size of the spots experience large variations during solar maximum (see figure 2.4). As we will see in the next section 2.1, the strength of the spots is related to their width, which impose to set a threshold so the spots do not become too large nor too small. The distribution is truncated at a lower limit of 0.28 degrees and an upper limit at 9.4 degrees. For the same reasons as in section a. Find the coordinates of the leading spot, we wish to weight small widths greater than large widths, and will on this basis sample from the absolute value of a truncated normal distribution with time dependent mean.

$$\text{Width}(t) \sim |\mathcal{N}(\mu_{width}(t), (\frac{\mu_{width}}{2}(t))^2| \tag{2.4}$$

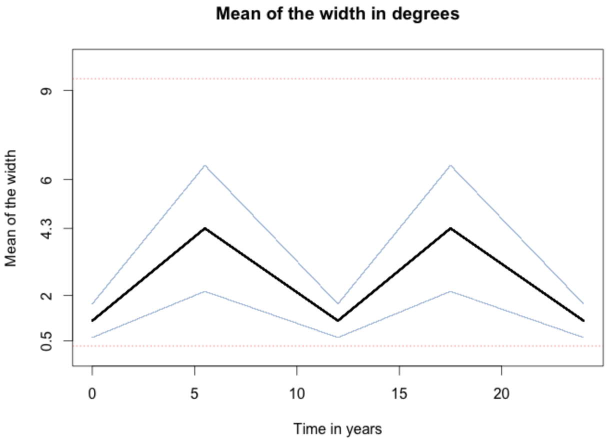

Figure 2.4: Mean of the width of the spots in a BMR in degrees

e. Magnetic strength of the spots

The strength of the spots is proportional to their widths; the larger, the higher becomes the strength. Analysis have shown that there is a linear relation between the tilt angle, the width and the stage of the cycle. We do not follow the precise relation described in the litterature (Jensen and Ringnes, 1957). van Ballegooijen et al. (1998) has described the flux repartition of a new BMR as a relation between the tilt angle, the width of the spots and an initial field strength, B_{max}. However, for small BMR, the repartition can be approximated by a Gaussian bell (Mackay et al., 2004). We therefore define the flux repartition of the BMR as two Gaussian bells, one of negative polarity and one of positive polarity. It has to be notice that the formulation of the initial value of the field in equation 2.5, does not integrate to zero as required in a FV method because of the conservation of the field. This will be adjusted in the FVS code in R.

$$\begin{aligned} G &= \frac{A}{2\pi \mathrm{Width}^2} \exp(-(\frac{(\lambda-\lambda_1)+(\phi-\phi_1)}{2\mathrm{Width}^2}) \\ &- \frac{A}{2\pi \mathrm{Width}^2} \exp(-(\frac{(\lambda-\lambda_2)+(\phi-\phi_2)}{2\mathrm{Width}^2}) \end{aligned} \tag{2.5}$$

where G is the strength of the BMR, A is a function of the width, of the form $A = C \exp(Width)$ with the Width in radians, and C is a suitable constant. The Width is between 0.28 and 9.4 degrees, which is a range between 0.005 and 0.164 radians. Making the strength proportional to the exponential of the width results in slow growing strengths for small widths, and fast growing strengths for large widths (see tables 2.1 and 2.2).

The flux repartition is a function of the width, and of the coordinates of the spots. By extension, it will be related to the time of emergence in the cycle. The range of the strengths, is in average, depending on the coordinates of the BMR, between ±90G to ±3200G, where these extreme values are very rare, nevertheless, they are in concordance with the values observed by Solanki (2003). Figure 2.5 illustrates the vertical repartition of the flux in the spots.

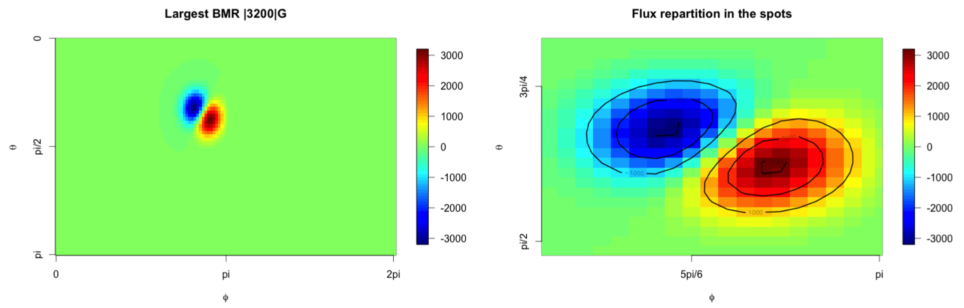

(a) Large BMR

(b) Field distribution in the spots

Figure 2.5: Flux repartition of very large BMR

The magnetic field in the spots, see figure 2.5(b), is faithful to the analysis performed by Solanki (2003).The field is ± 3200G at the center of the spots and falls to 1000G at the limit of the visible part of the spot area.

The most common strengths resulting from the values of the mean latitudes of emergence combined with the mean widths can be seen in tables 2.1 and 2.2.

At solar maximum					
	B_{max} (Gauss)	β (degrees)	width (degrees)	λ_1 (degrees)	λ_2 (degrees)
$\mu_{width} - sd$	180	4.5	2.1	18	21.6
μ_{width}	365	6.25	4.3	25	30
$\mu_{width} + sd$	760	8	6.4	32	38.4

Table 2.1: Mean values at solar maximum

At solar minimum					
	B_{max} (Gauss)	β (degrees)	width (degrees)	λ_1 (degrees)	λ_2 (degrees)
$\mu_{width} - sd$	100	0.75	0.57	3	3.6
μ_{width}	115	1.25	1.15	5	6
$\mu_{width} + sd$	130	1.75	1.71	7	8.4

Table 2.2: Mean values at solar minimum

In contrary to other work (Baumann, 2005), (Mackay et al., 2004), the width is not a function of the separation angle β. Nevertheless, they are both function of the latitude of emergence λ_1 and are therefore proportional when looking at the mean values. However, it can occur, that a BMR with a small separation angle can have a large width with a corresponding high strength.

f. Rate of emergence, i.e the number of events per time unit.

The time of solar cycle is approximated by a discrete time process with fixed time steps $\Delta t = t_{i+1}$ - t_i. The time of emergence of the BMR is approximated as a stochastic process in discrete time with time steps equal to the solar cycle time steps $\Delta t = t_{i+1}$ - t_i.

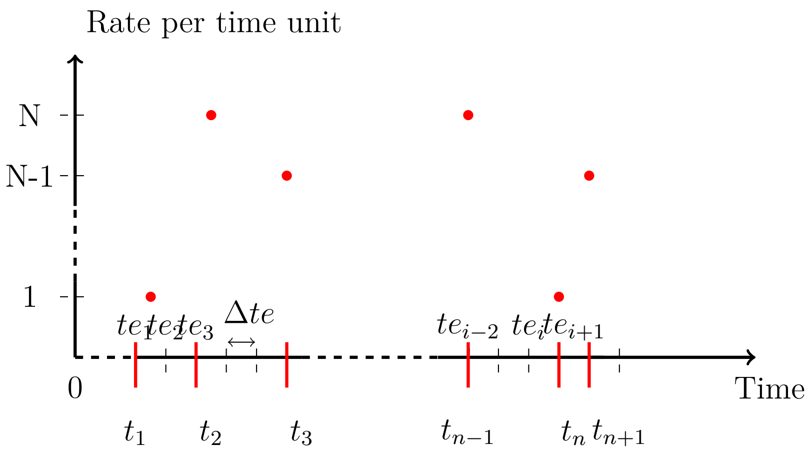

Figure 2.6: Arrival time

We consider a Poisson point process, where te_i is the arrival time, i.e the time of emergence of the i_{th} BMR, with a nonhomogeneous intensity $\lambda(t)$.

The expected number of events, Ne, in a time interval between t_i and t_{i+1} is given by:

$$\mathbb{E}\mathrm{Ne}(t_i, t_{i+1}] = \int_{t_i}^{t_{i+1}} \lambda(t)dt \tag{2.6}$$

We have:

- Ne(0) =0
- The increments are independent : for $t_1 < t_2, ..., t_{i-1} < t_i < t_{i+1}$, the number of events $\mathrm{Ne}(t_2, t_1], ..., \mathrm{Ne}(t_{i-1}, t_i], \mathrm{Ne}(t_i, t_{i+1}]$ are independent.
- The increments are stationary, the distribution of the number of events that occur between t_i and t_{i+1} depends only on the length of the interval: for $t_i < t_{i+1}$, the distribution of Ne (t_{i+1}) - Ne (t_i) equals the distribution of Ne $(t_{i+1} - t_i)$

The number of events Ne, between a time interval t_i and t_{i+1} is Poisson distributed with the intensity function $\lambda(t)$. $\lambda(t)$ increases linearly from a rate of 0.1 BMR per day at a solar minimum to 1.9 BMR per day at the solar maximum and falls back to 0.1 BMR per day at the end of a cycle as seen on figure 2.7.

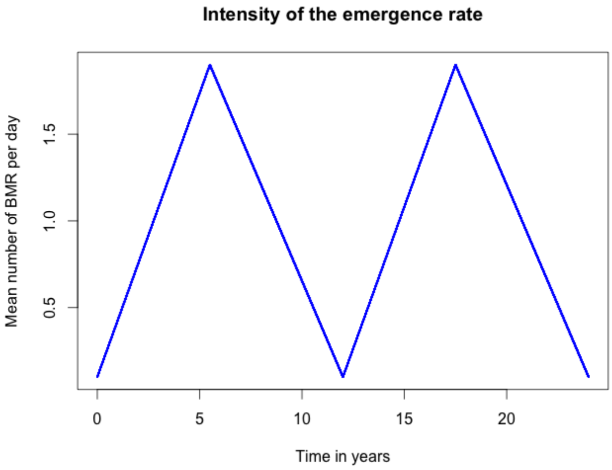

Figure 2.7: Intensity of the Poisson process

As illustrated in figure 2.6, there are not events at every time steps. The lower the intensity, the more time steps free of events, which is exactly what we were seeking. As an example, during a solar minimum, this process can produce two events at a time between t_{i-1} and t_i and none between t_i and t_{i+20} corresponding to a rate of 0.1 per time interval.

Chapter 3

Verification of the sources model

3.1 Background

As mentioned previously, the input parameters for the model are chosen based on observations and previous analysis of the solar surface (see the real data in the next part). In this work, we are mostly interested in the solar cycles 23 and 24, ranging from 2003 to 2014, from which we have taken average values. We will use a 12 years cycle with half a year of overlap at both ends of the cycles. Other studies have used one year of overlap at both end of the cycle, and consequently a cycle running time of 13 years. For minimising the running time of the simulation, we have chosen to use a 12 years cycle running time. Another feature that we have taken into account, is the difference of time between a solar minimum and maximum and between a maximum and a minimum. During a cycle, the rising time from a solar minimum to a maximum is shorter than the time of decay (Hathaway, 2010). Other studies (Baumann, 2005), (Mackay et al., 2004) ususally place the maximum at the precise half cycle time. Because our goal is to analyse the light curve produced from this simulation, and compare it to real data, we will set the solar maximum to five years after the beginning of the cycle and the decay time to a minimum to six years.

3.2 Simulation of two solar cycles

We now want to run a simulation of two full cycles. van Ballegooijen et al. (1998) have defined an initial surface magnetic field as a function of the latitude so it corresponds to the quiet Sun, i.e a solar minimum where there are few spots. At that stage of the cycle, the field can be approximated by a steady state configuration, where the meridional flow balances the supergranular diffusion. We have chosen to start our two cycles simulation with an initial field corresponding to a solar minimum reached after a whole cycle has been running,see figure 4.24. The time unit is chosen to be the same as for the real data, that we will work with in the next part, which is 6 hours per day. One cycle has a length of 12 years with a cycle period of 11 years.

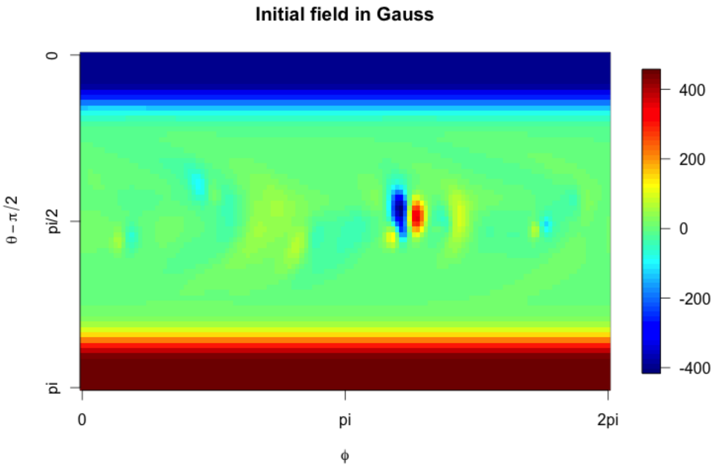

Figure 3.1: Initial B field in Gauss

Figure 3.1 corresponds to a solar minimum, with a maximum filed of $\pm 450G$. There is one spot that have emerged at the end of a cycle, very near the equator, at $\frac{\pi}{2}$.

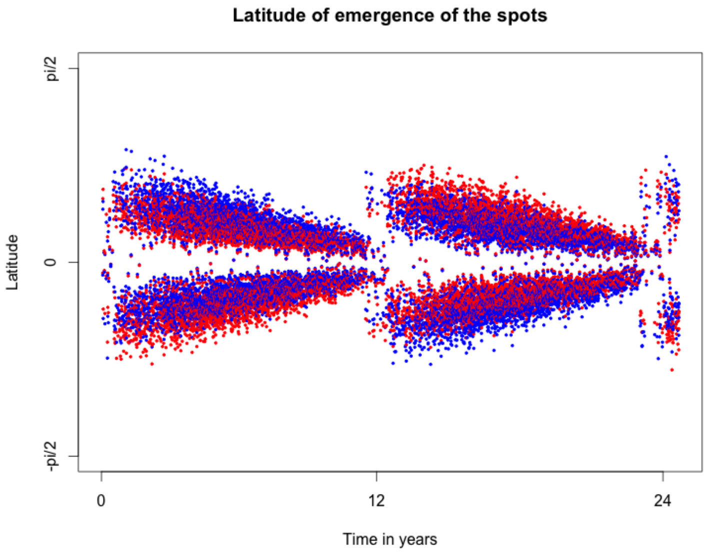

Figure 3.2: BMR latitude of emergence

The latitude of emergence of the BMR follow the butterfly diagram as defined on figure 2.1. We can denote some deviations from the mean, which is the effect that we wanted to produce by sampling from a truncated normal distribution. During the first cycle, from 0.5 to 11.5 years, the leading spot in the Northern hemisphere is colored in red and the follower in blue. It is the opposite at the Southern hemisphere. The colors are inversed at the next cycle beginning at 12.5 years.

The polarity at the poles is changing during each cycle around the solar maximum, as it should do (Mackay and Yeates, 2012). In other studies, (Mackay and Yeates, 2012), the polarity reversal happens between one and two years after the simulated solar maximum. In the present work, this polarity switch can happen from one year before a maximum up to two years after, which corresponds better to reality. This reflects the pertinent choice of parameter values for the model. Figure 3.3 shows the field one year after the solar maximum. Figure 3.4 show the field 1.5 year after the second solar maximum in our simulation.

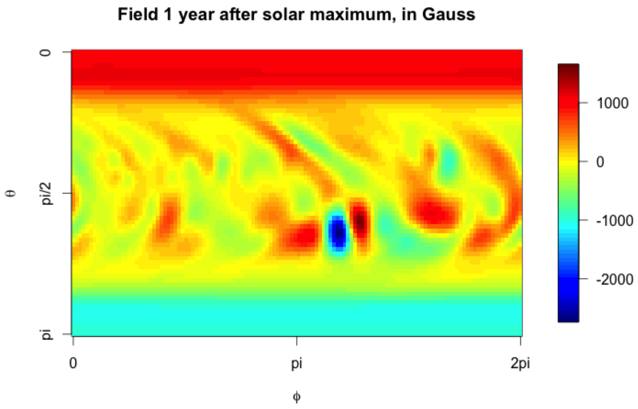

Figure 3.3: The field 6 years after the beginning of the cycle

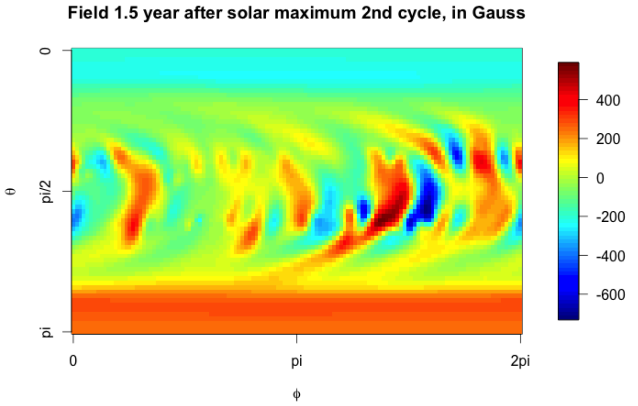

Figure 3.4: The field 6.5 years after the beginning of the cycle

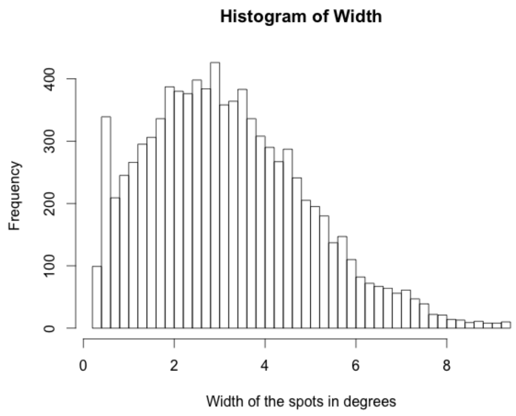

Figure 3.5: Frequency of the width of the spots

The truncation of the normal distribution for the calculation of the size of the spots allows the desired frequency of the different sizes. Figure 3.5 shows that there is a concentration of small spots with a width between 0.5 and 1 degree. The mean of the width during two solar cycles is 3.18 degrees.

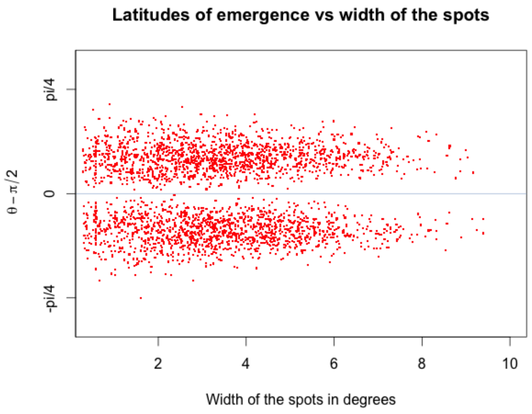

Figure 3.6: Width of the spots at different latitudes of emergence

Figure 3.6 illustrates that the latitude of emergence and the width of the spots are not a function of each other, but time dependent. We can see that during the solar maximum, at mid latitudes, the spots can have widths that vary between 0.28 degrees up to the maximum allowed size in this simulation, 9.4 degrees. Middle to large size spots, up to 6 degrees, can emerge at low and high latitudes, corresponding to a solar minimum, where the mean width was set to 1.15 degrees.

The number of BMR during this simulation can be seen in table 3.1. As we will see in part III, these values are in concordance with real values.

Number of BMR	
Cycle 1 (between year 0.5 to 11.5)	4207
Cycle 2 (between year 12.5 to 23.5)	4377
Cycle average (11 year's cycle)	4292
Overlap 1 (between year 0 and 0.5)	39
Overlap 2 (between year 11.5 and 12.5)	66
Overlap 3 (between year 23.5 and 24.5)	75
Overlap average (1 year's overlap)	60

Table 3.1: Mean numbers of BMR

3.3 Conclusion

We have defined a stochastic model for simulating the emergence of the BMR at time t, $S(\theta, \phi, t)$ that we have added to the homogeneous flux transport code from Part I. The choice of the parameter values in addition to the approximations by truncated normal distributions for the latitude of emergence, the width of spots and the rate of emergence, permit some deviations compared to fixed parameter values and seem to reproduce quite well real data. The results compared to other studies are quite similar and the model has been validated. We will now use simulations from this model to produce light curves.

Chapter 4

Light curve conversion

New sources in the form of BMR can now be added to the solar surface as a Poisson point process in time. The magnetic field will now be mapped into a light curve. There are different parameters to take into account when the conversion takes place. The Total Solar Irradiance (TSI), i.e the amount of light perceived at the upper atmosphere on Earth per unit area, usually measured in W/m^2 is a sum of the irradiance emitted from the different structures at the solar surface. As an example, we will perform two tests with a BMR of magnetic strength of 1000G at emergence and make it evolve for 60 days. The first will be placed at very low latitude, near the equator, while in the second test, it will be at high latitude. It is important to underline that these scenarios,i.e with equatorial and polar spots having a strength of 1000G, are very rare because of the definition of the input parameters from our BMR emergence simulation (see chapter two and chapter three in this part). The TSI will then be the sum of the corrections made for magnetic structures such as the sunspots, and the faculae but also from the geometry that influence the perceived light, the limb darkening. We assume that spots and faculae are the only structure contributing to the TSI. The time unit for the simulation will be one day. In order to see the global effect of these corrections, we will look at the light curve produced with the simulation used for the model verification in the previous chapter for a two cycles period, with a time unit of 6 hours, sampling time corresponding to the VIRGO data (See next part).

4.1 From magnetic field to light curve

The repartition of the large-structure of the magnetic field at the solar surface at time t reflects the effect of the three processes operating at the solar surface, i.e. the meridional flow, the differential rotation and the supergranular diffusion. All these transport processes can be traced in a light curve. We will look at the evolution over 2 rotations, that we choose to be 28 days for the BMR at high latitudes and 25 days for the BMR near the equator because of the differential rotation, with a sampling time of 1 day, of a BMR with a strength of 1000G. The coordinates of the bipole near the equator are in degrees ($\lambda_1 = 5, \phi_1 = 70$) for the leading spot and ($\lambda_2 = 6.9, \phi_2 = 62$) for the following, while the coordinates of the bipole at high latitudes are ($\lambda_1 = 45, \phi_1 = 70$) for the leading spot and ($\lambda_2 = 55, \phi_2 = 61$) for the follower. All the plots have a region shaded in grey corresponding to the non visible half surface of the Sun, assuming a fixed observation point.

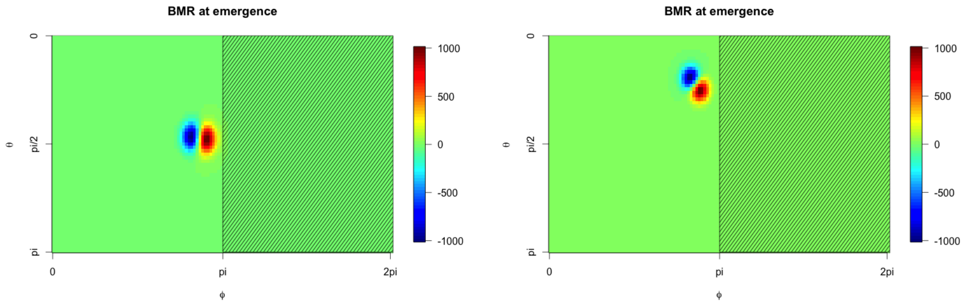

(a) BMR low latitude

(b) BMR high latitude

Figure 4.1: BMR 1000Gauss at emergence

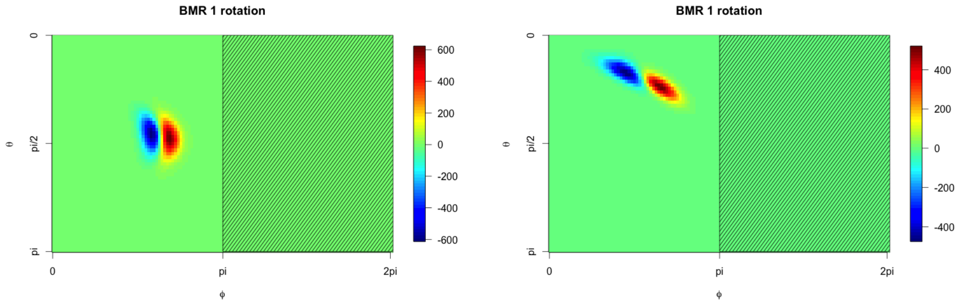

(a) BMR low latitude

(b) BMR high latitude

Figure 4.2: BMR after 1 rotation

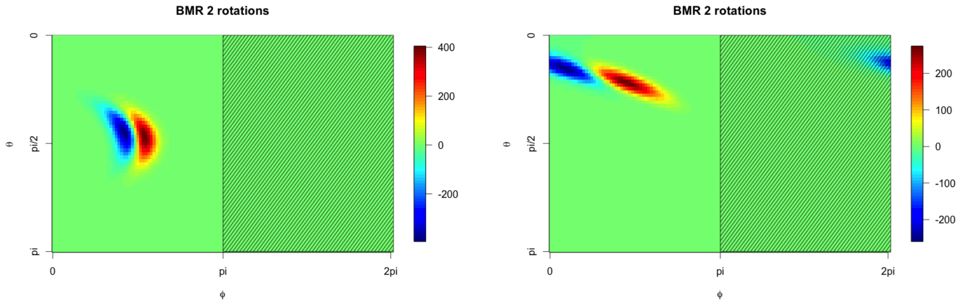

(a) BMR low latitude

(b) BMR high latitude

Figure 4.3: BMR after 2 rotations

As we can see on figures 4.3(b) and 4.3(a) it is very clear that low latitudes rotate faster than at high latitudes. From these fgures, it is noticeable that there is a clear difference in the dominant transport process depending on the latitudes. Near the equator, the spots are only driven by the differential rotation, whereas at high latitudes, the meridional flow takes over, as we have seen in the model validation chapter, in Part I. We can see the evolution of the field on the visible part of the sphere, before any optical corrections. The strength at emergence is 1000G, after one rotation the field is fallen to 600G for the equatorial BMR and to 500G for the polar BMR. After 2 rotations, the field strength has decreased to 400G for the equatorial spots and 300G for the polar ones. We will now proceed to the corrections due to the limb darkening, the luminosity at the spots and the brightness of the faculae, i.e bright spots, that are associated to the sunspots.

4.1.1 The limb darkening on the non magnetic Sun

The limb darkening is an optical effect from the observation point, that makes the center of the observed disk appear brighter than at the edges, called the limb. This is an effect resulting mainly from a difference in temperature between the center of the observed disk and the limb, where the temperature decreases proportional to the distance to the center. The solar irradiance is measured from the surface of the Earth, at 1 A.U, from where the Sun clearly does not appear equally bright on all points of its visible surface. Figures 4.4 and 4.5 show the geometry of the limb darkening on the sphere from the observation point. The limb darkening is a function of the heliocentric angle ψ ,which is the angle between the line of sight and the normal to the sphere at the point of sight, P (See figure 4.4 and and 4.5), from the center of the Sun. The limb darkening, μ, is defined as the cosine of the heliocentric angle, ψ and can be seen on figure 4.6. Figures 4.4 and 4.5 show a sketch of the limb darkenig geometry, where the lines of sight represent the lines from Earth to the Sun. They might be more parallele than on the figures in reality, as the distance between the Sun and the Earth is 1 A.U.

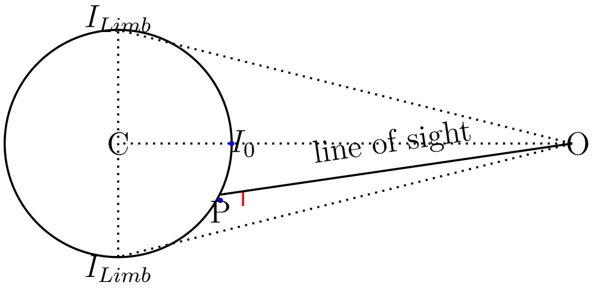

Figure 4.4: Limb darkening geometry

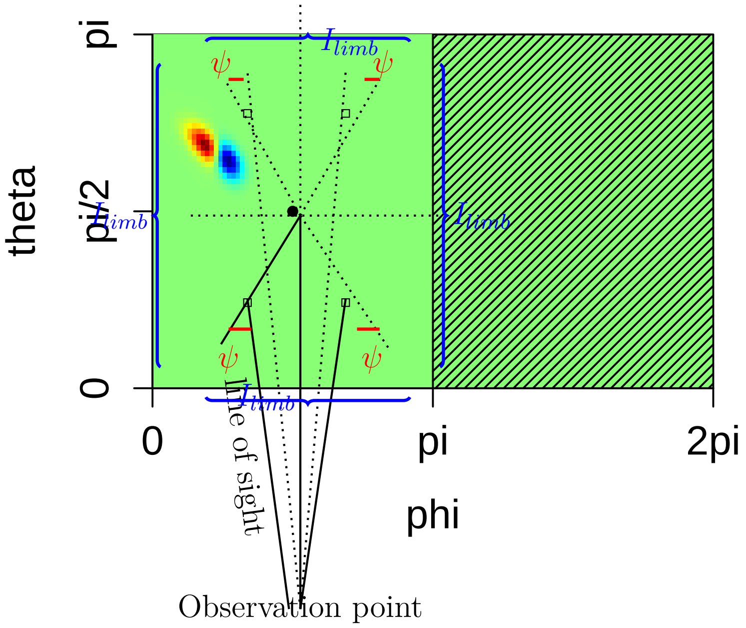

Figure 4.5: Limb darkening geometry on the projected map

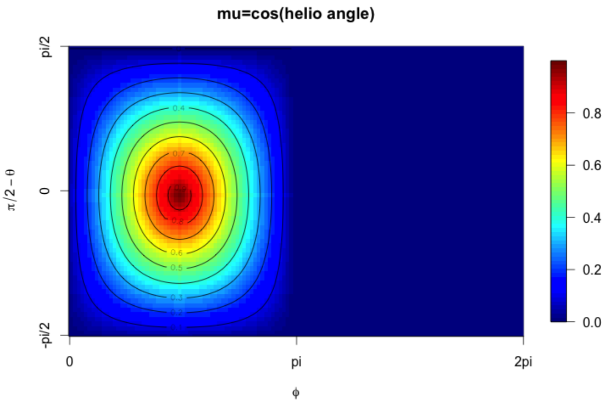

Figure 4.6: Limb darkening, $\mu = \cos(\psi)$ -
Notice the color scale, the dark red is brightest.

The quadratic form of the limb darkening (Leonard and Choudhary, 2008) is given by the following equation and can be seen on figure 4.7.

$$I_{LD}(\mu) = 0.329 + (0.908\mu) - 0.240(\mu^2) \tag{4.1}$$

This corresponds to the intensity of the emitted light from a non magnetic Sun, i.e the Sun when there are no or very few spots.

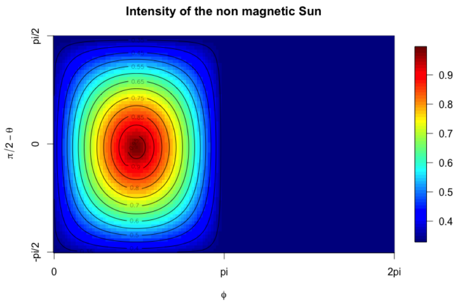

Figure 4.7: The intensity of the non magnetic Sun
Notice the color scale, the dark red is brightest.

Figure 4.6 shows that the intensity of the emitted light decreases fastest between the center of the visible disk where $\mu = 1$ and $\mu = 0.6$. Between $\mu = 0.6$ and the limb $\mu = 0$, the intensity still decreases but at a lower rate, a feature that also can be seen on figure 4.6.

4.1.2 Intensity at the spots

One of the physical characteristics of the sunspots is that they appear darker than the surrounding material, because of their lower temperature. The light emitted at the spots is consequently lower at these area. The intensity at the spots is a function of the magnetic field $|B|$ (Leonard and Choudhary, 2008) , where the normalised contribution is defined as:

$$I_{spot}(B) = 0.96035 - 0.0004174|B| + 10^{-7}1.13514|B|^2 \tag{4.2}$$

This relation is valid for a magnetic field of $\pm 1500G$. The field is set to saturate at these values. Figure 4.8 illustrates how the intensity increases as the strength of the magnetic field in the spot decreases. It is without doubt that the interior of the spots is less bright than the surrounding, because of their dark apparance. This property can easily be seen on figures 4.9 and 4.10 and 4.11. After two rotations, the field has fallen down to 400 G for the equatorial BMR and 300G for the polar BMR, and the difference of intensity at the spots and the surrounding becomes to balance each other (see figure 4.11).

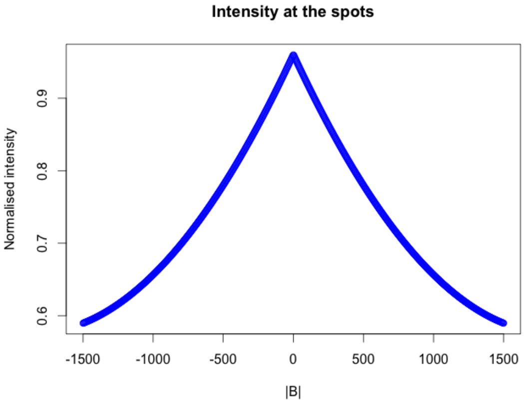

Figure 4.8: Intensity of the spot as a function of |B|

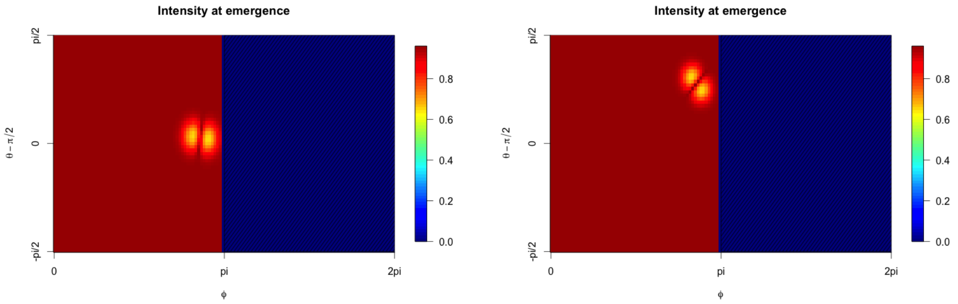

(a) BMR low latitude

(b) BMR high latitude

Figure 4.9: Spot intensity at the emergence
Notice the color scale, the dark red is brightest.

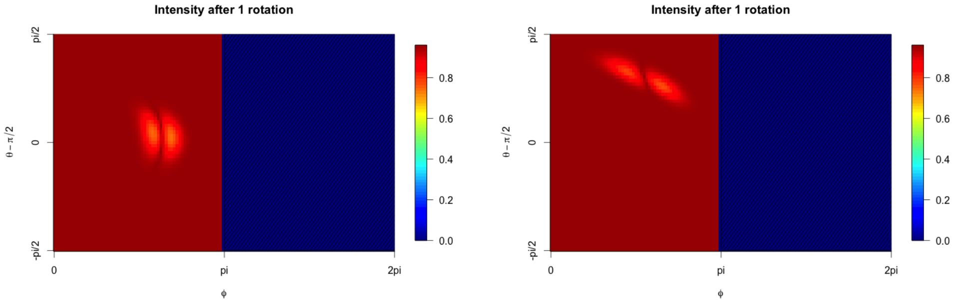

(a) BMR low latitude

(b) BMR high latitude

Figure 4.10: Spot intensity after 1 rotation
Notice the color scale, the dark red is brightest.

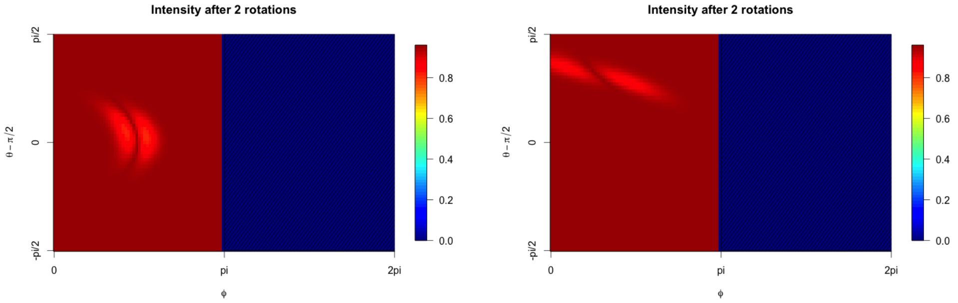

(a) BMR low latitude

(b) BMR high latitude

Figure 4.11: Spot intensity after 2 rotations
Notice the color scale, the dark red is brightest.

For calculating the contribution of the intensity at the spots, to the light curve, we need to correct I_{spot} by its projection on the sphere, μ and by the limb darkening I_{LD}: $I_{spot.cor} = I_{spot} I_{LD} \mu$.

The primary factors for the change in the spot intensity are the strength of the magnetic field at the spots and their latitudes. These characteristics are illustrated in figures 4.12 and 4.13 At the emergence it is difficult to distinguish the two spots next to the limb at π. After one rotation, the field has begun its dispersal and covers a larger area: after two rotations, the area of field is even larger. Figures 4.13 and 4.14 show the difference and the importance of the location on the sphere for the irradiance of the Sun. In effect, it is clear that the spots at low latitudes have an increasing luminosity as the field dissipates and their area grows, while at high latitudes, it is difficult to denote any differences between the time of emergence and after two rotations. However, it is possible to slightly perceive the spots passing around the sphere.

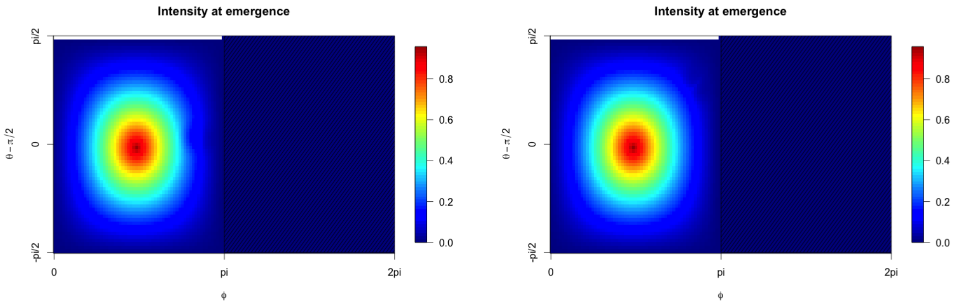

(a) BMR low latitude

(b) BMR high latitude

Figure 4.12: Spot intensity at the emergence
Notice the color scale, the dark red is brightest.

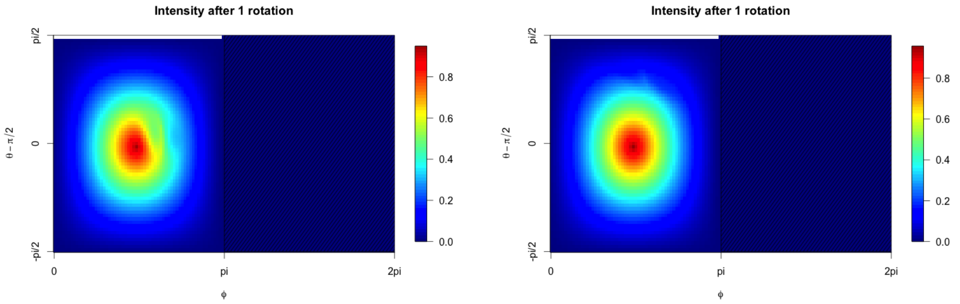

(a) BMR low latitude (b) BMR high latitude

Figure 4.13: Spot intensity after 1 rotation
Notice the color scale, the dark red is brightest.

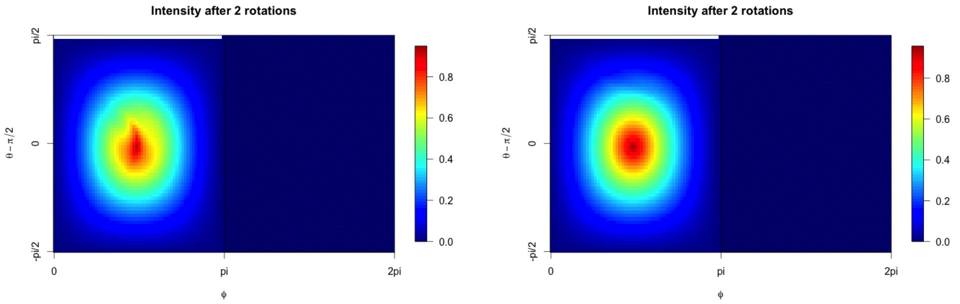

(a) BMR low latitude (b) BMR high latitude

Figure 4.14: Spot intensity after 2 rotations
Notice the color scale, the dark red is brightest.

We can now calculate the contribution to the light curve. This is just the surface integral of the corrected intensity over the visible surface.

$$TSI_{I_{spot}} = \int_0^\pi \int_{-1}^1 I_{spot} I_{LD} \mu d\cos(\theta) d\phi \tag{4.3}$$

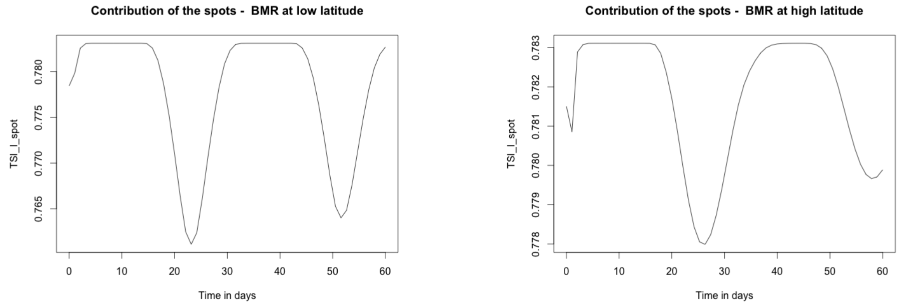

(a) BMR low latitude (b) BMR high latitude

Figure 4.15: Contribution of the intensity at the spots

Figure 4.15 show clearly that the irradiance at the spots is lowest in the visible part. We can clearly see how peaks increase as the field strength falls. The difference in the rotation time is very apparant as well. It is clear that it takes longer time to rotate at high latitudes, the peaks in the irradiance curve for the polar spots are shifted compared to the peaks for the equatorial spots.

4.1.3 The contrast at the faculae

The faculae or bright spots, are only detectable around the sunspots, although they are covering the whole surface of the Sun. Their emergence follows the sunspot cycle, and are one of the reason why the Sun appears brighter at solar maximum, despite of the dark effect of the Sunspots. The contrast of the faculae is defined as a function of the magnetic field B and μ (Ortiz et al., 2002) and (Yeo et al., 2013). Its normalised relation is given by:

$$\begin{aligned} I_{Contrast} &= 10^{-4}(0.48+9.12\mu-8.50\mu^2)|B| \\ &+ 10^{-6}(0.06-2.00\mu+1.23\mu^2)|B|^2+10^{-10}(0.63+3.90\mu+2.82\mu^2)|B|^3 \end{aligned} \tag{4.4}$$

This equation is valid for a magnetic field range $0to \pm 600G$. Field that would be greater than this threshold will be considered as being equal to $\pm 600G$.

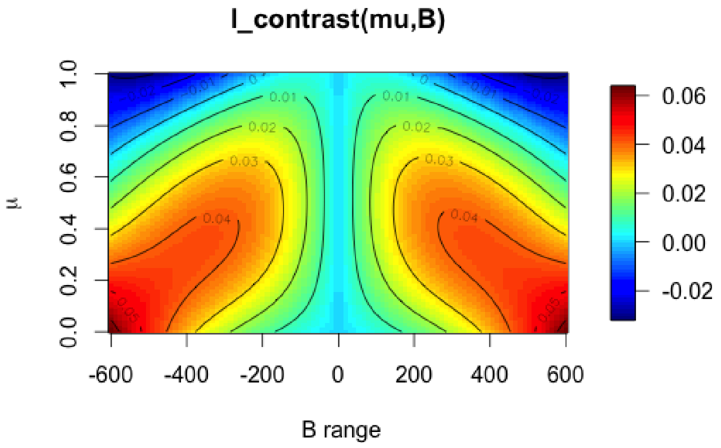

Figure 4.16: Contrast at the faculae as a function of |B|
Notice the color scale, the dark red is brightest.

Figure 4.16 shows how the contrast at the faculae varies in function of the magnetic field value B and the cosine of the heliocentric angle, μ.

When the field is strongest, at $\pm 600G$, and at the center of the visible disk, the contrast factor becomes sligtly negative. For a high B value, the contrast is highest at the limb. For a moderate magnetic field value, between 200G and 400G, we will expect a strong contrast for $\mu = 0.4$.

The following images represent the intensity of the contrast projected on the sphere, $I_{Contrast.corr}(B,\mu) = I_{Contrast}(B,\mu) I_{LD} \mu$. To favorise visibility, the intensity is very low, we are not using the same color scale as the one used for the irradiance at the spots.

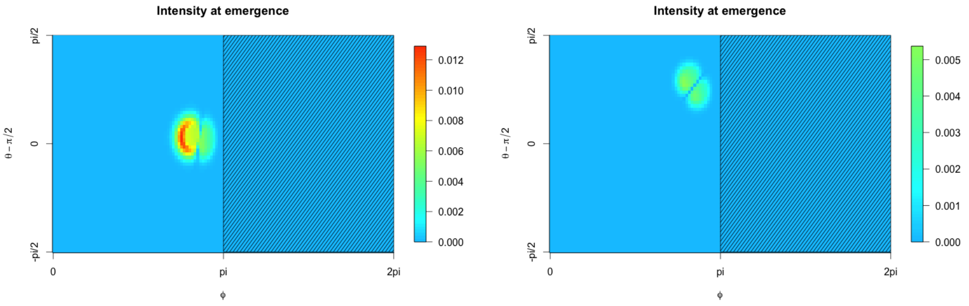

(a) BMR low latitude (b) BMR high latitude

Figure 4.17: Contrast intensity at emergence
Notice the color scale, the dark red is brightest.

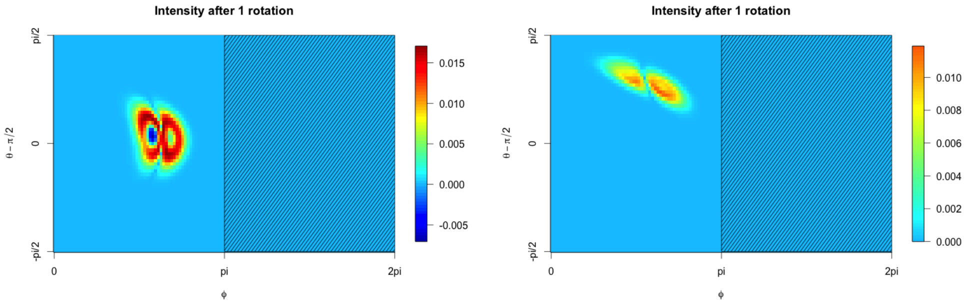

(a) BMR low latitude

(b) BMR high latitude

Figure 4.18: Contrast intensity after 1 rotation
Notice the color scale, the dark red is brightest.

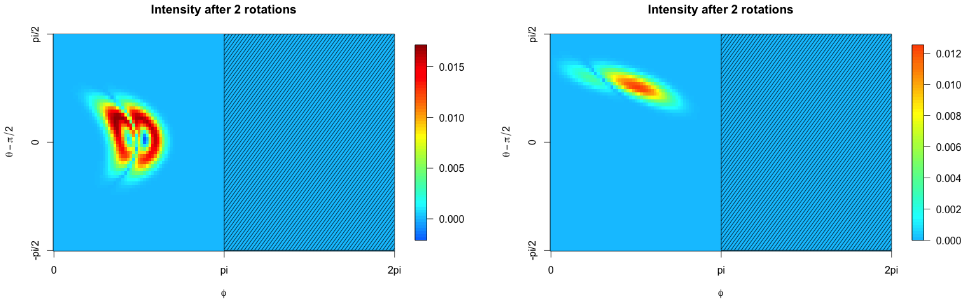

(a) BMR low latitude

(b) BMR high latitude

Figure 4.19: Contrast intensity after 2 rotations
Notice the color scale, the dark red is brightest.

The contrast at the faculae is clearly highest for BMR at low latitudes, which is a consequence of the nature of the limb darkening that is highest at the center of the visible part. At the emergence, the BMR are near the limb and the contrast is therefore not so high as when closer to the center. We begin with the contrast of the faculae for the equatorial BMR. After one rotation, where the maximum field strength is $\pm 600G$ (see figure 4.2(a)), we experience a negative contrast that can be seen on figure 4.18(a). The center of one of the spots, where the field strength is highest, is positioned at the center of the visible part, where the value of the limb darkening, μ, is equal to one. This combination of field strength and position on the sphere corresponds to a position in the upper left corner on figure 4.16 where the contrast is negative, with a value of -0.005. The surrounding has a positive contrast with values that are similar to those at emergence. After two rotations, the BMR have the same central position, see figure 4.19(a), and the contrast at the center is still negative, with a lower negative value of 0.02, because the magnetic field strength has decreased to $\pm 400G$ (see figure 4.3(a)), which is what expected from figure 4.16.

The faculae contrast for the polar BMR on the other hand, does not experience such large variations (see figures 4.18(b) and 4.19(b)) and is mostly influenced by the position of the spots more than the field strength. The latitude position of the BMR corresponds approximatively to a μ value of 0.6 from the time of emergence until two rotations. A position where the contrast does not vary much and is between 0.01 and 0.02 all along the visible part, as we can see on figure 4.16.

The contribution to the light curve of the light intensity at the faculae is here again the surface integral of the corrected intensity over the visible surface.

$$TSI_{I_{contrast}} = \int_0^\pi \int_{-1}^1 I_{contrast} I_{LD} \mu d\cos(\theta) d\phi \tag{4.5}$$

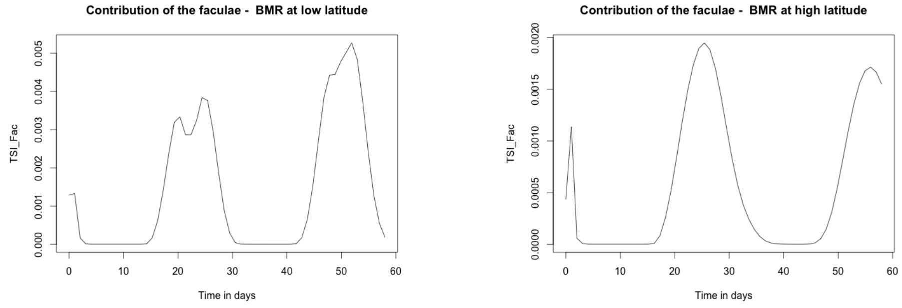

(a) BMR low latitude

(b) BMR high latitude

Figure 4.20: Contribution of the irradiance of the faculae

The latitude of the BMR is clearly an important factor for the resulting light curve contribution from the faculae contrast. The negative contrast appears as a decrease in the intensity when the BMR is at the center of the visible part (see figure 4.20(a)). This is the reason why the intensity value increases from the peaks at one rotation to the peaks at two rotations, as the contrast becomes less negative, the intensity finds a more regular shape when in the visible part of the sphere. The intensity coming from the BMR at high latitudes, on the other hand is more smooth and decreases from the values at one rotation to those at two rotations, as the field dissipates.

4.2 Simulated Total Solar Irradiance

We have now seen the effect of the corrections of the intensity of the sunspots and at the faculae. The simulated light curve is a sum of integrals 4.3 and 4.5. However, studies have shown that the area covered by faculae is 10 times the area covered by sunspots, where the irradiance of the sunspots should only contribute to less than 0.01%(Yeo et al., 2013). This means, that the contrast at the faculae should cover a broader range of values than when using the same area as the sunspots. However, in this work, we have defined the area of the faculae to be equal to the sunspots, and have corrected the contrast from that area. We therefore have to assume that the lacking broader faculae area and consequently a broader range of contrast values for each faculae can be balanced by a larger irradiance contribution of each faculae, at every latitudes. On this basis, we will weight the irradiance from the sunspots as 1% contribution and the irradiance from the faculae as 99 % contribution to the light curve.

The TSI is calculated as :

$$\begin{aligned} TSI_{Total} &= 0.01\int_0^{\pi}\int_{-1}^{1} I_{spot} I_{LD} \mu d\cos(\theta) d\phi \\ &+ 0.99\int_0^{\pi}\int_{-1}^{1} I_{contrast} I_{LD} \mu d\cos(\theta) d\phi \end{aligned} \tag{4.6}$$

We have have run the simulation of the test BMR until the field has dissipated until approximatively $\pm 40G$ corresponding to 250 days, in order to see the evolution of the light curve over many rotations.

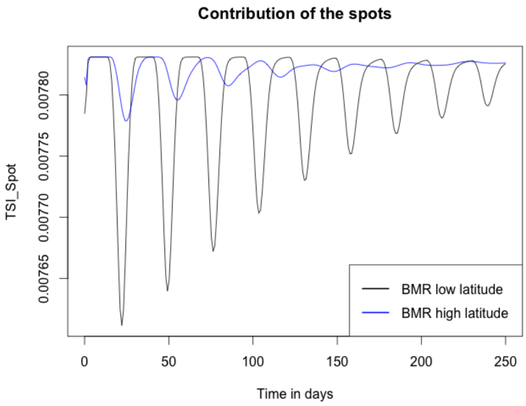

Figure 4.21: Contribution of the intensity of the spots

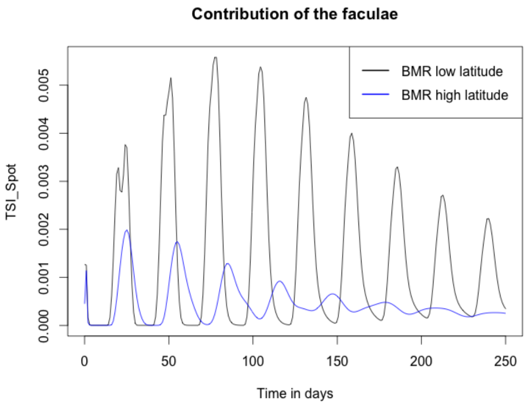

Figure 4.22: Contribution of the intensity of the faculae

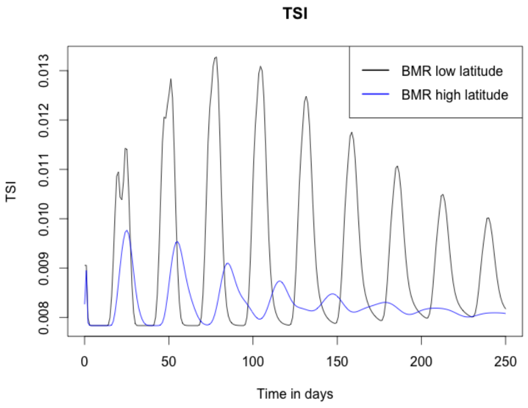

Figure 4.23: TSI of BMR - low and high latitudes

We recognize the patterns of the faculae irradiance plots (figure 4.23). It is important to specify again, that these configurations of BMR emerging at very high and very low latitudes would not have a maximum stength of |1000| G, because these latitudes of emergence correspond to solar minimum latitudes. As investigated in the previous chapter, sunspots are very small with a low strength (lower than |200| G) at solar minimum, resulting in contrasts that will not be negative, even in a configuration where the center of a sunspot would pass the center of the visible part (see figure 4.16). However, the parameters governing the strength of the BMR are sampled from a truncated normal distribution, with the purpose of having the possibility to experience scarecely large deviations from the mean and consequently negative contrasts. This is a way to compensate for the lacking 1:10 relation between sunspots area and faculae area.

4.3 Simulation of light curve over two solar cycles

It is now possible to simulate light curves from the data of the full flux transport code. We will now investigate the ligth curve produced from the two cycles simulation used in chapter three. The sampling time is six hours, corresponding the sampling time from the VIRGO data, that we will analyse in the next part. We have used a cycle time of 12 years, with half a year of overlap at both ends of the cycle, where BMR can emerge at both low and high latitudes until the beginning of a new cycle (Mackay et al., 2004). The resulting cycle period, defined as the time from where the first BMR in a given hemisphere have swiched polarity compared to the previous cycle, until a new overlapping time beginns, becomes 11 years.

The intial field corresponds to the last time of a cycle.

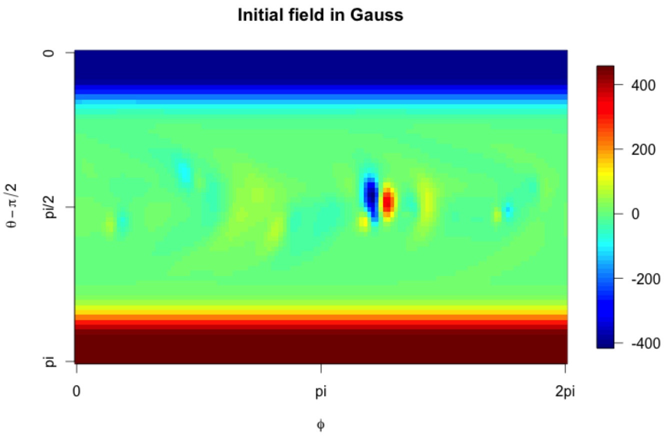

Figure 4.24: Initial B field

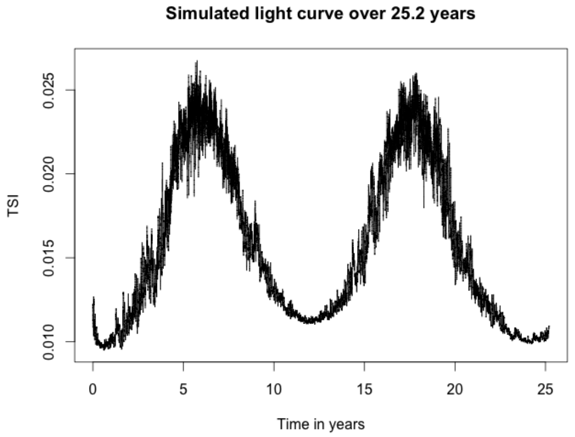

Figure 4.25: Light curve from simulated cycles

Figure 4.25 shows that there are large variations in the size of the BMR at different times of the simulated cycles. During the first cycle, these variations occur on the way up to a solar maximum, while during the second cycle, the largest variations are on the way down from the solar maximum. This explains why the reversal of the polarity at the poles occur at different time in each cycle as we have seen in the previous chapter, although it has to take place between one and two years after a solar maximum, which it does (Mackay and Yeates, 2012).The solar maximum happens around 5.5 years for the first cycle and 17.5 years for the second cycle.

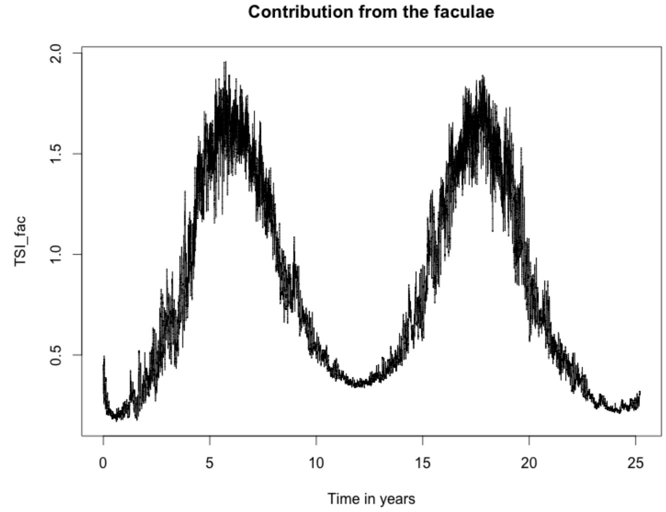

Figure 4.26: Contribution from the faculae

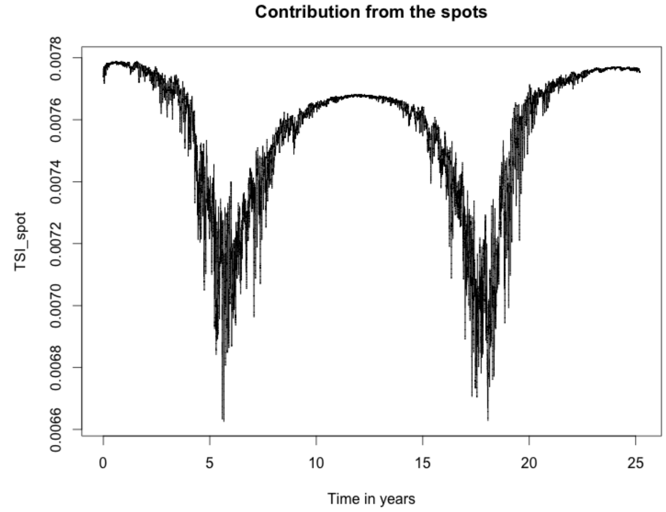

Figure 4.27: Contribution from the sunspots

It is clear that the irradiance of the spots has an opposite pattern than the irradiance of the faculae. At solar maximum, we can clearly see on figure 4.27 the difference in the size of the spots, where there are large variations in the light intensity at the spots.

Chapter 5

Summary and conclusion

The flux transport equation with the source term, $S(\theta, \phi, t)$ has been solved. The emergence of new sources of magnetic flux have been defined as a stochastic process and added to the homogeneous flux transport equation. The spatial properties, i.e the Hale's and Joy's law, known from observations have been presented. These laws are crucial for the dispersal of the magnetic flux on the solar surface. The Joy's law about the relative position of the two spots that forms a BMR, the tilt angle, is determinant for the correct poleward transport of flux. The Hale's law makes sure that the respectively leader and follower spot, keep the same polarity during a same cycle. The methods and parameter values for simulating the emergence of new sources have been calculated with help of results from previous work. We have chosen to sample the emergence latitude of the leading spot and the width of the spots from the absolute value of a truncated normal distribution, in order to allow occasional deviances from the mean values, but also for weighting small values highest. Their means have been defined as time dependant, following the solar cycle, where their maximum values are to be found at the simulated solar maximum, in the present work, 5 years after the beginning of a new cycle. The mean latitude of emergence of the leading spot, has a range starting at 25 degrees at the beginning of a cycle, with a standard deviation of 7 degrees, for ending at 5 degrees with a standard deviation of 2 degrees. The latitude of the follower is a function of the latitude of the leading spot and its mean ranges from 30 degrees with a standard deviation of 7 degrees down to 6 degrees with a standard deviation of 2 degrees. In this work, we have assumed that the longitude of emergence is equal all along the sphere, and is therefore sampled from a uniform distribution from 1 degree to 360 degrees for the leading spot. The longitude of the following spot is found through the separation angle between the two spots.The mean of the width has been set to 4.3 degrees at solar maximum and 1.15 degrees at solar minimum. The flux repartition of a spot has been approximated by a Gaussian bell with a standard deviation equal to the width of the spots and a mean equal to its coordinates. The strength of the BMR is a function of the coordinates and of the width of the spots, and can experience variations in the maximum value depending on where on the sphere, they emerge, for a given width. One BMR is defined as the sum of two Gaussian bells of opposite sign. These bipoles have the same maximum magnetic normed strength value, which balances each other.

A verification of the model has been performed by simulating two cycles of 12 years with half a year of overlap, giving a cycle period of 11 years. The butterfly diagram is well reproduced, with changing polarity at each hemisphere for each cycle. The mean of the widths is 3.18 degrees per simulated solar cycle. The simulation results in 4292 BMR per cycle in average, where the frequency of small sizes, and consequently low strengths, is highest.

In Chapter 4, we have worked on the conversion of the magnetic field into a light curve. We have performed light intensity corrections due to the limb darkening that makes the Sun appear non equally bright on its visible part, due to the dark appearance of the sunspots and due to the bright contrast of the faculae. In order to emphasise the contribution to the TSI of these intensities, we have worked through two parallel examples of BMR evolution during two cycles. With no surprise, the coordinates added to the strength of the magnetic field are determinant for the produced light intensity. The light intensity from the sunspots varies the opposite way as the intensity from the faculae. Litterature have shown that there exists a 1:10 relation between the area covered by the sunspots and the faculae. The contribution to the light curve, of the intensity of the spots should be less than 0.001 %. In the present work, we have not taken into account the 1:10 area relation and have used a faculae area equal to the spots area. In order to compensate for this missing correction, we have decided to weight the faculae contribution to the light curve with 99 % and the contribution of the spot intensity as 1 %. We have seen that the light intensity is most affected by a central position combined with a high field strength, causing negative faculae contrasts. Even though this is a very rare scenario, because at equatorial latitudes, the spots should have a very small width and a corresponding small strength, the probability of occurence is still there. This is a consequence of having defined time dependent means of latitudes and widths, and not having followed the direct width - tilt angle relation described by Joy's law. As a result, spots with large widths can emerge at any latitudes and might compensate to the lacking faculae area correction, by producing a larger range of faculae contrast at any latitudes. However, because of the input parameters, it is very rare to experience large deviations from the means, but important to include because of the large effect on the light curves.

The ligth curve resulting from a two solar cycles simulation will be the data used for the further analysis that we will work on in Part III.

Part III

Lightcurve parameter analysis

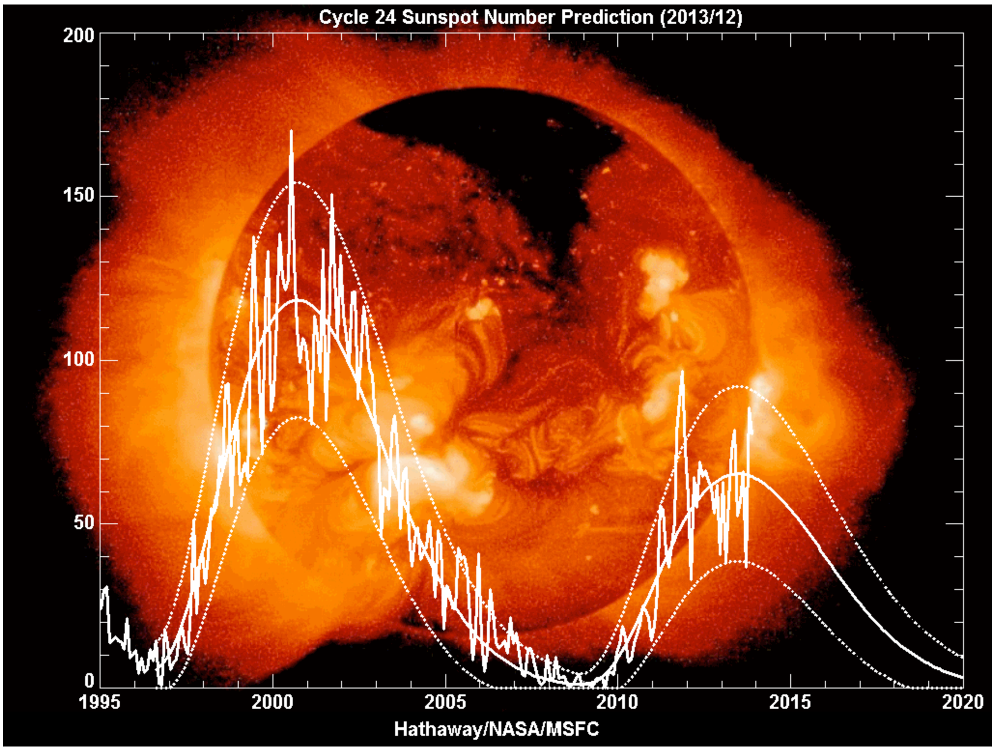

Source: http://solarscience.msfc.nasa.gov/images/ssn_predict_l.gif

Table of Contents

Chapter 1

Introduction

The flux transport PDE with the source term has been solved in the previous part. We are now able to convert the evolution of the magnetic field at solar surface into a light curve. In the previous chapter, we have run a two solar cycles simulation and converted it into a light curve. The aim of this part is to detect the causes of the variations in a light curve on a short timescale, such as six months. We want to compare the periods found in the real data to those from the simulated light curve. The data is represented as a set of unevenly spaced time series, it is therefore important to use appropriate methods that can handle missing data. We will try to model the data as a linear continuous time ARMA model, from which the spectrum can be found. It has been shown that such a model can present limitations and non linear modeling would certainly be more appropriate (Vio et al., 2005). We will not perform any nonlinear continuous time modelling in this work. Instead, we will perform light curve analysis with help of a commonly used technique when dealing with astrophysical data or other kind of data with missing values, the Lomb Scargle periodogram. We will look at the periods found from a sample of the VIRGO data, just before a solar maximum, where many parameters, e.g. the rate of emergence of the BMR or their latitudes of emergence, can influence the light curve produced. We will try to find the same periods in a sample of the simulated light curve around the solar maximum, by tuning different parameters which effect can be seen at different timescales such as the velocity of the meridional flow or the latitude of emergence of the BMR.

1.1 Description of the data

The data set is from the ESA/NASA SOHO spacecraft, VIRGO. Informations about the data can be found at the official VIRGO/SOHO homepage. It represents the Total Solar Irradiance measured at the terrestrial upper atmosphere, at 1A.U in W/m2. The TSI is *"the radiant energy emitted by the Sun at all wavelengths crossing a square meter each second outside the Earth s atmosphere"* (Jones, 1993).

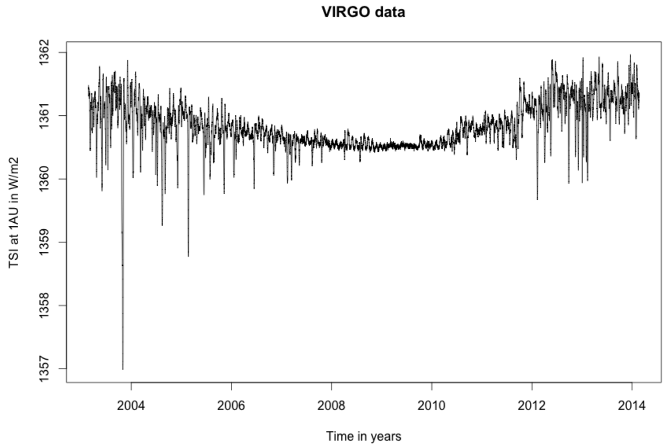

Figure 1.1: Virgo–lightcurve from February 25, 2003 to February 21, 2014

The data covers one period of 11 years with a sampling time of six hours, resulting in 16060 data points. The data runs from February 2003, solar cycle 23, to February 2014, solar cycle 24 and corresponds to a time two years after the last solar maximum until this year, 2014. Cycle 23 lasts for approximatively 12 years, and had its maximum in 2000- 2001. Cycle 24 began in January 2008 and is predicted to have its maximum during 2014 -2015 (NAS). On figure 1.2, we can see the averaged monthly sunspot number prediction, and recognise the pattern of the light curve from our data on figure 1.1. We can see that the averaged monthly number of sunspots per year differs a lot from one cycle to another. It has to be notice that the averaged monthly number of sunspots is not the same as the averaged monthly number of BMR as a BMR is formed by two sunspots. So the averaged monthly number of BMR would be 75 BMR per month at solar maximum during cycle 23, and 50 BMR per month at solar maximum during cycle 24, resulting in an average in the order of 2 BMR per day at maximum, which corresponds to the mean rate of emergence per day in our simulation. At solar minimum, we have used a mean rate of emergence of 0.1 BMR per day resulting in an average of 3 BMR per months, which seems to fit the data at both solar minimum, during cycle 23 and 24.

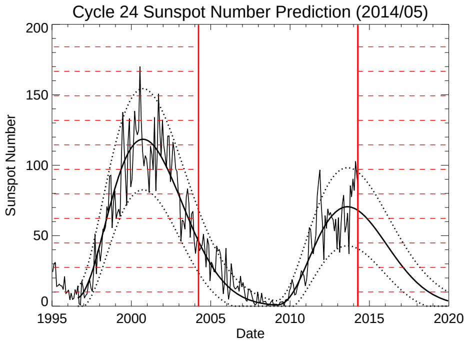

Source:Hathaway/NASA/MSFC

Figure 1.2: Monthly averaged sunspot number Figure from NAS

1

Chapter 2

Spectrum analysis

2.1 Linear continuous time ARMA

It has been common to work with discrete time for modelling light curves such as AR or ARMA models. However, approximation by discrete time processes can lead to erroneous interpretations when searching for periods (Vio et al., 2005). Light curves are not stationary processes, although they can be considered as so on a very small time periods. The underlying processes that we have worked with in the previous parts are all time dependent, and this characteristic might give rise to errors when using discrete time modelling. It is therefore important to include this time dependency in the model which can be done by using continuous time modelling. The alternative to a discrete time ARMA model would be a Continuous time ARMA.

An ARMA(p,q) model is a combination of an AutoRegressive, AR(p), and a Moving Average, MA(q) model where p is the order of the AR part, and q the order of the MA part (Madsen, 2008).

The AR(p) part is given by:

$$X_t = X_0 + \sum_{i=1}^{p} \phi_i X_{t-i} + \epsilon_t \tag{2.1}$$

where X_0 is the initial value, and ϕ_i the parameters of the process, the noise term, ϵ is i.i.d. , $\epsilon \sim \mathcal{N}(0, \sigma^2)$. The AR(p) process is a regression on past values up to the time t and gives information about how the state at time t is influenced by the weighted sum of the previous states up to time $t - i$, for $1 \leq i \leq p$ and the noise at time t. From lag p +1, all the parameters are zero.

The MA(q) part corresponds to:

$$X_t = \mu + \epsilon + \sum_{i=1}^{q} \theta_i \epsilon_{t-i} \tag{2.2}$$

where μ is the mean value of X_t, θ_i the parameters of the process and ϵ_i the noise term, ϵ is i.i.d. , $\epsilon \sim \mathcal{N}(0, \sigma^2)$.

The MA(q) process is a linear regression on the past values of the noise term. Here, can all the parameters be zero from lag i, $1 \leq i \leq q$.

The ARMA(p,q) model becomes:

$$X_t = X_0 + \epsilon + \sum_{i=1}^{p} \phi_i X_{t-i} + \sum_{i=1}^{q} \theta_i \epsilon_{t-i} \tag{2.3}$$

with q< p.

and can also be written:

$$X_t + \phi_1 X_{t-1} + ... + \phi_p X_{t-p} = X_0 + \mu + \epsilon_t + \theta_1 \epsilon_{t-1} + ... + \theta_q \epsilon_{t-q} \tag{2.4}$$

We now consider the dynamical system in continuous time, an ARMA(n,m) state space model (Brockwell and Davis, 2002). The model is represented by a system equation, X_t, and an observation equation, Y_t. Such a process can be written as :

$$\begin{aligned} dX(t) &= AX(t) + \sigma B dW(t) \\ Y(t) &= CX(t) + \epsilon \end{aligned} \tag{2.5}$$

A, B, and C are matrices, σ is the variance and ϵ is i.i.d., $\epsilon \sim \mathcal{N}(0, \sigma^2)$. $W(t)$ is standard Brownian motion defined as :

$$\begin{aligned} W(t) &= \int_0^t dW_s \\ W(t + \Delta t) - W(t) &\sim \mathcal{N}(0, \Delta t) \end{aligned} \tag{2.6}$$

The model is a system of Stochastic Differential Equations.

The matrices from equation 2.5 are given by:

$$A = \begin{bmatrix} -a_1 & 1 & 0 & \cdots & 0 \\ -a_2 & 0 & 1 & \cdots & 0 \\ \vdots & \vdots & \vdots & \ddots & \vdots \\ -a_{n-1} & 0 & 0 & \ddots & 1 \\ -a_n & 0 & 0 & \cdots & 0 \end{bmatrix} \tag{2.7}$$

$$B^T = \begin{bmatrix} 1 & b_1 & \dots & b_{n-2} & b_{n-1} \end{bmatrix} \tag{2.8}$$

where the b_{n-i}, $1 \leq n-i \leq n-1$, can be equal to zero from a certain $n-i$.

$$C = \begin{bmatrix} 1 & 0 & \dots & 0 & 0 \end{bmatrix} \tag{2.9}$$

The states $X(t)$ are:

$$X^T(t) = \begin{bmatrix} X_1(t) & X_2(t) & \dots & X_{n-1}(t) & X_n(t) \end{bmatrix} \tag{2.10}$$

and the observations $Y(t)$:

$$Y^T(t) = \begin{bmatrix} Y_1(t) & Y_2(t) & \dots & Y_{n-1}(t) & Y_n(t) \end{bmatrix} \tag{2.11}$$

The transfer function of the system is found as

$$H(s) = sC(Is - A)^{-1}B \tag{2.12}$$

where I is the identity matrix.

which results in :

$$H(s) = -s\frac{s^q + b_1 s^{q-1} + ... + b_q}{-s^p + a_1 s^{p-1} + ... + a_p} \tag{2.13}$$

with q <p.

The spectrum can be found using: $\mathcal{H}(\omega)\ \mathcal{H}(-\omega)$ where $\mathcal{H}(\omega) = H(i\omega)$.

And period is then:

$$\frac{T}{Argmax(\mathcal{H}(\omega)\mathcal{H}(-\omega))} \tag{2.14}$$

In this work, T is 6 hours or $\frac{1}{4}$ day.

2.2 The Lomb Scargle periodogram

Spectrum analysis with the help of the Lomb Scargle periodogram is a widely used technique when dealing with enevenly spaced time series such as astrophysical data (Scargle, 1982). It is constructed in such a way that it can handle missing values (Scargle, 1982).

The classical periodogram requires evenly spaced data, and is constructed around the Discrete Fourier Transform, DFT given by :

$$X(\omega) = \sum_{k=0}^{N-1} X(k) \exp(-i\omega k t) \tag{2.15}$$

for a sample of N instants, where ω is the frequency and t is the sample time. For a time series with N data points, the classical periodogram is given by:

$$\begin{aligned} P_x(\omega) &= \frac{1}{N} |\sum_j X(t_j) \exp(-i\omega t_j)|^2 \\ &= \frac{1}{N} [\sum_j X_j \cos(\omega t_j)^2 + \sum_j X_j \sin(\omega t_j)^2] \end{aligned} \tag{2.16}$$

The Lomb Scargle periodogram on the other hand, is constructed in such a way, that it measures the data points and is not relying on the time intervals. In fact, this method includes a time offset, τ, that makes the power independant of non equidistant time intervals. The normalised Lomb Scargle periodogram is defined as following:

$$P(\omega) = \frac{1}{2\sigma^2} \left(\frac{[\sum_j (h_j - \bar{h}) \cos \omega (t_j - \tau)]^2}{\sum_j \cos^2 \omega (t_j - \tau)} + \frac{[\sum_j (h_j - \bar{h}) \sin \omega (t_j - \tau)]^2}{\sum_j \sin^2 \omega (t_j - \tau)} \right) \tag{2.17}$$

where τ is defined as:

$$\tan(2\omega\tau) = \frac{\sum_j \sin^2 \omega t_j}{\sum_j \cos^2 \omega t_j} \tag{2.18}$$

σ^2 is the variance and $\bar{h}$ is the mean:

$$\begin{aligned}\bar{h} &= \frac{1}{N}\sum_{i=0}^{N-1} h_i \\ \sigma^2 &= \frac{1}{N-1}\sum_{i=0}^{N-1}(h_i - \bar{h})^2 \qquad (2.19)\end{aligned}$$

2.3 Comparison of methods

We have investigated different samples of the light curve, using the package Continuous Time Stochastic Modelling in R, CTSM-R. The best estimation is found with a log likelihood ratio test. We test the method with two examples. Here is one time step equivalent to six hours, meaning that we have to divide the actual period found by four to find the period in days.

2.3.1 Spectrum of the light curve between a solar maximum and a solar minimum

We choose a portion of the data corresponding to the time from a solar maximum to a minimum. The data represents 350 points, which is about 3 months or approximatively 3.5 solar rotations.

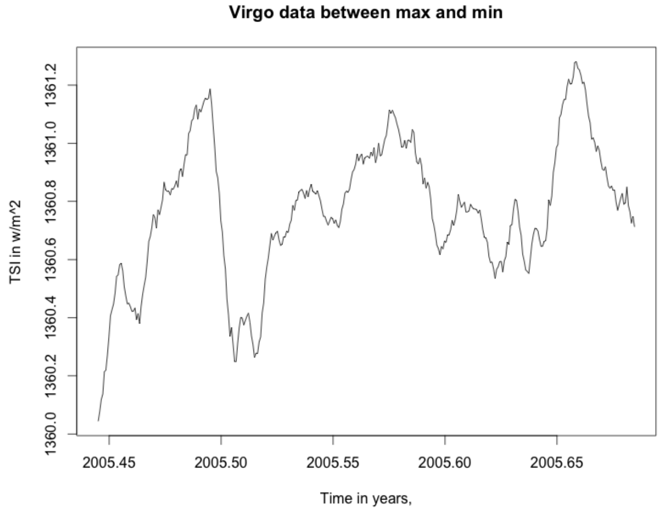

Figure 2.1: TSI between a solar maximum and minimum

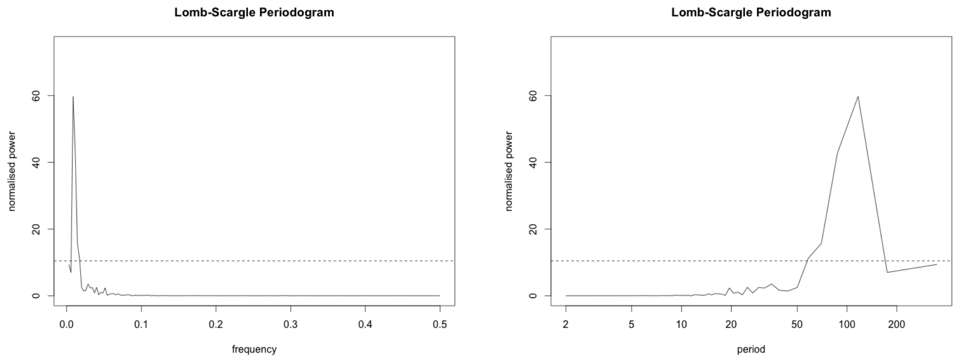

(a) Frequency Lomb Scargle (b) Period Lomb Scargle

Figure 2.2: Lomb Scargle Periodogram

The best estimation is found with a continuous time ARMA(3,1).

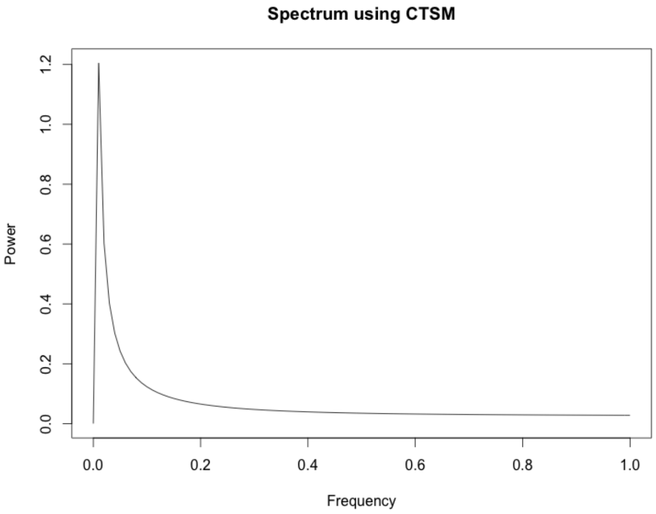

Figure 2.3: Spectrum with CTSM

We find a period of 25 days which is the rotation's period at the equator and is similar to the period found with the Lomb Scargle periodogram.

In fact, all the periods we found with this method were 25 days. This corresponds most of the time to the dominant period. It is clear that it is dominant in the spectrum, as it corresponds to a latitude where the brightness is at its highest. We have not found other periods, even when the dominant period is not the equatorial rotation time, which denotes either the need of adjusting some of the parameters to estimate, or the need to construct a more elaborate model such as a non linear continuous time stochastisc model that can handle more complex underlying processes. We will not go further into that subject in the present project. Instead, we will use the Lomb Scargle periodogram technique and perform some tests for investigating the different parameters that can influence the light curve.

Chapter 3

Analysis of the simulated light curve

We now want to perform some tests and compare the periods found in the sample from the real data and from the simulated, using the Lomb Scargle periodogram. It is important to underline that some of the tests do not necesseraly correspond to real scenarios, but are performed with the only purpose to see the consequences of extreme changes in the timescale of the parameters. This can give an indication about how to adjust other variables values in order to give rise to a similar effect.

The sample from the Virgo light curve is just before a solar maximum, and range over 730 days corresponding to a 6 months period with of sampling time of 6 hours. In this portion of data, there are no missing values.

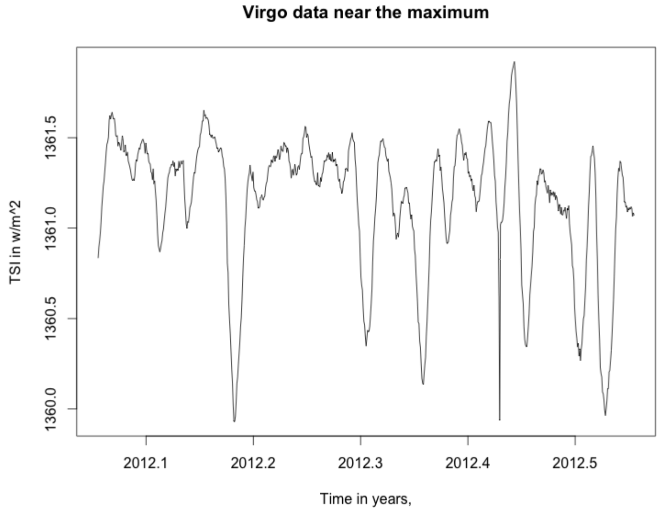

Figure 3.1: TSI on the way up to a solar maximum

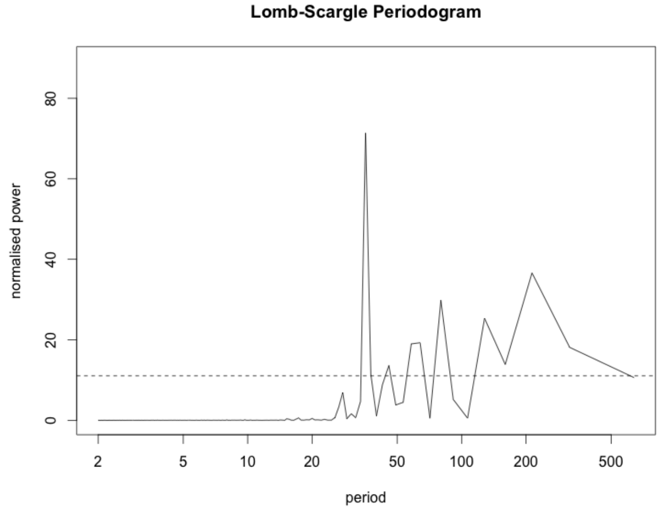

Figure 3.2: Periods from the Lomb Scargle periodogram, 1 day = 4 time steps

Figure 3.2 illustrates that the dominant period is not always the rotation period at the equator, but can represent other timescales, such as a period of 10 days. During the time up to a solar maximum, there are many processes that may overshadow for the equatorial period of rotation. Alongside with that period, there are other significant periods found in this light curve, and we want to investigate what the causes to these peaks can be.

To this end, we have tried to find a similar part of the simulated light curve that could contain peaks in the spectrum that reminds of those from the

VIRGO data. The exact corresponding time in our light curve, between a year and a couple of years before the solar maximum, did not present interesting periods in its spectrum besides of the rotation period. We have therefore chosen a sample from our simulated light curve just after a solar maximum instead. What is interesting is that we have found spikes at similar times in the Lomb Scargle periodogram from the simulated light curve, than those from the real data.

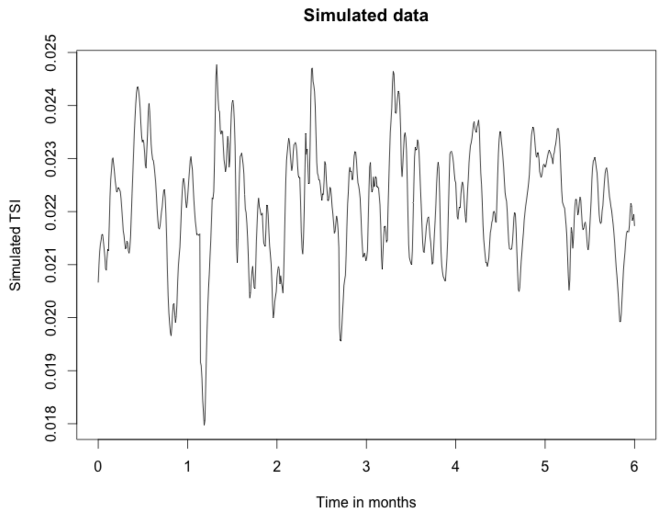

Figure 3.3: TSI on the way up to a solar maximum

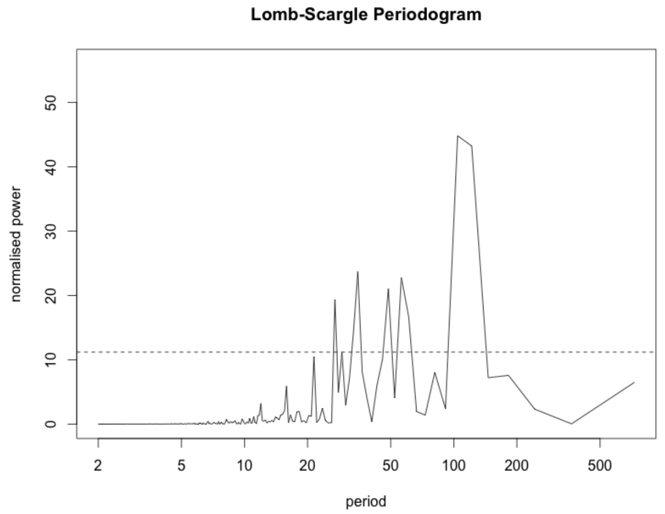

Figure 3.4: Period from the Lomb Scargle periodogram

We recognise the spikes between 20 and 50 time steps, around 50 and 100. We will focus on finding the causes of the peaks before 100 time steps, 25 days.

In the next sections, we will stress the possible factors that can influence the VIRGO light curve on a short time scale. The contributions to the lightcurves from the intensity of the spots and the contrast of the faculae can be seen in Appendix A.

1. Increased rate of emergence
2. High latitude of emergence
3. High latitude and increased emergence rate
4. Low latitude of emergence
5. Low latitude and increased emergence rate
6. Mid latitude
7. Mid latitude and middle emergence rate
8. Slow differential rotation
9. Fast differential rotation
10. Slow meridional flow
11. Fast meridional flow

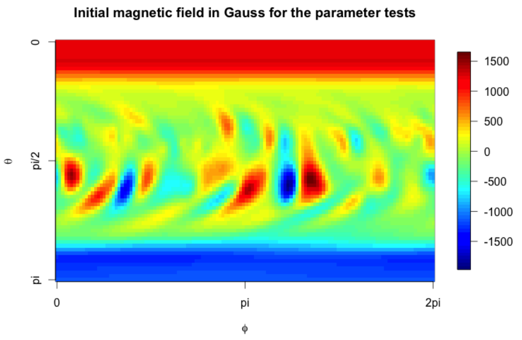

Figure 3.5: Initial field for the tests

The initial field for the tests is chosen to be 7 months after the simulated solar maximum of our two cycles lightcurve. It is clear that at this stage of the cycle, the solar activity is high, which can be seen on figure 3.5.

3.1 Increased rate of emergence

We run a simulation with an increased rate of emergence, from 1.9 BMR per day to 5 BMR per day, which can correspond to the monthly averaged number of spots for a very active cycle, e.g during the solar maximum of cycles 21 and 22.

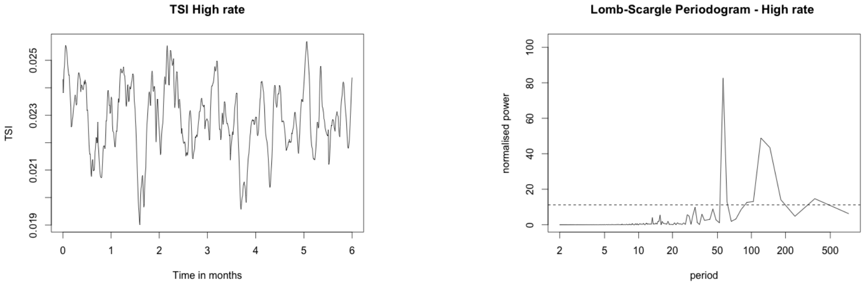

(a) TSI (b) Period Lomb Scargle

Figure 3.6: Increased rate of emergence 5 BMR per day at solar maximum

The increased rate of emergence, makes the period of half a rotation the dominant period. We recognise the shape and the power value from figure 3.2, although it is not the same period. The period at 100 time steps has moved to a higher value, and this is also a feature we have seen in the VIRGO data.

3.2 High emergence latitude

We have raised the mean latitude of emergence of the leading spot to 40 degrees with a standard deviation of 10 degrees, at solar minimum.

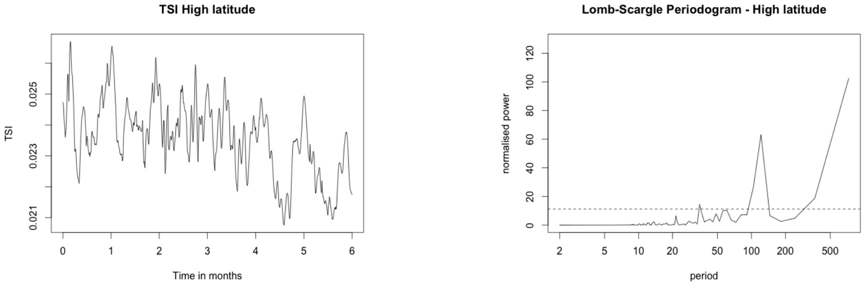

(a) TSI (b) Period Lomb Scargle

Figure 3.7: High latitudes

The high latitude of emergence dominates all other parameters than the differential rotation and the meridional flow, that we suspect to be the beginning spike after 500 time steps. This is in concordance with the light curve study we made in Part II, chapter 4.

3.3 High latitude and increased emergence rate

We still have a raised latitude of emergence, but have increased the rate to 5 BMR per day.

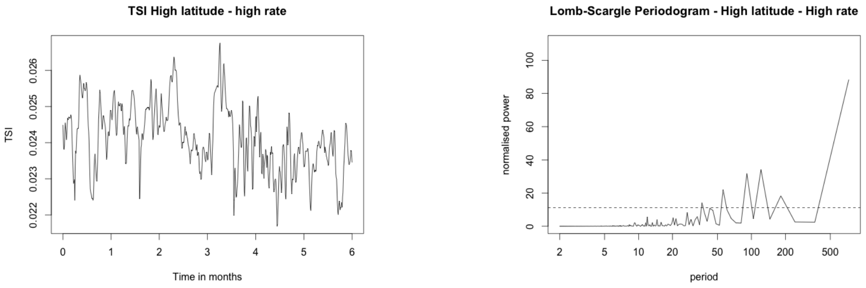

(a) TSI

(b) Period Lomb Scargle

Figure 3.8: High latitudes and increased rate

A high latitude combined with an increased rate, lowers all the periods except the period for the meridional flow. This is actually what was expected, when sunspots emerge at high latitudes, while the following spot is driven by the meridional flow, the strength of the leading spot has weakened before being taken by the differential rotation.

3.4 Low latitude of emergence

In this test, we have lower the mean of the latitude of emergence at solar minimum to 15 degrees with a standard deviation of 5 degrees. Furthermore, we have threshold the zone free of BMR to a maximum of 20 degrees.

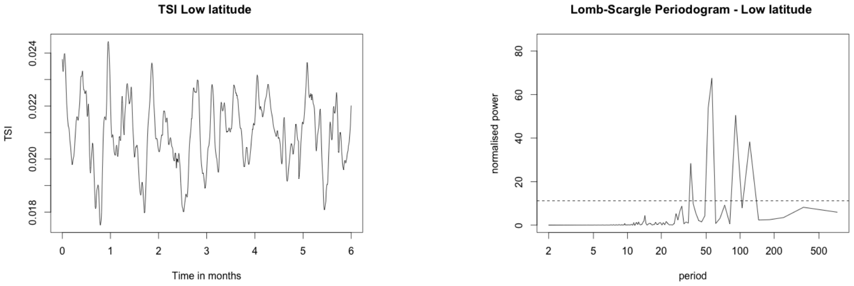

(a) TSI (b) Period Lomb Scargle

Figure 3.9: Low latitudes

Figure 3.9 shows that the shorter periods are favorised, when lowering the latitude of emergence. The peak at around 40 time steps, which is the dominant period in the VIRGO sample has become more significant.

3.5 Low latitude and increased emergence rate

We repeat the same test as the previous and add an increased rate of emergence.

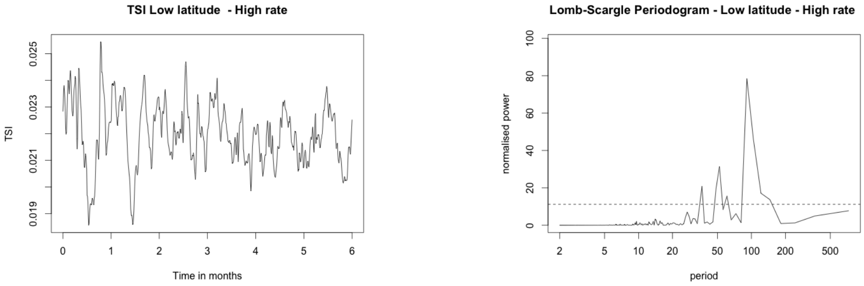

(a) TSI (b) Period Lomb Scargle

Figure 3.10: Low emergence latitude and increased rate

The increase in the rate of emergence cancels out the effect of the lowered mean of emergence. The dominant period is the rotation time at the equator.

3.6 Mid latitude

We lower the mean latitude of emergence at solar minimum to 20 degrees for the leading spot with a standard deviation of 5 degrees.

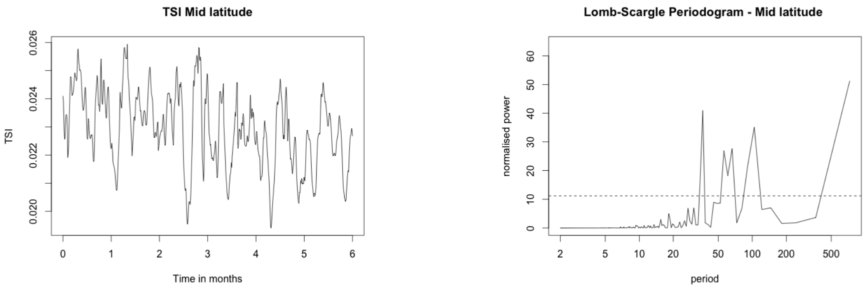

(a) TSI (b) Period Lomb Scargle

Figure 3.11: Mid emergence latitude

Lower latitudes give a dominant period of approximatively 40 time steps. This is the same dominant period we have seen in the VIRGO light curve.

3.7 Mid latitude and middle emergence rate

We repeat the test combined with a slightly higher rate of emergence, that we set to 3 BMR per day at solar maximum.

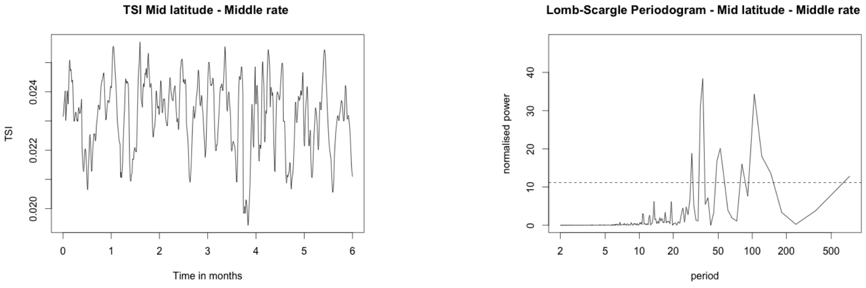

(a) TSI (b) Period Lomb Scargle

Figure 3.12: Mid emergence latitude and middle rate

A slightly higher emergence rate has made the period of the meridional flow to be longer. The dominant period is still the one at 40 time steps, but the dominance is not as pronounced as in the VIRGO data.

3.8 Slow differential rotation

We have decreased the differential rotation to a rotation period four times slower, i.e 100 days at the equator.

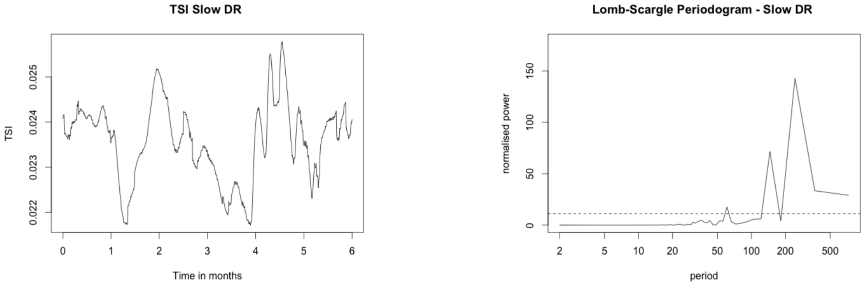

(a) TSI (b) Period Lomb Scargle

Figure 3.13: Slow differential rotation 100 days at the equator

The slow differential rotation pushes the dominant period to be about 300 time steps, corresponding to 75 days and at the half of it..This corresponds to the rotation at the equator and its half time. A slow differential rotation, makes all the other periods to disappear. The peaks are at the same time than on figure 3.2.

3.9 Fast differential rotation

We have increased the differential to twice as fast, resulting in a rotation period of 12.5 days at the equator.

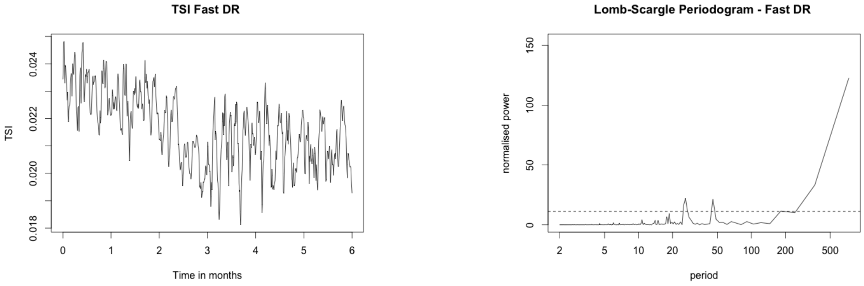

(a) TSI

(b) Period Lomb Scargle

Figure 3.14: Fast differential rotation

We were expecting to see a shorter time period, corresponding to the faster differential rotation. Instead, the dominant period seems to be the meridional flow. This can be explained by the fact that the spots are transported so fast, that it takes under one rotation, before they are driven by the meridional flow and makes them difficult to be traced.

3.10 Slow meridional flow

we have set the velocity, $v_0(t)$, to 5 meters per second instead of 11 meters per second.

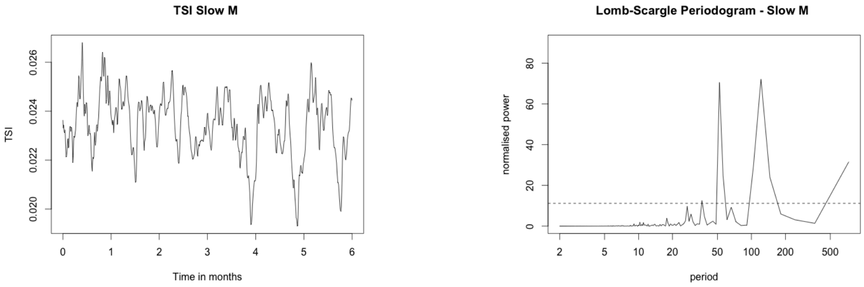

(a) TSI

(b) Period Lomb Scargle

Figure 3.15: Slow meridional flow $v_0(t) = 5$ m per second

A slow meridional flow produces the periods at 50 and 100 time steps, i.e 12.5 and 25 days. This is what expected as it takes longer time for the flux to be pushed polewards, and is therefore longer time in brighter zones of the sphere, than when using an average meridional flow velocity.

3.11 Fast meridional flow

Here we have now raised the velocity of the meridional flow to 30 meters per second.

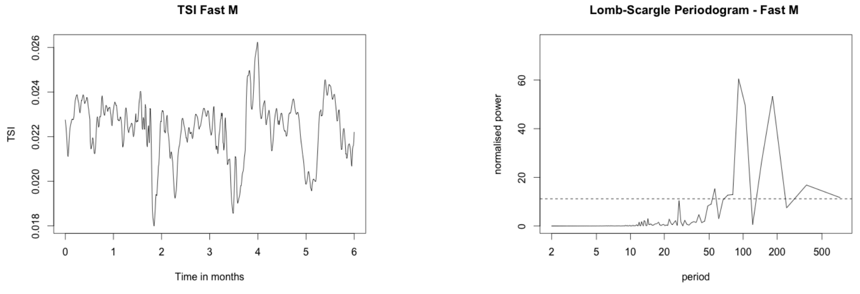

(a) TSI

(b) Period Lomb Scargle

Figure 3.16: Fast meridional flow $v_0(t) = 30$ m per second

A fast meridional flow creates a peak at 200 time steps, 50 days. But we do not recognise any periods from the VIRGO Lomb Scargle periodogram.

3.12 Final test

We have shortly stressed what possibly can influence strongly the periods in a light curve. We have recognised the dominant periods from the VIRGO data, in the tests. The one where we have lowered four times the velocity of the differential rotation corresponding to a rotation period of 100 days at the equator a dominant period at around 300 time steps, 75 days, was produced. The other test that gave results was when we lowered the mean of emergence for the solar minimum, resulting in lower emergence latitudes at solar maximum, combined with a slightly raised emergence rate. Because the differential rotation velocity has been established quite precisely (Snodgrass, 1983), we will not change its velocity despite of the results from the test. Instead we will try to adjust other parameters that can have the same influence.

We will perform a last test where we lower the latitude of emergence to mid latitudes, i.e a mean latitude of 20 degrees at solar minimum down to 5 degrees for the leading spot, with a standard deviation of 5 to 2 degrees. In this test, we have lowered the velocity of the meridional flow from 11 down to 9 meters per second, and the supergranular diffusion to 250 km^2/s. The rate of emergence is raised to 3.5 BMR per day at solar maximum, and 0.1 BMR per day at solar minimum.

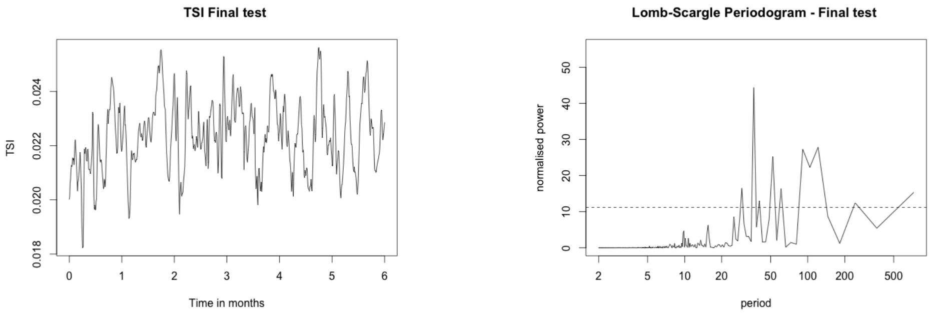

(a) TSI

(b) Period Lomb Scargle

Figure 3.17: Final test of parameter value adjustement

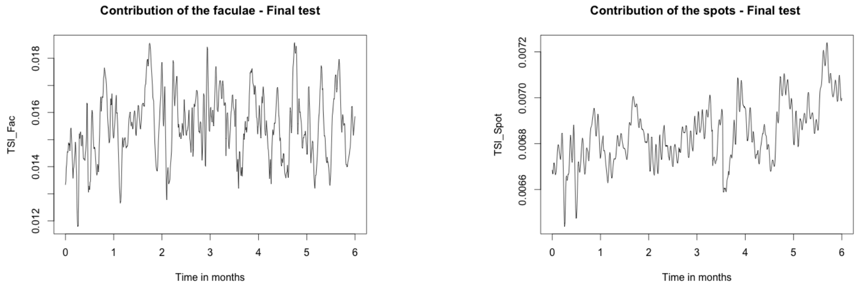

(a) Contribution of the faculae

(b) Contribution of the spots

Figure 3.18: Intensity contribution from the sunspots and the faculae

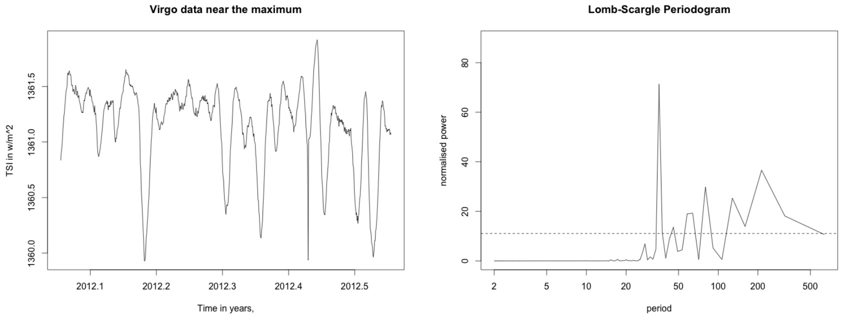

(a) TSI (b) Period Lomb Scargle

Figure 3.19: Periods from the VIRGO data

The dominant period is now the same as the one of the VIRGO sample, corresponding to 40 time steps, 10 days. The 100 time steps, 25 days, has been lowered. There is also a peak just after 50 time steps on both periodograms. The significant periods in this final test are more or less at the same time steps, and more comparable than with the mid latitudes of emergence test or with the test from the slow differential rotation.

Chapter 4

Summary and conclusion

We have worked with real data from the SOHO spacecraft VIRGO. We have tested two methods, that are designed to handle unevenly spaced time series, for finding the periods in the VIRGO light curve. The principle behind each method has been shortly presented. The first one was through the transfer function of a continuous time ARMA model, where the parameters were estimated with CTSM in R. We have tested the method on data from different stages of the solar cycle, and the only period found was the period corresponding to the rotation time at the equator, 25 days. Some adjustements in CTSM-R, such as fixing the noise variance at a very low level, could possibly contributes to find other significant periods. The other method was a Lomb Scargle periodogram, that is a modified classical periodogram. It is a widely used method when working with astrophysical data, or other kinds of data that might suffer from missing values, because its construction makes it independant of the time intervals. It was possible to find a larger number of significant periods than with the previous method. We therefore chose this method for the comparison of the parameter tests.

It is clear that the period found from the spectrum of light curves are influenced by the limb darkening and other irradiance and measurement corrections. The effect of the differential rotation might be dominating at the rotation time of the equator. However, we have tried to adjust some of the parameters that can influence the light curves. In a final test, we have succeed in changing the dominant period from the equatorial rotation time to the one from the VIRGO data, at 10 days. It is necessary to adjust all the parameters with each other, when trying to find a specific period.

Conclusion

Summary

We have analysed a flux transport equation that governs the evolution of the magnetic flux on the solar surface. This model has been used in several studies about the different parameters that influence the solar variability. The dispersal of the magnetic flux,B , is modelled as a PDE, as a function of the colatitude θ, the longitude ϕ and time. The three processes that govern the flux evolution comprise the meridional flow, that makes the magnetic field to migrate polewards, the differential rotation, that reflects the different period of rotation at the equator, 25 days, compared to the poles, 36 days, and finally the supergranular diffusion, that dissipates the magnetic flux with time. In a first part, we have stressed the most important numerical methods for solving a PDE, without source term. The spectral methods, hereunder the spherical harmonics approach have been tested for the approximation to the solution of the PDE. The finite methods, i.e. Finite Differences, Finite Elements, and the Finite Volume methods have been presented. From these, the Finite Volume method has been used as a part of a combined scheme, with FV, in the North - South direction, and spectral, in the West- East direction. It is an unusual method that we have not been presented to in other studies, neither about the transport of the magnetic field on the solar surface, nor in other kinds of work . The approximation to the solution has been submitted to specific initial conditions with the only purpose to follow the dispersal of the magnetic flow under each of the three processes. The time unit for the tests is one rotation, taken as 28 days, and we have made the flux evolve for 36 rotations. The combined FV-spectral method reproduces well the evolution of the magnetic flow, whereas the SH scheme experienced stability problems especially under the effect of the meridional flow. It was therefore decided to use the FVS method for the rest of the project.

Part II was divided into two subjects, the first chapter was about the process of flux emergence, and the second part concerned the conversion of the evolution of the magnetic field into a light curve. We started by defining a model that can simulate the emergence of new magnetic fluxes in the form of BMR, where sunspots forms. This constitutes the source term of the PDE solved in Part I. We have build a model that reproduces the main features of the complicated geometrical relations between the sunspots at emergence, e.g Joy's law about the tilt angle and the separation angle between the spots, the Hale's polarity law that states that for each hemisphere, there is for each BMR emerging, a leading and a following spot with opposite polarity, which have the opposite polarity compared to the other hemisphere. Moreover, this polarity switches at each cycle. We have based the physical features of sunspots on in-depth analysis about sunspots. The parameters governing the emergence process have been estimated in other wor, through detailed study about the solar dynamo. We have decided not to follow all the implicite relations between the parameters and have defined some of the parameters as following a truncated normal distribution with time dependent means. The next issue was to define the process of the BMR emergence as a stochastic process by using a Poisson point process in time. We have approximated the time of the BMR emergence by a discrete time process with time steps equal to the time steps used in our simulation of the solar cycle and used a time dependent mean that follows the solar cycle, i.e a few number of BMR at solar minimum growing towards the sunspot maximum for decaying back towards a minimum. The model has been tested through a simulation of two cycles, where one cycle had a running time of 12 years, with half a year of overlap at both parts of the cycle, where BMR can emerge at both high and low latitudes until a new cycle begins. Between two cycles, it actually results in one year of overlap. The period of one cycle becoming 11 years. The results of this simulation were convincing and we chose to use it for the following chapter, that dealed with the conversion of the evolution of the magnetic field into a light curve.

The conversion is a complex procedure that involves many factors that have been empirically estimated. It is not possible just to map the evolution of the magnetic field into a light curve without taking into account some optical factors. Limb darkening, the spots and the faculae are the primary factors that contributes to a light curve. The limb darkening is an optical effect resulting from a difference in temperature between the center of the visible disk and the limb. It makes the center of the observed disk appear brighter than the limb. A the sunspots, where the concentration of magnetic field is high, the ltemperature is lower than the surrounding and therefore appear dark. The faculae, bright spots, that are always associated to sunspots, on the other hand, have a very high contrast. In fact, the irradiance from the faculae is the main contribution to a light curve. Once the intensity from the spots and the faculae are calculated, they are needed to be projected on the sphere and corrected by the limb darkening. One point of light curve is found as the spherical integral of the corrected intensity. Previous study has shown that the intensity form the sunspots has a contribution to the light curve of under 0.01 % while the other part comes from the intensity of the faculae. The model we used is simplified, in the sense that observations show that the area of the faculae is ten times higher than the areal of the sunspots. In the present work, we have used a 1:1 areal relation between the sunspots and the faculae. On this basis, we have set the contribution of the irradiance of the faculae to the light curve to be 99 % and 1 % coming from the irradiance of the sunspots.

In the last part, Part III, we have used the simulated light curve from Part II, in order to perform some analysis about the spectrum and the dominant periods found in a light curve. The aim was to compare the spectogram of real data to simulated data on a short time scale, i.e. six months. The real data we used were from a VIRGO lightcurve, from which we chose a sample that presented many unusual periods, i.e that were not only corresponding to the period of rotation at the equator, 25 days. Light curves are generally unenvely spaced times series and it is important to use a method that can handle missing values. We have tested two different methods that are adequate to this kind of time series, a Continuous Time ARMA, model, which is a system of stochastic differential equations, where the parameters were estimated with CTSM-R, from which the transfer function and the spectrum could be found. The other method was the Lomb Scargle peridodogram, which is a modified periodogram that makes the calculation of the periods independent of the time steps. The only period found through the continuous time ARMA model was a period of 25 days corresponding to the period of rotation at the equator. The Lomb Scargle periodogram could find other periods, such as a half period of rotation. In the last chapter, we have perform some tests by changing the parameter values of the processes that govern the evolution of the magnetic field at solar surface. We have investigated the effect of the latitude of emergence, the rate of emergence, the velocity of meridional flow and the differential rotation. It appeared that a slow differential rotation could explained two of the unusual periods found in the VIRGO Lomb Scargle periodogram. A lowered latitude of emergence, combined with a slightly increased rate of emergence, a lower diffusion timescale and a lower meridional flow velocity, could produce a periodogram with a dominant period similar to the one in the VIRGO sample.

Conclusion

For solving numerically a PDE on flux transport on a sphere it is primordial to work with a method that can assure stability and conservation of the field, as the FV method does. The FVS method presents also the advantage to reduce the number og grid cells compared to a pure FV, making the code more efficient. Moreover, the approximation with the real SH requires to solve a system of $(\mathrm{lmax}+1)^2$ equations, while the use of a combined finite volume - spectral method reduces the system to (lmax + 1) differential equations. This makes the code remarkably shorter to implement and reduces the running time. The combination of the finite volume with the spectral method allows us to exploit the rotation symmetry by using the properties of the eigenfunctions of a differential operator that is rotationally invariant. Furthermore, the use of a spectral method in one of the directions results in a much smaller grid than if we only used a pure finite volume scheme. It can certainly be recommanded to use this untraditional method for work about flux transport processes on a sphere.

Not following exactly the relations between the different parameters that characterise sunspots, as described in the litterature from observations and previous work, produced quite interesting results. The simulated solar cycles could show similar periods than in real data, and it seems to be an important factor to determine the emergence of the BMR as a stochastic process. But also to allow the different parameters that govern the emergence of the sunspots to deviate from the mean values found in previous estimations. It might correspond to what actually happens on the Sun.

This was confirmed when analysing the spectra of the real data and the simulated one. We wanted to find the periods with the help of a continuous time model in order to have a better insight of the underlying processes in the solar dynamo. To this end we tested a linear continuous time ARMA model, that unfortunately did not give periods different from the equatorial rotation time. Adjustements in the parameters of the model could eventually solve this issue. Nevertheless, it might be necessary to build a more complex model, such as a non linear continuous time stochastic model, as suggested by other light curve studies.

Future work

- Despite of the interesting results from this work, it would be recommandable to adjust the area of the faculae to ten times the area of the sunspots. Although we have tried to compensate for the too small area, it would produce even more reliable results in the analysis of a simulated light curve. As seen in this project, the position of the concentration of the magnetic field is important mostly because of the effect of the limb darkening, and a raised contribution to the light curve does not necessarely compensate entirely for the missing contrast values that a larger area of field would cover.

- Traditional statistic modelling of light curve includes non parametric methods such as Fourier analysis or parametric methods as ARMA models. The study of solar data indicates that these kind of models do not entirely fit the data and they present a gap between the model and the measurements. It is now accepted that the hidden processes that drive the solar dynamo involve stochastic processes, although the solar dynamo is not well understood. A way to analyse the system with all its components, would be to develop a non linear stochastic model and grey box modelling. This could give us a better insight on our understanding of the solar magnetic field. The latter has become more and more important, as it affects the Earth in many ways, especially as new technology has become a part of our everyday life. For example, satellites or GPS are very exposed to disturbations caused by magnetic, solar, storms.

- Once a reliable model that can provide informations about how the processes at the interior of the Sun are related to the evolution of the magnetic field at solar surface, is validated, it would be of greatest interest to apply it on star types main to the Sun. If the model can be applied succesfully on these types of stars, it could suggest that the magnetic field on the Sun and on stars similar to the Sun is of the same nature. By extension, it could provide informations about their exosystem and the exoplanets that rotate around them.

Appendix A

The contribution from the spots and the faculae to the light curve test from Part III can be seen in this appendix.

Increased rate of emergence

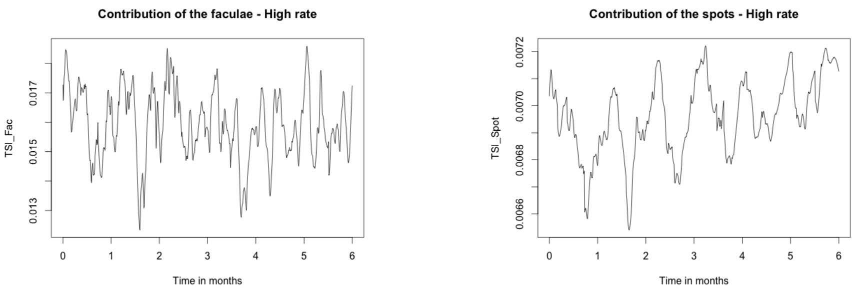

(a) Contribution of the faculae (b) Contribution of the spots

Figure 1: Increased rate of emergence 5 BMR per day at maximum

High emergence latitude

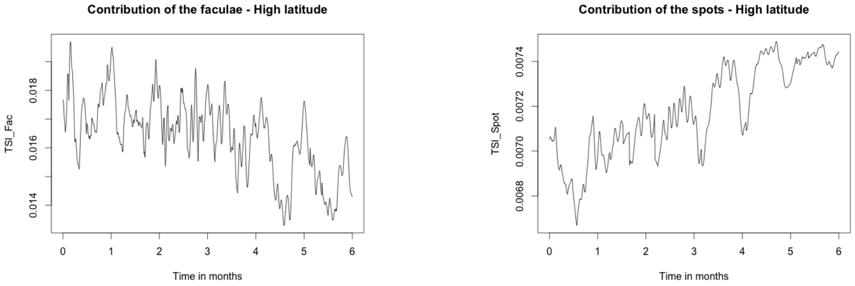

(a) Contribution of the faculae (b) Contribution of the spots

Figure 2: High emergence latitude

High latitude and increasing emergence rate

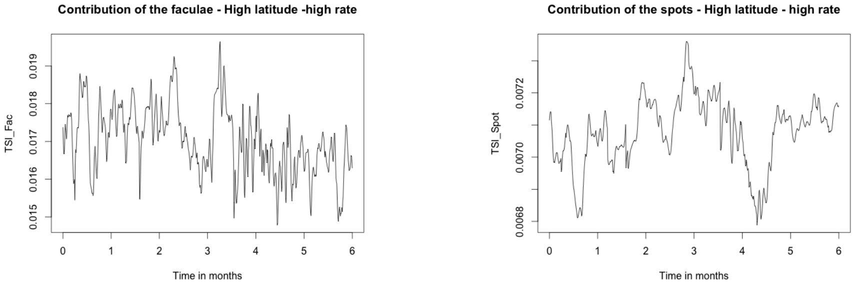

(a) Contribution of the faculae (b) Contribution of the spots

Figure 3: High emergence latitude and rate of 5 BMR per day at maximum

Low latitude of emergence

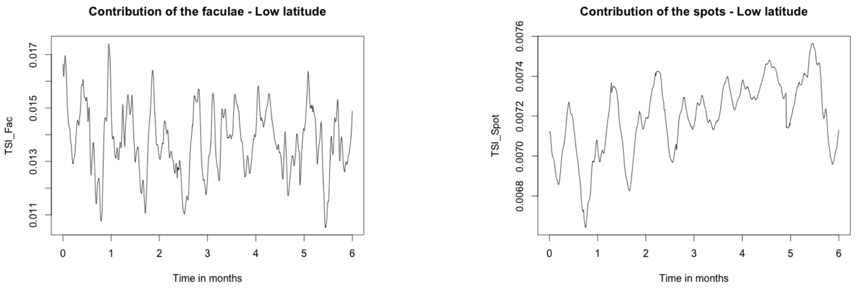

(a) Contribution of the faculae (b) Contribution of the spots

Figure 4: Low emergence latitude

Low latitude and increasing emergence rate

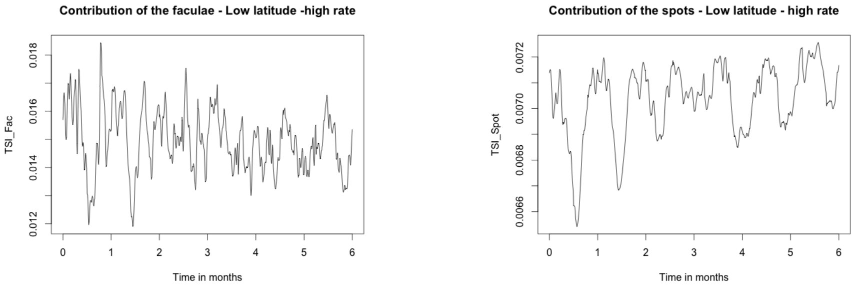

(a) Contribution of the faculae (b) Contribution of the spots

Figure 5: Low emergence latitude and increased rate

Mid latitude

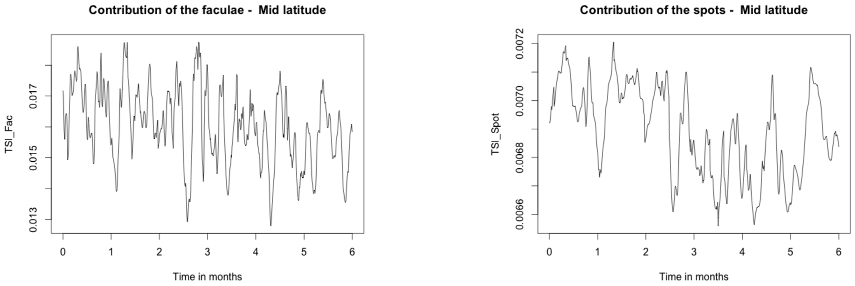

(a) Contribution of the faculae (b) Contribution of the spots

Figure 6: Mid emergence latitude

Mid latitude and increasing emergence rate

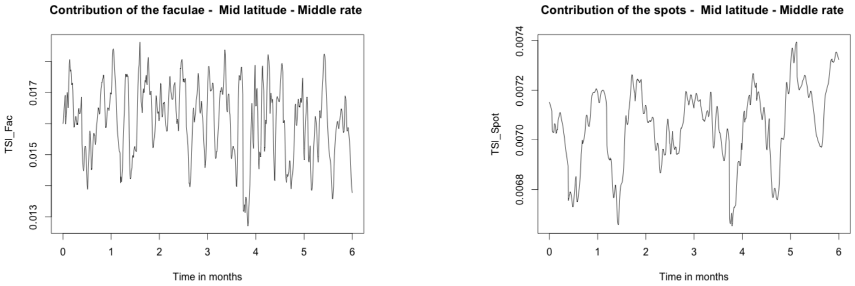

(a) Contribution of the faculae (b) Contribution of the spots

Figure 7: Mid emergence latitude and middle rate of emergence

Slow differential rotation

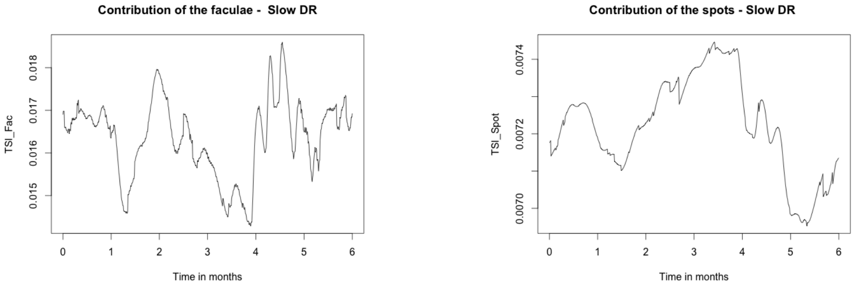

(a) Contribution of the faculae (b) Contribution of the spots

Figure 8: Slow differential rotation

Fast differential rotation

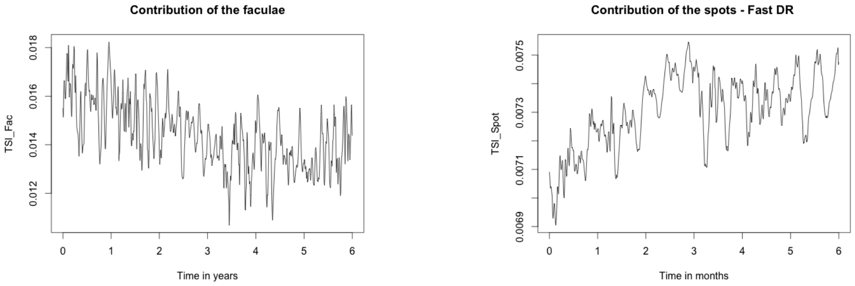

(a) Contribution of the faculae (b) Contribution of the spots

Figure 9: Fast differential rotation

Slow meridional flow

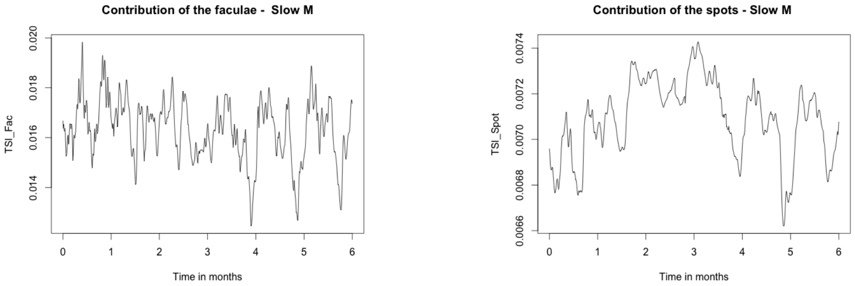

(a) Contribution of the faculae (b) Contribution of the spots

Figure 10: Slow meridional flow

Fast meridional flow

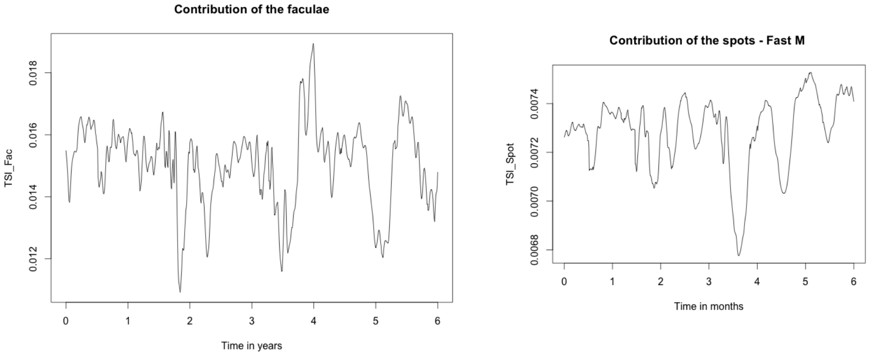

(a) Contribution of the faculae (b) Contribution of the spots

Figure 11: Fast meridional flow

Bibliography

Solar cycle prediction. http://solarscience.msfc.nasa.gov/predict.shtml.

Virgo. http://www.ias.u-psud.fr/virgo/.

J.I. Baumann. *Magnetic flux on the Sun.* PhD thesis, Georg-August-Universit at Gottingen, 2005.

P. J. Brockwell and R. A. Davis. *Introduction to Time Series and Forecasting.* Springer, second edition, 2002.

R. H. Cameron, J. Jiang, D. Schmitt, and M. Schussler. Surface flux transport modeling for solar cycles 15 - 21 : effects of cycle - dependent tilt angles of sunspots groups. *The Astrophysical Journal*, 719:264 – 270, 2010.

B. Costa. Spectral methods for partial differential equations. *Cubo - Revista de Matematica*, 6(34), 2004.

R. Eymard, Herbin, and T. Gallouet. Finite volume methods. *Laboratoire d' Analyse Topologie et Probabilite s, UMR 6632*, 97-19, 2006. http://www.cmi.univ-mrs.fr/~herbin/PUBLI/bookevol.pdf.

G. E. Hale, F. Ellerman, S. B. Nicholson, and A. H. Joy. The magnetic polarity of sun-spots. *Astrophysical Journal*, 49(A82), 1919. http://dx.doi.org/10.1086/142452.

D. H. Hathaway. Doppler Measurements of the Sun's Meridional Flow. *Astrophysical Journal*, 460:1027, 1996. URL http://adsabs.harvard.edu/abs/1996ApJ...460.1027H. Provided by the SAO/NASA Astrophysics Data System.

D. H. Hathaway. The solar cycle. *Living Reviews in Solar Physics*, 7(1), 2010. URL http://www.livingreviews.org/lrsp-2010-1.

D. H. Hathaway. The solar dynamo. *NASA*, 2012. `http://solarscience.msfc.nasa.gov/dynamo.shtml`.

T. P. Higgins and Z. Kopal. Volume Integrals of the Products of Spherical Harmonics and their Application to Viscous Dissipation Phenomena in Fluids. *Astrophysics and Space Science*, 2:352–369, November 1968. URL `http://adsabs.harvard.edu/abs/1968Ap26SS...2..352H`. Provided by the SAO/NASA Astrophysics Data System.

H. Hudson. Solar activity. *Scholarpedia*, 2008. `http://www.scholarpedia.org/article/Solar_activity`.

E. Jensen and T.S Ringnes. On the dependence of the magnetic field strength of sunspots on their areas in relation to the solar cycle. *Astrophysica Norvegia*, 6:1, 1957.

J. Jiang, R. H. Cameron, D. Schmitt, and M. Schussler. The solar magnetic field since 1700 i. characteristics of sunspot group emergence and reconstruction of the butterfly diagram. *Astronomy And Astrophysics*, 528(A82), 2011. `http://dx.doi.org/10.1051/0004-6361/201016168`.

B.W. Jones. *Discovering the Solar System.* John Wiley & Sons Ltd, second edition, 1993.

T. Leonard and D.P. Choudhary. Intensity and magnetic field distribution of sunspots. *Solar Physics*, 252:33–41, 2008.

D. H. Mackay and A. Yeates. The sun's global photospheric and coronal magnetic fields: Observations and models. *Living Reviews in Solar Physics*, 9(6), 2012. doi: 10.12942/lrsp-2012-6. `http://www.livingreviews.org/lrsp-2012-6`.

D.H. Mackay, M. Jardine, A. Collier Cameron, J-F. Donati, and G.A.J Hussain. Polar caps on active stars : magnetic flux emergence and transport. *The Astrophysical Journal*, 501:866 – 881, 2004.

H. Madsen. *Time series analysis.* Chapman & Hall, 2008.

A. Ortiz, S.K.Solanki, V. Domingo, M.Fligge, and B. Sanahuja. On the intensity contrast of solar photospheric faculae and network elements. *Astronomy and Astrophysics*, 333:1036–1047, 2002.

J. Peiro and S. Sherwin. *Handbook of Materials Modeling*, volume 1 - Methods and Models. Springer, 2005.

J. D. Scargle. Studies in astronomical time series analysis. ii - statistical aspects of spectral analysis of unevenly spaced data. *The Astrophysical Journal*, 263: 835:853, 1982.

B. Schmieder and E. Pariat. Magnetic flux emergence. *Scholarpedia*, 2007. `http://www.scholarpedia.org/article/Magnetic_flux_emergence`.

H. B. Snodgrass and S. B. Dailey. Meridional motions of magnetic features in the solar photosphere. *Solar Physics*, 163:21–42, 1996.

H.B. Snodgrass. Magnetic rotation of the solar photosphere. *The Astrophysiscal Journal*, 270:288–299, 1983.

S.K. Solanki. Sunspots: An overview. *The Astronomy and Astrophysics Review*, 11:153–286, 2003.

A. A. van Ballegooijen, N.P. Carttledge, and E. R. Priest. Magnetic flux transport and the formation of filament channels on the sun. *The Astrophysical Journal*, 501:866 – 881, 1998.

R. Vio, N.R. Kristensen, H. Madsen, and W. Wamsteker. Time series analysis in astronomy: limits and potentialities. *Astronomy And Astrophysics*, 435: 773–780, 2005.

K. L. Yeo, S.K.Solanki, and N. A. Krivova. Intensity contrast of solar network and faculae. *Astronomy and Astrophysics*, 550:A95, 2013.